

## **INFORMATION TO USERS**

**This manuscript has been reproduced from the microfilm master. UMI films the text directly from the original or copy submitted. Thus, some thesis and dissertation copies are in typewriter face, while others may be from any type of computer printer.**

**The quality of this reproduction is dependent upon the quality of the copy submitted. Broken or indistinct print, colored or poor quality illustrations and photographs, print bleedthrough, substandard margins, and improper alignment can adversely affect reproduction.**

**In the unlikely event that the author did not send UMI a complete manuscript and there are missing pages, these will be noted. Also, if unauthorized copyright material had to be removed, a note will indicate the deletion.**

**Oversize materials (e.g., maps, drawings, charts) are reproduced by sectioning the original, beginning at the upper left-hand corner and continuing from left to right in equal sections with small overlaps.**

**ProQuest Information and Learning  
300 North Zeeb Road, Ann Arbor, MI 48106-1346 USA  
800-521-0600**

**UMI<sup>®</sup>**



**MODIFIED MARKER-AND-CELL MODEL FOR  
WAVE-STRUCTURE INTERACTIONS**

**by**

**Chi-Shih Chao**

---

**A Dissertation Presented to the  
FACULTY OF THE GRADUATE SCHOOL  
UNIVERSITY OF SOUTHERN CALIFORNIA  
In Partial Fulfillment of the  
Requirements for the Degree  
DOCTOR OF PHILOSOPHY  
(CIVIL ENGINEERING)**

**May 2002**

**Copyright 2002**

**Chi-Shih Chao**

**UMI Number: 3073758**

**UMI<sup>®</sup>**

---

**UMI Microform 3073758**

**Copyright 2003 by ProQuest Information and Learning Company.  
All rights reserved. This microform edition is protected against  
unauthorized copying under Title 17, United States Code.**

---

**ProQuest Information and Learning Company  
300 North Zeeb Road  
P.O. Box 1346  
Ann Arbor, MI 48106-1346**

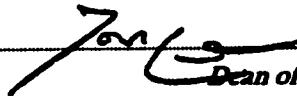
UNIVERSITY OF SOUTHERN CALIFORNIA  
The Graduate School  
University Park  
LOS ANGELES, CALIFORNIA 90089-1695

*This dissertation, written by*

*Chi-Shih Chao*

*Under the direction of his... Dissertation  
Committee, and approved by all its members,  
has been presented to and accepted by The  
Graduate School, in partial fulfillment of  
requirements for the degree of*

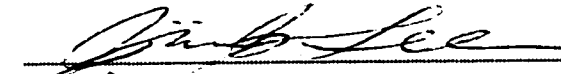
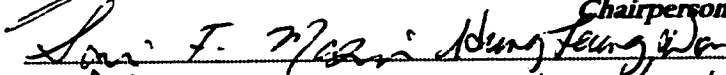
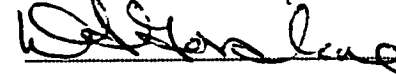
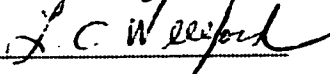
**DOCTOR OF PHILOSOPHY**



Dean of Graduate Studies

Date May 10, 2002

**DISSERTATION COMMITTEE**

  
Chairperson  
  
 

## **Acknowledgments**

**I would like to express the warmest thanks to my advisor, Dr. Jiin-Jen Lee, for his invaluable support, for directing my research, for offering suggestions and encouragement at times of impasse throughout my graduate studies at the University of Southern California.**

**I would like to thank Dr. Donn Gorsline, Dr. Sami F. Masri, Dr. L. Carter Wellford, and Dr. Hung Leung Wong for kindly serving on my Ph.D. guidance and thesis committee and for valuable discussions of the numerical results.**

**I appreciate Dr. Jiin-Jen Lee and F. Zhuang for offering the experimental data of solitary waves overtopping the breakwater. I would also like to thank the Sanitation District of Orange County for offering the experimental data on wave forces acting on the pipeline at the seafloor.**

**Finally, I sincerely thank my parents for the support and encouragement they have given to me. I would like to thank my wife, Shu-Mei Hsu, for her infinite love, caring, understanding and patience during my graduate study. I would like to dedicate this work to her and to my children, Stephaine and Vivian, who have always had the utmost faith in their father.**

# **Contents**

<b>Acknowledgments</b>	<b>ii</b>
<b>List of Tables</b>	<b>vi</b>
<b>List of Figures</b>	<b>vii</b>
<b>Abstract</b>	<b>xv</b>
<b>Chapter 1 Introduction</b>	
<b>Background</b>	<b>1</b>
<b>Objective and Scope of Present Study</b>	<b>3</b>
<b>Chapter 2 Review of Previous Research</b>	
<b>2.1 Theoretical models</b>	<b>5</b>
2.1.1 Solitary wave overtopping the submerged breakwater	5
2.1.2 Solitary wave running up on vertical wall and sloping beach	6
2.1.3 Wave passing over the submarine pipeline	8
<b>2.2 Experimental models</b>	<b>10</b>
2.2.1 Solitary wave overtopping the submerged breakwater	10
2.2.2 Solitary wave running up on vertical wall and sloping beach	11
2.2.3 Wave passing over the submarine pipeline	12
<b>2.3 Numerical models</b>	<b>13</b>
2.3.1 Solitary wave overtopping the submerged breakwater	13
2.3.2 Solitary wave running up on vertical wall and sloping beach	14

<b>Chapter 3</b>	<b>Numerical Method</b>	
3.1	Marker and Cell Method	17
3.2	Governing Equations	19
3.3	Boundary Conditions	20
3.4	Initial Conditions	22
3.5	Finite Difference Scheme	24
<b>Chapter 4</b>	<b>Presentation and discussion of modeling results</b>	
4.1	Wave overtopping on the submerged rectangular structure	41
4.2	Run-up of solitary wave on vertical wall	71
4.3	Run-up of solitary wave on sloping beach	76
4.3.1	Run-up of solitary wave on a $S = 1$ ( $45^\circ$ ) slope	77
4.3.2	Run-up of solitary wave on a $S = 0.58$ ( $30^\circ$ ) slope	78
4.3.3	Run-up of solitary wave on a $S = 0.05$ ( $2.88^\circ$ ) slope	90
4.4	Wave-induced loading on a half-buried pipe	101
4.4.1	Hydrodynamic forces on a half-buried pipe studied by Foda's experiment	101
4.4.2	Hydrodynamic forces on a half-buried pipe studied by the Sanitation District of Orange County, CA.	110
<b>Chapter 5</b>	<b>Conclusion and Recommendation</b>	
5.1	Conclusions	126
5.1.1	Overtopping the submerged rectangular structure	126
5.1.2	Run-up of non-breaking solitary wave on vertical wall	127
5.1.3	Run-up of non-breaking solitary wave on steep sloping beaches	128
5.1.4	Run-up of breaking solitary wave on a mild sloping beach	128
5.1.5	Wave-induced force on half-buried marine pipeline	129



## **List Of Tables**

- 4.1 Comparison of the maximum run-up for a solitary wave with a normalized amplitude  $H/d_0 = 0.05$  at the time when the wave climbs on the vertical wall. .... 72
- 4.2 Comparison of the maximum run-up for a solitary wave with a normalized amplitude  $H/d_0 = 0.2$  at the time when the wave climbs on the vertical wall. .... 75

## List Of Figures

3.1 Cell setup and location of variables	18
3.2.1 Sketch of boundary conditions	20
3.2.2 Boundary condition of sloping beach	22
3.3 Interpolation of pressure $P_{ij}$ near the free surface	29
3.4 Interpolation of velocity $u_k$ at the particle $k$	31
3.5 Outside domain velocity from extrapolation of interior fluid	34
3.5 Boundary orientation in relation to the staggered grid	34
3.7 Control volume for $u$ on a sloping boundary	36
3.8 Sketch of pressure $p$ on sloping boundary	38
3.9 Propagation of velocities near the intersection of free surface and sloping boundary	39
4.1 Solitary wave propagates over breakwater	42
4.2 Comparison of velocities of the present model, experiment (Lee, et al., 1993), and combined rotational flow model (C.R.F.M)(Zhuang, 1994) at $x=0.15$ and $y=0.175$ , which are measured from bottom bed and shoreward face of the breakwater. ( $D/d_o=0.5$ , $H/d_o=0.3$ , $d_o=0.9\text{in}$ )	44

- 4.3 Comparison of velocities of the present model, experiment (Lee, et al., 1993), and combined rotational flow model (C.R.F.M)(Zhuang, 1994) at  $x=0.15$  and  $y=0.25$ , which are measured from bottom bed and shoreward face of the breakwater. ( $D/d_o=0.5$ ,  $H/d_o=0.3$ ,  $d_o=0.9\text{in}$ ) 45
- 4.4 Pictures (A) and (B) of an experimental observation of vortex generation for solitary wave overtopping submerged breakwater.  $D/d_o=0.5$ ,  $H/d_o=0.3$ ,  $d_o=0.9\text{in}$ . (Lee, et al., 1993) 47
- 4.5 Pictures (C) and (D) of an experimental observation of vortex generation for solitary wave overtopping submerged breakwater.  $D/d_o=0.5$ ,  $H/d_o=0.3$ ,  $d_o=0.9\text{in}$ . (Lee, et al., 1993) 48
- 4.6 Velocity field at non-dimensional time  $T=10.0$  ( $t\sqrt{g/d_o}=10.0$ ) by the present model. The ordinate is  $y/d_o$  and the abscissa is  $x/d_o$ .  $D/d_o=0.5$ ,  $H/d_o=0.3$ ,  $d_o=0.9\text{in}$ . (a) the variation of water surface while the solitary wave passing over the breakwater (b) close-up of velocity field in the vicinity of the breakwater 49
- 4.7 Velocity field at non-dimensional time  $T=12.0$  ( $t\sqrt{g/d_o}=12.0$ ) by the present model. The ordinate is  $y/d_o$  and the abscissa is  $x/d_o$ .  $D/d_o=0.5$ ,  $H/d_o=0.3$ ,  $d_o=0.9\text{in}$ . (a) the variation of water surface while the solitary wave passing over the breakwater (b) close-up of velocity field in the vicinity of the breakwater 51
- 4.8 Velocity field at non-dimensional time  $T=14.0$  ( $t\sqrt{g/d_o}=14.0$ ) by the present model. The ordinate is  $y/d_o$  and the abscissa is  $x/d_o$ .  $D/d_o=0.5$ ,  $H/d_o=0.3$ ,  $d_o=0.9\text{in}$ . (a) the variation of water surface while the solitary wave passing over the breakwater (b) close-up of velocity field in the vicinity of the breakwater 52
- 4.9 Velocity field at non-dimensional time  $T=16.0$  ( $t\sqrt{g/d_o}=16.0$ ) by the present model. The ordinate is  $y/d_o$  and the abscissa is  $x/d_o$ .  $D/d_o=0.5$ ,  $H/d_o=0.3$ ,  $d_o=0.9\text{in}$ . (a) the variation of water surface while the solitary wave passing over the breakwater (b) close-up of velocity field in the vicinity of the breakwater 54

- 4.10 Velocity field at non-dimensional time  $T=18.0(t\sqrt{g/d_o}=18.0)$  by the present model. The ordinate is  $y/d_o$  and the abscissa is  $x/d_o$ .  $D/d_o=0.5$ ,  $H/d_o=0.3$ ,  $d_o=0.9\text{in}$ . (a) the variation of water surface while the solitary wave passing over the breakwater (b) close-up of velocity field in the vicinity of the breakwater 55
- 4.11 Velocity field at non-dimensional time  $T=20.0(t\sqrt{g/d_o}=20.0)$  by the present model. The ordinate is  $y/d_o$  and the abscissa is  $x/d_o$ .  $D/d_o=0.5$ ,  $H/d_o=0.3$ ,  $d_o=0.9\text{in}$ . (a) the variation of water surface while the solitary wave passing over the breakwater (b) close-up of velocity field in the vicinity of the breakwater 56
- 4.12 Velocity field at non-dimensional time  $T=50.0(t\sqrt{g/d_o}=50.0)$  by the present model. The ordinate is  $y/d_o$  and the abscissa is  $x/d_o$ .  $D/d_o=0.5$ ,  $H/d_o=0.3$ ,  $d_o=0.9\text{in}$ . (a) the variation of water surface while the solitary wave passing over the breakwater (b) close-up of velocity field in the vicinity of the breakwater 58
- 4.13 Comparison of velocities of the present model and experiment (Lee, et al., 1993), at  $x=0.15$  and  $y=0.175$ , which are measured from bottom bed and shoreward face of the breakwater. ( $D/d_o=0.75$ ,  $H/d_o=0.2$ ,  $d_o=0.9\text{in}$ ) 60
- 4.14 Velocity field at non-dimensional time  $T=10.0(t\sqrt{g/d_o}=10.0)$  by the present model. The ordinate is  $y/d_o$  and the abscissa is  $x/d_o$ .  $D/d_o=0.75$ ,  $H/d_o=0.2$ ,  $d_o=0.9\text{in}$ . (a) the variation of water surface while the solitary wave passing over the breakwater (b) close-up of velocity field in the vicinity of the breakwater 62
- 4.15 Velocity field at non-dimensional time  $T=12.0(t\sqrt{g/d_o}=12.0)$  by the present model. The ordinate is  $y/d_o$  and the abscissa is  $x/d_o$ .  $D/d_o=0.75$ ,  $H/d_o=0.2$ ,  $d_o=0.9\text{in}$ . (a) the variation of water surface while the solitary wave passing over the breakwater (b) close-up of velocity field in the vicinity of the breakwater 63
- 4.16 Velocity field at non-dimensional time  $T=14.0(t\sqrt{g/d_o}=14.0)$  by the present model. The ordinate is  $y/d_o$  and the abscissa is  $x/d_o$ .  $D/d_o=0.75$ ,  $H/d_o=0.2$ ,  $d_o=0.9\text{in}$ . (a) the variation of water surface while the solitary wave passing

over the breakwater (b) close-up of velocity field in the vicinity of the breakwater 64

4.17 Velocity field at non-dimensional time  $T=16.0(t\sqrt{g/d_o}=16.0)$  by the present model. The ordinate is  $y/d_o$  and the abscissa is  $x/d_o$ .  $D/d_o=0.75$ ,  $H/d_o=0.2$ ,  $d_o=0.9$ in. (a) the variation of water surface while the solitary wave passing over the breakwater (b) close-up of velocity field in the vicinity of the breakwater 65

4.18 Velocity field at non-dimensional time  $T=18.0(t\sqrt{g/d_o}=18.0)$  by the present model. The ordinate is  $y/d_o$  and the abscissa is  $x/d_o$ .  $D/d_o=0.75$ ,  $H/d_o=0.2$ ,  $d_o=0.9$ in. (a) the variation of water surface while the solitary wave passing over the breakwater (b) close-up of velocity field in the vicinity of the breakwater 66

4.19 Velocity field at non-dimensional time  $T=20.0(t\sqrt{g/d_o}=20.0)$  by the present model. The ordinate is  $y/d_o$  and the abscissa is  $x/d_o$ .  $D/d_o=0.75$ ,  $H/d_o=0.2$ ,  $d_o=0.9$ in. (a) the variation of water surface while the solitary wave passing over the breakwater (b) close-up of velocity field in the vicinity of the breakwater 67

4.20 Velocity field at non-dimensional time  $T=50.0(t\sqrt{g/d_o}=50.0)$  by the present model. The ordinate is  $y/d_o$  and the abscissa is  $x/d_o$ .  $D/d_o=0.75$ ,  $H/d_o=0.2$ ,  $d_o=0.9$ in. (a) the variation of water surface while the solitary wave passing over the breakwater (b) close-up of velocity field in the vicinity of the breakwater 68

4.21 Close-up of velocity field in the vicinity of the breakwater at non-dimensional time  $T = 14.0$  and  $16.0$  by the present model. The ordinate is  $y/d_o$  and the abscissa is  $x/d_o$ .  $D/d_o=0.75$ ,  $H/d_o=0.3$ ,  $d_o=0.9$ in. 70

4.22 Solitary wave propagates and runs up a vertical beach 71

4.23 The numerical results of normalized free surface profile ( $y/d_o$ ) for the solitary wave with  $H/d_o=0.05$  when the run-up height on the right wall becomes maximum. 73

4.24	The numerical results of normalized free surface profile ( $y/d_0$ ) for the solitary wave with $H/d_0=0.2$ when the run-up height on the right wall becomes maximum.	74
4.25	Solitary wave propagating and running up a sloping beach	76
4.26	Comparison of the free surface profiles of a solitary wave with $H/d_0=0.48$ running up on a $45^\circ$ slope at non-dimensional time $T=5$ . The solid line is the results of present model and the dotted lines are the experimental data of Camfield and Street. (1968)	79
4.27	Comparison of the free surface profiles of a solitary wave with $H/d_0=0.48$ running up on a $45^\circ$ slope at non-dimensional time $T=6.5$ . The solid line is the results of present model and the dotted lines are the experimental data of Camfield and Street. (1968)	80
4.28	Comparison of the free surface profiles of a solitary wave with $H/d_0=0.48$ running up on a $45^\circ$ slope at non-dimensional time $T=9$ . The solid line is the results of present model and the dotted lines are the experimental data of Camfield and Street. (1968)	81
4.29	Comparison of the free surface profiles of a solitary wave with $H/d_0=0.17$ running up on a $30^\circ$ slope at non-dimensional time $T=8.5$ . The solid line is the results of present model and the solid circles are the experimental data of Pengzhi Lin, et al. (1999)	83
4.30	Velocity field on a $30^\circ$ slope at non-dimensional time $T=8.5$ by the present model. The ordinate is $y/d_0$ and the abscissa is $x/d_0$ .	84
4.31	Comparison of the free surface profiles of a solitary wave with $H/d_0=0.17$ running up on a $30^\circ$ slope at non-dimensional time $T=10.3$ . The solid line is the results of present model and the solid circles are the experimental data of Pengzhi Lin, et al. (1999)	86
4.32	Velocity field on a $30^\circ$ slope at non-dimensional time $T=10.3$ by the present model. The ordinate is $y/d_0$ and the abscissa is $x/d_0$ .	87

- 4.33 Solitary wave run-up at  $T=8.5$ . Comparisons of vertical variation of velocities at  $x/d_o=15.4$ ,  $16.4$ , and  $17.4$ . The lines are present model, the circles are experiment by Lin, et al (1999), and the squares are numerical results by RANS method. (Lin, et al, 1999) 88
- 4.34 Solitary wave run-up at  $T=10.3$ . Comparisons of vertical variation of velocities at  $x/d_o=15.4$ , and  $16.4$ . The lines are present model, the circles are experiment by Lin, et al (1999), and the squares are numerical results by RANS method. (Lin, et al, 1999) 89
- 4.35 Comparison of the free surface profiles of a solitary wave with  $H/d_o=0.28$  running up on a  $2.88^\circ$  slope at non-dimensional time  $T=10$ . The solid line is the results of present model and the solid circles are the experimental data of Synolakis(1987), and the dash lines are the numerical results of WENO method by Ying Li(2000). 92
- 4.36 The velocity field of a solitary wave with  $H/d_o=0.28$  running up on a  $2.88^\circ$  slope from  $x/d_o=20$  to  $x/d_o=40$  at non-dimensional time  $T=10$ . (a)The ordinate is  $y/d_o$  and the abscissa is  $x/d_o$ . (b)The ordinate is  $(y/d_o)*10$  and the abscissa is  $x/d_o$ . 93
- 4.37 Comparison of the free surface profiles of a solitary wave with  $H/d_o=0.28$  running up on a  $2.88^\circ$  slope at non-dimensional time  $T=15$ . The solid line is the results of present model and the solid circles are the experimental data of Synolakis(1987), and the dash lines are the numerical results of WENO method by Ying Li(2000). 94
- 4.38 The velocity field of a solitary wave with  $H/d_o=0.28$  running up on a  $2.88^\circ$  slope from  $x/d_o=20$  to  $x/d_o=40$  at non-dimensional time  $T=15$ . (a)The ordinate is  $y/d_o$  and the abscissa is  $x/d_o$ . (b)The ordinate is  $(y/d_o)*10$  and the abscissa is  $x/d_o$ . 95
- 4.39 Comparison of the free surface profiles of a solitary wave with  $H/d_o=0.28$  running up on a  $2.88^\circ$  slope at non-dimensional time  $T=20$ . The solid line is the results of present model and the solid circles are the experimental data of Synolakis(1987), and the dash lines are the numerical results of WENO method by Ying Li(2000). 96

4.40	The velocity field of a solitary wave with $H/d_o=0.28$ running up on a $2.88^\circ$ slope from $x/d_o=28$ to $x/d_o=40$ at non-dimensional time $T=20$ . (a)The ordinate is $y/d_o$ and the abscissa is $x/d_o$ . (b)The ordinate is $(y/d_o)*10$ and the abscissa is $x/d_o$ .	97
4.41	Solitary wave run-up on a $2.88^\circ$ slope at $T=10$ . Comparisons of vertical variation of velocities at $x/d_o=24.15$ , $25.95$ , and $28.05$ . The wave crest is at $x/d_o=26.21$ . The lines are present model, and the circles are experiment by Lin, et al (1999)	99
4.42	Solitary wave run-up on a $2.88^\circ$ slope at $T=15$ . Comparisons of vertical variation of velocities at $x/d_o=30.15$ , $31.95$ , and $34.05$ . The wave crest is at $x/d_o=31.44$ . The lines are present model, and the circles are experiment by Lin, et al (1999)	100
4.43	Solitary wave run-up on a $2.88^\circ$ slope at $T=20$ . Comparisons of vertical variation of velocities at $x/d_o=34.95$ , and $36.15$ . The wave crest is at $x/d_o=36.76$ . The lines are present model, and the circles are experiment by Lin, et al (1999)	102
4.44	Definition of the half-buried pipe used by Foda (1990)	103
4.45	Comparison of water pressure of the present model and experiment (Foda, 1990) on exposed half-surface of pipe during one full wave cycle	105
4.46	Close-up of velocity field is around the sand basin and pipe by present model, while the wave crest just passes over the pipe.	106
4.47	Close-up of velocity field is around the sand basin and pipe by present model, while the wave trough just passes over the pipe.	107
4.48	Comparison of drag forces of present model, Morison equation, and experiment (Foda, 1990) on half-surface of pipe.	108
4-49	The layout of 120 inch outfall pipeline and the location of six positions used for the hydrodynamic force analysis at Orange County, California.	111
4.50	Variation of probable maximum wave height with recurrence interval at location 1 in Orange County, California, July 1997	113



4.51	Variation of probable maximum wave height with recurrence interval at location 2 in Orange County, California, July 1997	114
4.52	The vertical, horizontal, and resultant forces acting on a circular pipe at the depths of 40.65 ft and 47.75 ft in Orange County, California, July 1997	116
4.53	Comparison of drag forces of the present model with solitary and periodic waves and the report of Orange County Sanitation District at the depth of 40.65 ft	118
4.54	Comparison of lift forces of the present model with solitary and periodic waves and the report of Orange County Sanitation District at the depth of 40.65 ft	119
4.55	Comparison of resultant forces of the present model with solitary and periodic waves and the report of Orange County Sanitation District at the depth of 40.65 ft	120
4.56	Comparison of drag forces of the present model with solitary and periodic waves and the report of Orange County Sanitation District at the depth of 47.75 ft	122
4.57	Comparison of lift forces of the present model with solitary and periodic waves and the report of Orange County Sanitation District at the depth of 47.75 ft	123
4.58	Comparison of resultant forces of the present model with solitary and periodic waves and the report of Orange County Sanitation District at the depth of 47.75 ft	124

## **Abstract**

**Protections of coastal structures and coastal region from the attack of incident waves are important problems for coastal engineers. To solve these problems effectively and efficiently, the coastal engineers need more efficient tools for analyzing impacts of waves on structures in the planning and design of marine structures. The objective of this study is to develop a numerical model capable of predicting behavior of the non-breaking and near breaking solitary wave propagating in the coastal zone and the interactions of wave and coastal structure. The numerical model used in the study is called the Modified Marker-and-Cell (MODMAC) method which is a two-dimensional finite difference model. The equations modeled are the fully nonlinear, time dependent Navier-Stokes equation and the continuity equation. The wave profile of the propagating wave when interacting with coastal structure as well as the induced velocity field and the subsurface pressure are obtained in the whole flow field.**

**For the numerical analysis, both the Lagrangian and Eulerian methods are employed to track these massless markers along the free surface. The Eulerian methods are used in the following applications: (1) propagation of solitary waves in a**

# **Chapter 1**

## **Introduction**

### **Background**

Protections of coastal structures and coastal region from the attack of incident waves are important problems for coastal engineers. Many environmental factors have caused coastal disasters, among which are storm surge, beach erosion, extreme tropical cyclones, winter storm waves, tsunamis, earthquake and land subsidence. On June 15, 1896, a tsunamis resulting from an earthquake attacked Sanriku, Japan, and more than 27,000 people died and over 10,000 buildings were destroyed. A recent earthquake in Turkey on August 17, 1999, generated a tsunamis with a maximum run-up on the coast of 2.5 m. Indeed most of the damages associated with tsunamis are associated with their run-up at the shoreline. In 1995, the winter storm waves caused the leeside scour and damaged the Ventura breakwater. In addition, there was significant shoaling at the navigation channel in Ventura Harbor, California. The leeside scour and damage of the breakwater is caused by the rotational flow while the wave overtopping the rock sill. An understanding of wave actions is of vital importance in the design of many coastline facilities and harbor structures.

These coastal engineering problems can't be completely solved without the help of physical models or even prototype measurements. However, many coastal engineering problems associated with waves and currents can be analyzed or simulated by numerical models with different degree of accuracy. Numerical models, even though they are only approximations by nature, can have wider applications for real world coastal engineering problems. The finite difference method, the boundary element method, and the finite element method are three categories of numerical models.

Camfield and Street (1968) suggested that, to study the shoaling, breaking and run-up characteristics of catastrophic ocean waves, it is reasonable to begin by generating and studying simple finite-amplitude waves such as solitary wave. Such solitary waves can model many of the characteristics of tsunamis. Using a simple plane beach, important characteristics of the run-up tongue can be obtained both analytically and experimentally. (Synolakis,1986; Zelt,1991) In the shallow water region, the oscillatory waves are gradually transformed to become cnoidal wave with the limiting case approaching the solitary waves. In this sense the solitary waves can be considered a limiting case of the oscillatory wave and can be used to simulate the interaction of the wave and coastal structures. Because of the availability of a large amount of analytic results and experimental data on this

the drag and lift forces acting on the half-buried pipes. And the temporal variation of free surface elevation when the incident wave propagates over the submerged breakwater or over the sloping beach should be obtained simultaneously. The numerical model used in the study is called the Modified Marker-and-Cell (MODMAC) method that is a two-dimensional finite difference method. The computational process is simplified to solve the Navier-Stokes equations and the continuity equation. The numerical model was used to compute the wave profile, the velocity and the pressure. The numerical results for the wave overtopping the breakwater have been compared with the experimental data by Lee, Zhuang, and Chang (1993). The numerical solutions for the run-up problems compared with the experimental and numerical results by Pengzhi Lin (1999) and Ying Li (2000). The numerical solutions for the half-buried pipes have also been compared with the data generated for the Orange County Sanitation District in California (1998).

## **Chapter 2**

### **Review of Previous Research**

Many investigations have been conducted for wave propagations into the coastal zone as well as wave-structure interaction. In this chapter, some pertinent studies will be reviewed in its connection to the present investigation. In section 2.1 theoretical model on three classes of problem can be briefly reviewed. The experimental studies associated with the three classes of problem will be described in section 2.2. Numerical models used previously and their relevance to the present study will be presented in section 2.3.

#### **2.1 Theoretical Models:**

##### **2.1.1 Solitary Wave Overtopping the Submerged Breakwater:**

A linear inviscid model was used by Takano(1960) and Kirby and Dalrymple (1983). The model is based on a matched eigenfunction expansion technique, commonly used for studying surface wave propagation over abrupt transitions of water depth. The motion is governed by Laplace's equation:

$$V = \text{Re}(-e^{i\omega t} \nabla(\phi(x, y))), \quad \nabla^2 \phi = 0 \text{ in } \eta(x, t) < y < H(x), \quad -\infty < x < \infty$$

The linearized free-surface and bottom conditions are:

$$(\partial\phi/\partial y) + \omega^2 g^{-1}\phi = 0 \quad \text{on } y = 0 \text{ at free surface, and}$$

$$(\partial\phi/\partial n) = 0 \quad \text{on } y = H(x) \text{ at bottom}$$

Ting and Kim (1994) also used this method to obtain the surface wave profiles and the instantaneous velocity distributions near the submerged rectangular obstacle. Their results when compared to their experiments (1994) show that the linear inviscid model can't predict the rotational flow correctly on the lee side of the submerged rectangular obstacle. Therefore, it would be necessary to model the wave overtopping the submerged obstacle by using the viscous flow model.

### **2.1.2 Solitary Wave Running Up on Vertical Wall or Sloping Beach:**

The earlier work on long wave run-up relied on analytical approaches. To describe the analytical solutions for the solitary wave running up on the vertical wall, Latione(1960) used the perturbation method to obtain approximate solutions for the propagation of solitary waves in constant water depth unto vertical wall at one end of the wave tank. The normalized maximum run-up ( $R/d_0$ ) of solitary wave on the vertical wall obtained by Latione's approximation is,

$$R/d_0 = 2H' + \frac{H'^2}{2}$$

where  $H'$  is the normalized wave height  $= H/d_0$  and  $d_0$  is the constant water depth.

	$R/d_o$ $(\beta = 30^\circ, H/d_o = 0.17)$	$R/d_o$ $(\beta = 45^\circ, H/d_o = 0.48)$
Synolakis analytical solution(1987)	0.4067	1.1311
Lin, and et al. experiment(1999)	0.4306	1.2707

Pengzhi Lin and et al. (1999) employed an experiment, using the particle image velocimetry (PIV) technique, to investigate the free surface profile and also the spatial velocity distribution on the sloping beach. Their results show that the vertical variations of the horizontal velocity component increase linearly from bottom to free surface. The non-uniform vertical distribution of horizontal velocity component on the slope revealed that the long wave approximation used by the shallow water equations may not be adequate.

### 2.1.3 Wave Passing Over the Submarine Pipeline:

In the analysis of wave acting on the submarine pipelines on the seafloor, the unburied and buried pipelines are studied in the coastal engineering. The calculation of the hydrodynamic forces associated with wave action is crucial for the stability analysis of the pipeline. The vertical and horizontal forces,  $F_z(t)$  and  $F_x(t)$ , for a pipe with diameter  $D$  are usually calculated by the well known Morison equation,

$$F_x(t) = 0.5\rho DC_D|U(t)|U(t) + 0.25\rho\pi D^2C_M\dot{U}(t)$$

$$F_z(t) = 0.5\rho DC_LU^2(t)$$



where  $U(t)$  and  $\dot{U}(t)$  are the time-dependent total ambient water particle velocity and acceleration, and  $C_D$ ,  $C_M$  and  $C_L$  are time-invariant drag, inertia, and lift coefficients. The coefficients of Morison equation have been reported from the laboratory study of Bryndum et al. (1983), and from the field study by Grace and Zee.(1981) Due to the wake being swept back and forth over the pipe, the wake effect has been recognized for some time. Verley et al. (1989) developed a new hydrodynamic force model, called the wake model including wake velocity, for the prediction of forces on seabed pipelines. The wake model is,

$$F_x(t) = 0.5\rho DC_D(t)|U_w(t)|U_w(t) + 0.25\rho\pi D^2(C_M\dot{U}(t) - C_{AW}\dot{W}(t))$$

$$F_z(t) = 0.5\rho DC_L(t)U_w^2(t)$$

$$U_w = \text{wake velocity } (W(t)) + \text{ambient velocity } (U(t))$$

$C_{AW}$  is the added mass coefficient for the wake flow. Verley et al. (1989) employed an experiment and found that the wake model gave a better prediction of forces than the Morison equation.

Partial burial is a common configuration of submarine pipelines on the seafloor. Foda (1985) investigated half-buried marine pipe under the oscillatory loading of water waves. The hydrodynamic loading on the pipe is based on the assumption of the potential flow above the seabed. Only the vertical equilibrium of pipeline was considered under the wave-induced lifting force. Foda et al. (1990) conducted an

experiment to study the wave-induced force acting on the half-buried marine pipes and the breakout of this pipe. The Morison equation will be used to curve-fit the measured drag and lift forces on the exposed surface of the pipe. The best-fit coefficients of drag  $C_D$ , added mass  $C_M$ , and lift  $C_L$  can be obtained.

## **2.2 Experimental Studies:**

### **2.2.1 Solitary Wave Overtopping the Submerged Breakwater:**

The propagation of transient water wave over a submerged obstacle can be observed by experiments. Early investigators focused on the spatial variations of the water surface profile, but less concerned with the fluid kinematics near the submerged obstacle. Lee, Zhuang, and Chang (1993) conducted an experimental study on the propagation of solitary wave over a submerged obstacle. They found that (1) the overtopping wave constitutes a jet-like water mass which induces strong vortex in the vicinity of the shoreward region of the breakwater, (2) the oscillatory trains occur when the wave propagates over the breakwater. The vortex induces significant impacts on the shoreward face of the breakwater, and it can also scour the foundation of the breakwater and may damage the foundation region. Tsai, et al. (1986) showed that the critical failure areas in structures of caisson are the toe and the underlying foundation due to the wave-induced scouring, liquefaction and large stresses in the foundation soil. The oscillatory wave trains modify the frequency contents of the incident wave, thus the overtopping wave may affect the ship's

motions within the harbor basin. Ting and Kim's (1994) conducted laboratory experiments and found that there existed a region of formation and growth of separation responding directly to the wave transformation above the submerged obstacle. The interaction of the separated flow with the wave significantly modified the transmission process and consumed the wave energy.

### **2.2.2 Solitary Wave Running Up on Vertical Wall and Sloping Beach:**

Ippen and Kulin (1954) presented the results of an experimental study of the shoaling and breaking behavior of solitary waves. Camfield and Street (1968) simulated experimentally the shoaling, breaking and run-up of large amplitude long waves on a beach. Skjelbreia(1987) presented the velocity measurements in breaking solitary waves using the Laser Doppler Velocimetry(LDV). Since the LDV can only measure the time history of velocity at a point, it is difficult to obtain the global information of the entire flow field under a wave. Nishimura and Takewaka(1990) employed an imaging technique similar to the Particle Image Velocimetry(PIV) to measure the velocity field under the solitary waves that break either in constant water depth or on vertical wall. Pengzhi Lin, et al. (1999) employed the PIV technique to provide free surface profile and also the spatial velocity distribution in breaking solitary wave. LDV and PIV fail to measure velocity in the region where air bubble density becomes large. Therefore no velocity

data in the roller region of a breaking wave can be accurately measured using these methods.

### **2.2.3 Wave Passing Over the Submarine Pipeline:**

Summer et al. (1990) conducted an experiment and found that pipelines placed on an erodible bed may bury themselves due to action of waves and currents on the sediment in the neighborhood of the pipe. Cevik et al. (1999) presented an experimental investigation to determine the scour depth due to three vortices around the pipelines on the sloping beach. These pipelines might be destroyed partially or fully under the wave action and thus they may not be able to perform their functions.

Foda et al. (1990) conducted an experiment to study the wave-induced force acting on the half-buried marine pipes and the breakout of this pipe. The Morison equation was used to curve-fit the measured drag force on the exposed surface of the pipe. The Sanitation Districts of Orange County (1998) in California commissioned a large scale experimental investigation of forces acting on two different depths of the submarine outfall and its rock protection structure. The laboratory design wave used in the evaluation of forces acting on the pipe was obtained from U.S. Army Corps of Engineers and the Coast of California Storm and Tidal Wave Study. The forces were determined based on the velocity and

acceleration of the incident waves propagation in a direction perpendicular to the longitudinal axis of the outfall.

## **2.3 Numerical Models:**

### **2.3.1 Solitary Wave Overtopping the Submerged Breakwater:**

The early numerical model of ocean waves overtopping the submerged breakwater was based on inviscid irrotational flow. Kobayashi and Wurjanto (1989) developed a one-dimensional inviscid numerical model to predict the horizontal velocity and vertical elevation above the overtopping coastal structure located on the slope beach to assess the severity of the damage caused by the overtopping wave. Beji and Battjes(1993) presented a one-dimensional finite difference numerical model based on a time domain Boussinesq model. They developed an improved linear dispersion characteristic to solve relatively long waves propagating over a trapezoid submerged obstacle. The numerical model predicted the surface elevation of the wave before and after the submerged obstacle, and reproduced the details of the wave transformations over the submerged obstacle. But the numerical model, based on the nonviscous assumptions, again can't predict the flow field in the vicinity of the submerged breakwater. Zhuang and Lee(1994) developed a combined two-dimensional numerical model based on Boundary Element Method consisting of potential flow theory and vorticity stream function formulation. The vorticity stream function formulation was used in the vicinity of the shoreward

region of the breakwater. In the region away from the separation zone the potential theory by boundary element method was used. Although this numerical model successfully simulated the strong the vortex occurring around the submerged obstacle and the results did compare well with experimental data, the variations of free surface due to the combined rotational effect still were not investigated.

### **2.3.2 Solitary Wave Running Up on Vertical Wall or Sloping Beach:**

For practical problems with a wide range of wave parameters and complex beach geometry, numerical approaches are necessary. Hibberd and Peregrine(1979) obtained a numerical solution based on shallow water wave equation to describe the behavior of a uniform bore over a sloping beach and the subsequent run-up. Chubarov and Shokin(1987) presented the numerical model of long wave propagation, in particular for tsunami waves, in the framework of non-linear dispersion models of the Boussinesq and Korteweg-De Vries type using finite difference method. Based on the shallow water equation, which assume uniform horizontal velocity and hydrostatic pressure, Kobayashi et al.(1989) developed a numerical model based on the nonlinear shallow water equations to predict the run-up and overtopping problems. Their solutions have been shown to work well in simulating wave run-up and swash motions. Zelt(1991) parameterized the wave breaking with an artificial viscosity term in the momentum equation to obtain the solutions of run-up of non-breaking and breaking solitary waves on impermeable

beaches. He used a Lagrangian finite element method to solve the Boussinesq equation. Lemos(1992) developed a numerical model that solved the Reynolds Averaged Navier-Stokes (RANS) equations for the mean flow and the conventional  $k-\epsilon$  model for the turbulence field during the wave breaking. Lin and Liu(1998) presented a numerical model based on the RANS equations coupled with an improved  $k-\epsilon$  model using the nonlinear algebraic Reynolds stress closure assumption to study solitary wave run-up and run-down on beaches. Both velocity distributions of non-breaking and breaking solitary waves on beaches were investigated. Li(2000) developed a numerical model using the Weighted Essentially Non-Oscillatory (WENO) employed in gas dynamics to solve the nonlinear shallow water equations. It was found that the numerical scheme can predict the wave profile on the slope and maximum run-up very well.

The numerical solution of the Navier-Stokes equation for problems with free surface is complicated. The new position of the free surface should be obtained by solving a non-linear equation at each time. This problem has been solved by using finite difference method with a system of massless marker particles whose movements determine the position of the free surface at any particular time (Welch et al.(1966)). The numerical model used in the study is called the Modified Marker-and-Cell (MODMAC) method that is a two-dimensional finite difference method in solving continuity and Navier-Stokes equations. The method is useful in predicting

the non-breaking and near breaking solitary wave propagating into the coastal zone. The numerical model has been found to be convenient in computing the values of velocities and pressure. The numerical results obtained in the present study on the wave overtopping over the breakwater will be compared with the experimental data by Lee, Zhuang, and Chang(1993). The numerical solutions for the run-up problems will be compared with the experimental and numerical data by Pengzhi Lin (1999) and Ying Li(2000). The numerical solutions of the wave-induced forces on the half-buried pipes will be compared with the data of Orange County Sanitation in California (1998). These computed results will be presented in chapter 4.



## **Chapter 3**

### **Numerical Model**

The present Modified Marker-and-Cell (MODMAC) method is designed for simulating the unsteady motion of water waves in two space dimensions. In Section 3.1, the original Marker-and-Cell (MAC) method and Modified Marker-and-Cell (MODMAC) method are presented. In Section 3.2, the governing equations, the continuity and Navier-Stokes equations are described. The boundary conditions used in conjunction with the governing equations are presented in Section 3.3; the initial conditions are presented in Section 3.4. In Section 3.5, the discretised forms of the governing equations and the boundary conditions are presented.

#### **3.1 Marker and Cell Method**

Marker-and-Cell (MAC) method (Harlow and Welch, 1965) is one of the finite difference techniques that can be used to solve the nonlinear time dependent Navier-Stokes equations in two space dimensions including a free surface. The method is characterized by the staggered grid method (Fig. 3-1) in which velocities are centered at each cell boundaries and the pressures are centered at each cell. Working with the Poisson equation, which is obtained from momentum and continuity

equations, the pressure is computed. Substituting the computed pressure into the momentum equations, the new velocity is computed at each time step. In free surface flow problems, the massless marker particles, which are advanced by the local velocity field, move along the free surface to new positions at each time step. (Fletcher, 1991)

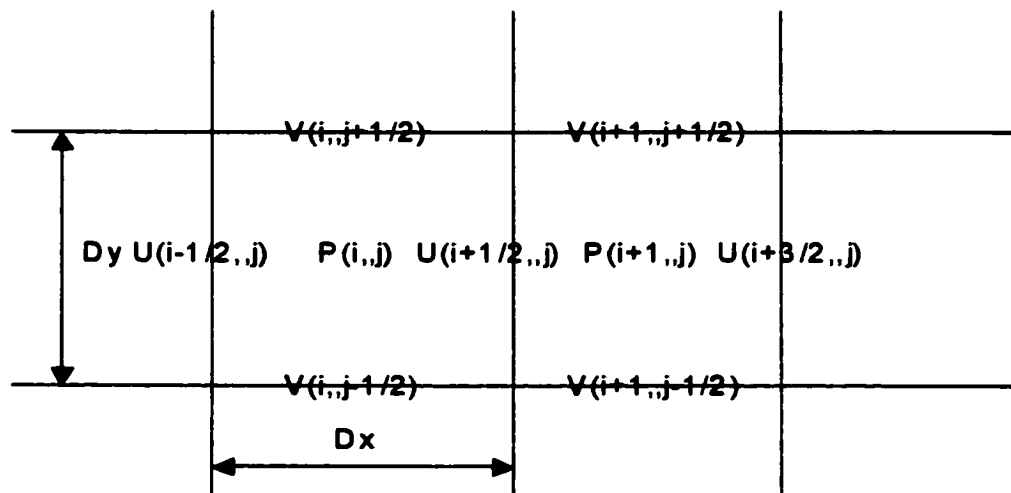


**Fig. 3-1 Cell setup and location of variables**

The method of computing the free surface positions in the MAC method is based on the Lagrangian formulation and can become unstable after a large number of time steps. To smooth out this difficulty, the Eulerian formulation is employed. The new formulation is an implicit scheme that has been shown to be stable after long time steps when applied to water waves propagating in the medium of constant water depth (Chan and Street 1970).

For problem of wave overtopping over a submerged breakwater, the present model modifies the MAC method with Eulerian formulation. The present model modifies the MAC method with Lagrangian formulation as well as special velocity adjustments near the intersection of the free surface and the sloping boundary for simulation of wave run-up on the sloping beach. The entire flow field is covered with rectangular mesh of cells, the space increments are  $\delta x$  and  $\delta y$  (or  $dx$  and  $dy$ ). The center of cell is designated by the indices  $i$  and  $j$ , where  $i$  is the column in  $x$  direction and  $j$  is the row in  $y$  direction of a Cartesian coordinate system. The fluid velocity components  $u$  and  $v$  and the pressure  $p$  are the dependent variables while the  $x$  and  $y$  and time  $t$  are independent variables in the problem.

### 3.2 Governing Equations

The present modified Marker-and-Cell method is designed for simulating the unsteady motion of water wave overtopping the rectangular breakwater and the run-up on the sloping beach in two-dimensional spaces. The viscous fluid is assumed incompressible. The governing equations are defined as follows:

For flow of constant density (incompressible flow), the continuity equation reduces to

$$\frac{\partial u}{\partial x} + \frac{\partial v}{\partial y} = 0 \quad (3.2.1)$$

The dimensionless Navier-Stokes equations are simplified as:

$$\frac{\partial u}{\partial t} + u \frac{\partial u}{\partial x} + v \frac{\partial u}{\partial y} = -\frac{\partial p}{\partial x} + g_x + \frac{1}{Re} \left( \frac{\partial^2 u}{\partial x^2} + \frac{\partial^2 u}{\partial y^2} \right) \quad (3.2.2)$$

$$\frac{\partial v}{\partial t} + u \frac{\partial v}{\partial x} + v \frac{\partial v}{\partial y} = -\frac{\partial p}{\partial y} + g_y + \frac{1}{Re} \left( \frac{\partial^2 v}{\partial x^2} + \frac{\partial^2 v}{\partial y^2} \right) \quad (3.2.3)$$

where  $x=x/d_o$ ,  $y=y/d_o$  are the normalized space variables;  $u=u/\sqrt{gd_o}$ ,  $v=v/\sqrt{gd_o}$  are the normalized velocity components in the x and y directions;  $p=p/\rho gd_o$  is the normalized pressure;  $\rho$  is the density of the fluid;  $g_x = g_x/g$  and  $g_y = g_y/g$  are the x, y components of gravity acceleration;  $t=t/\sqrt{d_o/g}$  is the dimensionless time variable;  $d_o$  = undisturbed water depth;  $\mu$  is the viscosity and the Reynolds number is defined as  $Re=\rho u d_o/\mu$ .

### 3.3 Boundary Conditions

Two types of boundary conditions are employed in this study (Figure 3.2.1).

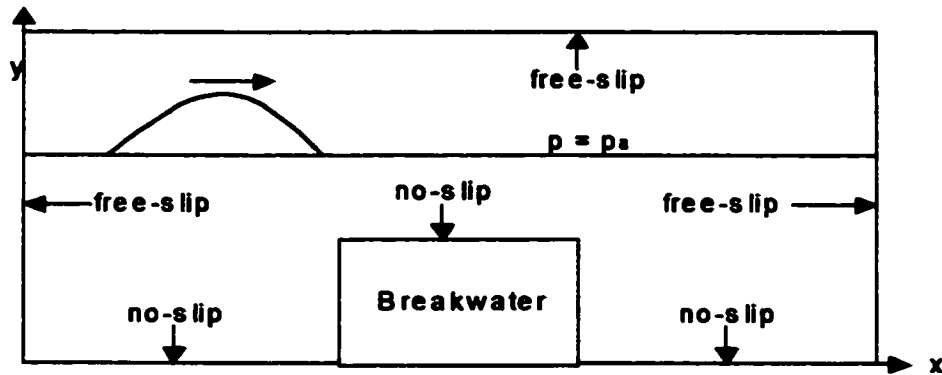


Fig. 3.2.1 Sketch of boundary conditions

First type of boundary conditions are specified at the domain of interest for computation; the free-slip horizontal solid boundaries are,

$$\left( v = 0, \quad \frac{\partial u}{\partial y} = 0, \quad \text{and} \quad \frac{\partial p}{\partial y} = g_y \right) \quad (3.3.1)$$

the free-slip vertical solid boundaries are,

$$\left( u = 0, \quad \frac{\partial v}{\partial x} = 0, \quad \text{and} \quad \frac{\partial p}{\partial x} = g_x \right) \quad (3.3.2)$$

Second type of boundary conditions is employed at the submerged breakwater surfaces and the bed i.e. the no-slip conditions are specified at the horizontal solid boundaries are,

$$\left( u = 0, \quad \frac{\partial v}{\partial y} = 0, \quad \text{and} \quad \frac{\partial p}{\partial y} = g_y + \frac{1}{R_e} \left( \frac{\partial^2 v}{\partial y^2} \right) \right) \quad (3.3.3)$$

At the vertical solid boundaries are no slip condition are also specified,

$$\left( v = 0, \quad \frac{\partial u}{\partial x} = 0, \quad \text{and} \quad \frac{\partial p}{\partial x} = g_x + \frac{1}{R_e} \left( \frac{\partial^2 u}{\partial x^2} \right) \right) \quad (3.3.4)$$

The boundary conditions at the free surface are defined as the interface between a liquid and a massless gas. For incompressible fluids with very low viscosity, such as water, it can be,

$$p = p_a(x, t) \quad (3.3.5)$$

Where  $P_a$  is the applied pressure on the free surface, for the present model  $P_a$  can be set to zero.

The boundary conditions on the sloping beach are defined as (Figure 3.2.2),

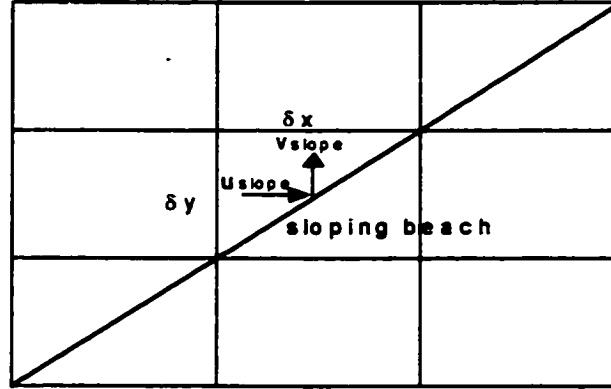


**Figure 3.2.2 boundary condition of sloping beach**

$$v_{slope} = u_{slope} \frac{\delta y}{\delta x} \quad (3.3.6)$$

where  $\delta x$  and  $\delta y$  are space increments and  $u_{slope}$  is derived from Section 3.5.

Based on equation (3.3.6), the flow field will move along the diagonal of the cells.

### 3.4 Initial Conditions

Theoretically, the length  $L$  of a solitary wave is infinite, so it is desirable to define a finite, practical length for a solitary wave. The main consideration is that the initial wave crest should be far enough from any obstacles and vertical walls.

According to Laitone's formulas,(Laitone (1960))

$$\frac{L}{d_o} = 6.9 \left( \frac{d_o}{H} \right)^{\frac{1}{2}} \quad (3.4.1)$$

where  $d_o$  is the still water depth and  $H$  is the wave height of the solitary wave.

The wave profile ( $y_s$ ) may be calculated from the classical formula of Boussinesq:

$$y_s(x) = d_o + H \sec h^2 \left[ \sqrt{\frac{3H}{4d_o}} \left( \frac{x - x_{CR}}{d_o} \right) \right] \quad (3.4.2)$$

where  $x_{CR}$  is the location between the wave crest and left-hand vertical wall.

The wave speed  $C$  can be evaluated by the following infinite series Laitone (1960),

$$\frac{C}{\sqrt{gd_o}} = 1 + \frac{1}{2} \left( \frac{H}{d_o} \right) - \frac{3}{20} \left( \frac{H}{d_o} \right)^2 + \dots \quad (3.4.3)$$

The velocities are computed by

$$u = C + \frac{\partial \psi}{\partial y} \quad ; \quad v = -\frac{\partial \psi}{\partial x} \quad (3.4.4)$$

and the stream function is obtained from Laplace's equation

$$\frac{\partial^2 \psi}{\partial x^2} + \frac{\partial^2 \psi}{\partial y^2} = 0 \quad (3.4.5)$$

### 3.5 Finite Difference Scheme

The computation region is divided into a number of rectangular cells as shown in Fig.3-1. The pressures are defined at the center of each cell and that velocity components are defined at each center point of the cell boundaries. Such an arrangement is very convenient for solving equations (3.2.2) and (3.2.3).

By incorporating the continuity equation into the convection acceleration terms, one obtains the following relationship:

$$u \frac{\partial u}{\partial x} + v \frac{\partial u}{\partial y} = \frac{\partial u^2}{\partial x} + \frac{\partial uv}{\partial y}$$

$$u \frac{\partial v}{\partial x} + v \frac{\partial v}{\partial y} = \frac{\partial uv}{\partial x} + \frac{\partial v^2}{\partial y}$$

Equations (3.2.2) and (3.2.3) can be rearranged as follows:

$$\frac{\partial u}{\partial t} + \frac{\partial u^2}{\partial x} + \frac{\partial uv}{\partial y} = -\frac{\partial p}{\partial x} + g_x + \frac{1}{R_e} \left( \frac{\partial^2 u}{\partial x^2} + \frac{\partial^2 u}{\partial y^2} \right) \quad (3.5.1)$$

$$\frac{\partial v}{\partial t} + \frac{\partial vu}{\partial x} + \frac{\partial v^2}{\partial y} = -\frac{\partial p}{\partial y} + g_y + \frac{1}{R_e} \left( \frac{\partial^2 v}{\partial x^2} + \frac{\partial^2 v}{\partial y^2} \right) \quad (3.5.2)$$



In discretising the equations (3.2.1), (3.5.1), and (3.5.2), the following finite difference expressions are used:

$$\left[ \frac{\partial u}{\partial t} \right]_{i+\frac{1}{2}j} = \frac{\left( u_{i+\frac{1}{2}j}^{n+1} - u_{i+\frac{1}{2}j}^n \right)}{\delta t} + o(\delta t),$$

$$\left[ \frac{\partial u^2}{\partial x} \right]_{i+\frac{1}{2}j} = \frac{(u_{i+1j}^2 - u_{ij}^2)}{\delta x} + o(\delta x^2),$$

$$\left[ \frac{\partial (uv)}{\partial y} \right]_{i+\frac{1}{2}j} = \frac{((uv)_{i+\frac{1}{2}j+\frac{1}{2}} - (uv)_{i+\frac{1}{2}j-\frac{1}{2}})}{\delta y} + o(\delta y^2),$$

$$\left[ \frac{\partial^2 u}{\partial x^2} \right]_{i+\frac{1}{2}j} = \frac{\left( u_{i+\frac{3}{2}j} - 2u_{i+\frac{1}{2}j} + u_{i-\frac{1}{2}j} \right)}{\delta x^2} + o(\delta x^2),$$

$$\left[ \frac{\partial^2 u}{\partial y^2} \right]_{i+\frac{1}{2}j} = \frac{\left( u_{i+\frac{1}{2}j-1} - 2u_{i+\frac{1}{2}j} + u_{i+\frac{1}{2}j+1} \right)}{\delta y^2} + o(\delta y^2),$$

$$\left[ \frac{\partial p}{\partial x} \right]_{i+\frac{1}{2},j} = \frac{(p_{i+1,j} - p_{i,j})}{\delta x} + o(\delta x^2).$$

Equations, (3.5.1), (3.5.2) and (3.2.1) can be approximated by the finite difference equation for cell (i,j) as follows:

$$u_{i+\frac{1}{2},j}^{n+1} = u_{i+\frac{1}{2},j}^* + \delta t * g_x + \frac{\delta t}{\delta x} (p_{i,j} - p_{i+1,j}) \quad (3.5.3)$$

$$v_{i,j+\frac{1}{2}}^{n+1} = v_{i,j+\frac{1}{2}}^* + \delta t * g_y + \frac{\delta t}{\delta y} (p_{i,j} - p_{i,j+1}) \quad (3.5.4)$$

$$D_{ij}^{n+1} = -\frac{u_{i+\frac{1}{2},j}^{n+1} - u_{i-\frac{1}{2},j}^{n+1}}{\delta x} + \frac{v_{i,j+\frac{1}{2}}^{n+1} - v_{i,j-\frac{1}{2}}^{n+1}}{\delta y} = 0 \quad (3.5.5)$$

Variables lacking a superscript are evaluated at the  $n$ th time step (the old time) and  $D_{ij}$  is the velocity divergence. The  $u^*$ ,  $v^*$  constitute velocities at the  $n+1$  time step (the new time).

$$u_{i+\frac{1}{2},j}^* = u_{i+\frac{1}{2},j} + \delta t \left[ \frac{u_{ij}^2 - u_{i+1,j}^2}{\delta x} + \frac{(uv)_{i+\frac{1}{2},j-\frac{1}{2}} - (uv)_{i+\frac{1}{2},j+\frac{1}{2}}}{\delta y} + \frac{\left( u_{i+\frac{3}{2},j}^2 - 2u_{i+\frac{1}{2},j}^2 + u_{i-\frac{1}{2},j}^2 \right)}{Re\delta x^2} + \frac{\left( u_{i+\frac{1}{2},j-1}^2 - 2u_{i+\frac{1}{2},j}^2 + u_{i+\frac{1}{2},j+1}^2 \right)}{Re\delta y^2} \right] \quad (3.5.6)$$

$$v_{i,j+\frac{1}{2}}^* = v_{i,j+\frac{1}{2}} + \delta t \left[ \frac{v_{ij}^2 - v_{ij+1}^2}{\delta y} + \frac{(uv)_{i+\frac{1}{2},j+\frac{1}{2}} - (uv)_{i-\frac{1}{2},j+\frac{1}{2}}}{\delta x} + \frac{\left( v_{i+\frac{1}{2},j+\frac{1}{2}} - 2v_{i,j+\frac{1}{2}} + v_{i-\frac{1}{2},j+\frac{1}{2}} \right)}{Re\delta x^2} + \frac{\left( v_{i,j+\frac{3}{2}} - 2v_{i,j+\frac{1}{2}} + v_{i,j-\frac{1}{2}} \right)}{Re\delta y^2} \right] \quad (3.5.7)$$

In discretising (3.5.6), (3.5.7) the following finite difference expressions are used:

$$u_{i,j} = \frac{1}{2} \left( u_{i+\frac{1}{2},j} + u_{i-\frac{1}{2},j} \right)$$

$$v_{i,j} = \frac{1}{2} \left( v_{i,j+\frac{1}{2}} + v_{i,j-\frac{1}{2}} \right)$$

$$(uv)_{i+\frac{1}{2},j+\frac{1}{2}} = \frac{1}{2} \left( u_{i+\frac{1}{2},j} + u_{i+\frac{1}{2},j+1} \right) * \frac{1}{2} \left( v_{i,j+\frac{1}{2}} + v_{i+1,j+\frac{1}{2}} \right) \quad (3.5.8)$$

Substituting equations (3.5.3) and (3.5.4) into equation (3.5.5) and requiring  $D_{i,j,n+1} = 0$  leads the pressure equation:

$$\frac{p_{i+1,j} - 2p_{ij} + p_{i-1,j}}{\delta x^2} + \frac{p_{i,j+1} - 2p_{ij} + p_{i,j-1}}{\delta y^2} = -R_{ij} \quad (3.5.9)$$

or

$$p_{ij} = \frac{1}{Z} \left( \frac{p_{i+1j} + p_{i-1j}}{\delta x^2} + \frac{p_{ij+1} + p_{ij-1}}{\delta y^2} + R_{ij} \right) \quad (3.5.10)$$

where

$$Z = 2 \left( \frac{1}{\delta x^2} + \frac{1}{\delta y^2} \right) \quad (3.5.11)$$

$$R_{ij} = -\frac{1}{\delta t} \left[ \frac{u_{i+\frac{1}{2}j}^* - u_{i-\frac{1}{2}j}^*}{\delta x} + \frac{v_{ij+\frac{1}{2}}^* - v_{ij-\frac{1}{2}}^*}{\delta y} \right] \quad (3.5.12)$$

Equation (3.5.9) is called a finite-difference Poisson equation whose corresponding partial differential equation is

$$\left( \frac{\partial^2 p}{\partial x^2} \right)_{ij} + \left( \frac{\partial^2 p}{\partial y^2} \right)_{ij} = -R_{ij} \quad (3.5.13)$$

Near the free surface, the pressure  $p = p_a$  is applied at the exact location of the surface and not in a nearby cell center where  $p$  is usually defined. Let  $\eta_1, \eta_2, \eta_3, \eta_4$ ;  $P_1, P_2, P_3, P_4$  be the lengths and pressures of the four segments of the irregular star depicted in (Fig.3-3).  $\eta_1$  is the length of  $p_1$  to  $p_{ij}$ ;  $\eta_2$  is  $p_2$  to  $p_{ij}$ ;  $\eta_3$  is  $p_3$  to  $p_{ij}$ ;  $\eta_4$  is  $p_4$  to  $p_{ij}$ . By expanding  $P_1, P_2, P_3, P_4$  in terms of Taylor series expansions about the point  $(i,j)$ , it can be shown that equation (3.5.13) is approximated by

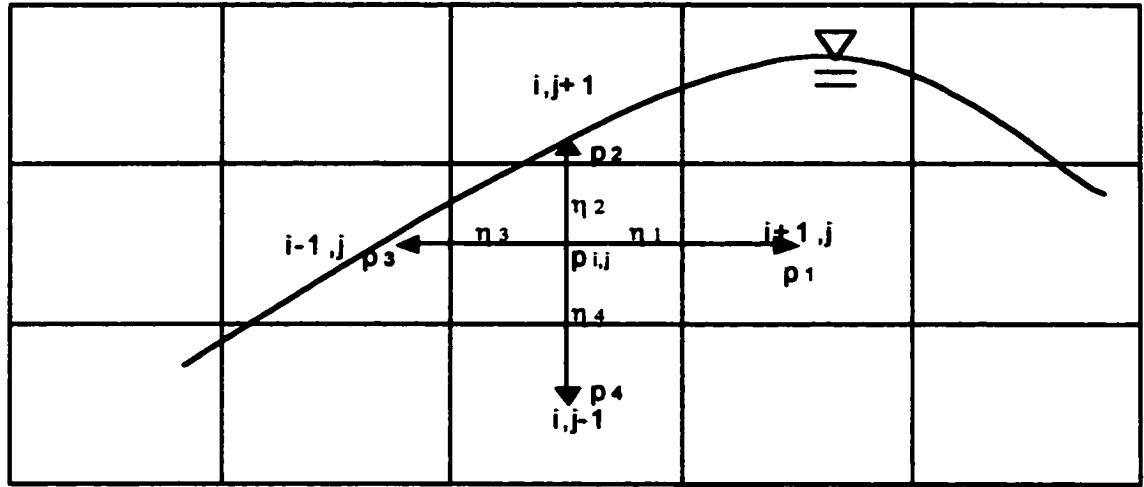


**Fig. 3-3 Interpolation of pressure  $P_{ij}$  near the free surface**

$$p_1 = p_{ij} + \eta_1 \left( \frac{\partial p}{\partial x} \right)_{ij} + \frac{\eta_1^2}{2} \left( \frac{\partial^2 p}{\partial x^2} \right)_{ij} + o(\eta_1^3) \quad (3.5.14)$$

$$p_3 = p_{ij} - \eta_3 \left( \frac{\partial p}{\partial x} \right)_{ij} + \frac{\eta_3^2}{2} \left( \frac{\partial^2 p}{\partial x^2} \right)_{ij} - o(\eta_3^3) \quad (3.5.15)$$

$$p_4 = p_{ij} - \eta_4 \left( \frac{\partial p}{\partial y} \right)_{ij} + \frac{\eta_4^2}{2} \left( \frac{\partial^2 p}{\partial y^2} \right)_{ij} - o(\eta_4^3) \quad (3.5.16)$$

$$p_2 = p_{ij} + \eta_2 \left( \frac{\partial p}{\partial y} \right)_{ij} + \frac{\eta_2^2}{2} \left( \frac{\partial^2 p}{\partial y^2} \right)_{ij} + o(\eta_2^3) \quad (3.5.17)$$

Neglecting  $\eta_i$  ( $i=1,2,3,4$ ) terms of the third or higher order, we eliminate the first

derivative of  $P_{ij}$  terms between (3.5.14) and (3.5.15); (3.5.16) and (3.5.17), thus we obtain the following expression for second derivation of P.

$$\left(\frac{\partial^2 p}{\partial x^2}\right)_{ij} = \frac{2}{\eta_1 \eta_3 (\eta_1 + \eta_3)} [\eta_3 p_1 + \eta_1 p_3 - (\eta_1 + \eta_3) p_{ij}] \quad (3.5.18)$$

$$\left(\frac{\partial^2 p}{\partial y^2}\right)_{ij} = \frac{2}{\eta_2 \eta_4 (\eta_2 + \eta_4)} [\eta_4 p_2 + \eta_2 p_4 - (\eta_2 + \eta_4) p_{ij}] \quad (3.5.19)$$

Substituting equations (3.5.18) and (3.5.19) into equation (3.5.13), we obtain

$$p_{ij} = \frac{\eta_1 \eta_2 \eta_3 \eta_4}{2(\eta_2 \eta_4 + \eta_1 \eta_3)} \left[ \frac{\eta_3 p_1 + \eta_1 p_3}{\eta_1 \eta_3 \left(\frac{\eta_1 + \eta_3}{2}\right)} + \frac{\eta_4 p_2 + \eta_2 p_4}{\eta_2 \eta_4 \left(\frac{\eta_2 + \eta_4}{2}\right)} + R_{ij} \right] \quad (3.5.20)$$

Equation (3.5.20) will be used at cells near free surface. It is reduced to equation (3.5.10), when it is applied to interior cells.

Equation (3.5.10) and equation (3.5.20) are solved for pressures P at each time step by using an iterative technique called Successive Over-Relaxation method. After pressures P have been obtained and substituted into equations (3.5.3) and (3.5.4), velocities  $u_{i+1/2,j}$ ,  $v_{i,j+1/2}$  are solved at the new time step.

The free surface particles move to their new locations according to their locally interpolated values of u and v. Considering the particle k in Fig.3-4, we can find the velocity component  $u_k$  for the particle by making a Taylor series expansion about 0. Neglecting the third and higher order terms, we obtain:

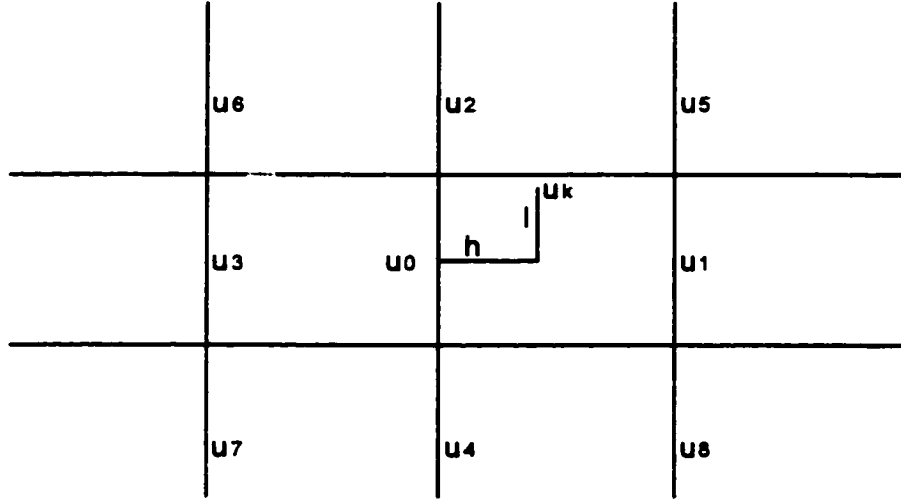


**Fig. 3-4 Interpolation of velocity  $u_k$  at the particle  $k$**

$$\begin{aligned}
 u_k &= u_0 + h \left( \frac{\partial u}{\partial x} \right)_0 + l \left( \frac{\partial u}{\partial y} \right)_0 + \frac{1}{2!} \left[ h^2 \left( \frac{\partial^2 u}{\partial x^2} \right)_0 + 2hl \left( \frac{\partial^2 u}{\partial x \partial y} \right)_0 + l^2 \left( \frac{\partial^2 u}{\partial y^2} \right)_0 + \dots \right] \\
 &\approx u_0 + \left( \frac{h}{\delta x} \right) \left( \frac{u_1 - u_3}{2} \right) + \left( \frac{l}{\delta y} \right) \left( \frac{u_2 - u_4}{2} \right) + \frac{1}{2} \left[ \left( \frac{h}{\delta x} \right)^2 (u_1 + u_3 - 2u_0) + \left( \frac{l}{\delta y} \right)^2 (u_2 + u_4 - 2u_0) \right] \\
 &\quad + \frac{1}{4} \left( \frac{h}{\delta x} \right) \left( \frac{l}{\delta y} \right) (u_5 - u_6 + u_7 - u_8)
 \end{aligned}
 \tag{3.5.21}$$

In a similar manner, a formula can be derived to calculate the y-component velocity  $v_k$  of the particle  $k$ .

$$\begin{aligned}
v_k &= v_0 + h \left( \frac{\partial v}{\partial x} \right)_0 + l \left( \frac{\partial v}{\partial y} \right)_0 + \frac{1}{2!} \left[ h^2 \left( \frac{\partial^2 v}{\partial x^2} \right)_0 + 2hl \left( \frac{\partial^2 v}{\partial x \partial y} \right)_0 + l^2 \left( \frac{\partial^2 v}{\partial y^2} \right)_0 + \dots \right] \\
&\approx v_0 + \left( \frac{h}{\delta x} \right) \left( \frac{v_1 - v_3}{2} \right) + \left( \frac{l}{\delta y} \right) \left( \frac{v_2 - v_4}{2} \right) + \frac{1}{2} \left[ \left( \frac{h}{\delta x} \right)^2 (v_1 + v_3 - 2v_0) + \left( \frac{l}{\delta y} \right)^2 (v_2 + v_4 - 2v_0) \right] \\
&\quad + \frac{1}{4} \left( \frac{h}{\delta x} \right) \left( \frac{l}{\delta y} \right) (v_5 - v_6 + v_7 - v_8)
\end{aligned} \tag{3.5.22}$$

With  $u_k$  and  $v_k$  computed, each free surface particle is advanced by Eulerian method,

Let  $\eta$  be the height of the free surface. The kinematics condition at the free surface is,

$$\frac{D\eta}{Dt} = v \tag{3.5.23}$$

which can be expanded to

$$\frac{\partial \eta}{\partial t} = v - u \frac{\partial \eta}{\partial x} \tag{3.5.24}$$

The forward implicit method is used to differentiate equation (3.5.24) as follows,

$$\frac{\eta_k^{n+1} - \eta_k^n}{\delta t} = v_k - u_k \left( \frac{\eta_{k+1}^{n+1} - \eta_{k-1}^{n+1}}{2\Delta} \right) \tag{3.5.25}$$

or

$$-\frac{\alpha}{2} \eta_{k-1}^{n+1} + \eta_k^{n+1} + \frac{\alpha}{2} \eta_{k+1}^{n+1} = \eta_k^n + \delta t v_k \tag{3.5.26}$$



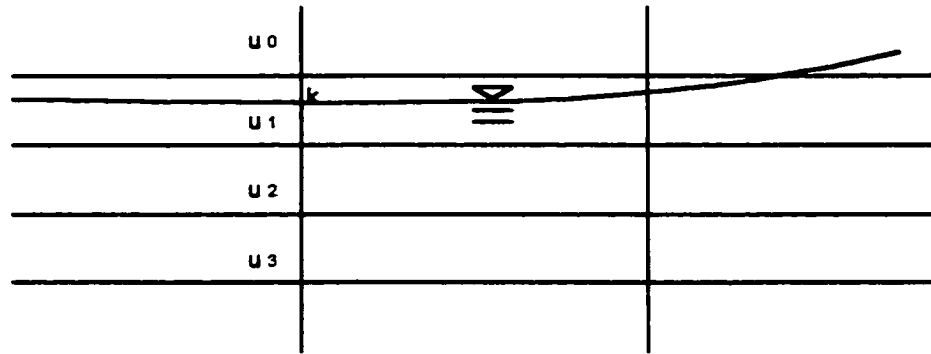


**Fig. 3-5 Outside domain velocity from extrapolation of interior fluid**

$$u_0 = 2u_1 - u_2 \quad (3.5.28)$$

As to the application of conditions at solid boundaries, consider the vertical wall that constitutes the right-hand boundary and horizontal wall that constitutes the bottom boundary in Fig. 3-6. Similarly, conditions may be derived for other vertical and horizontal boundaries.

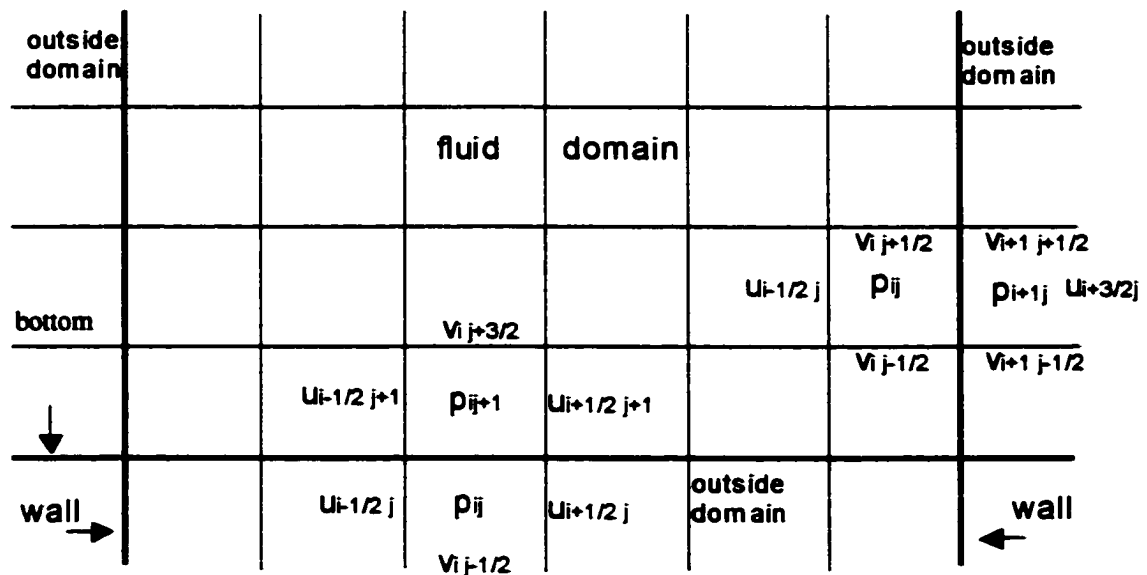


**Fig. 3-6 Boundary orientation in relation to the staggered grid**

The finite-difference formula of equation (3.3.1) at the horizontal free-slip boundary is as follows:

$$v_{i,j+\frac{1}{2}} = 0; u_{i+\frac{1}{2},j+1} = u_{i+\frac{1}{2},j}; u_{i-\frac{1}{2},j+1} = u_{i-\frac{1}{2},j};$$

$$p_{ij} = p_{i,j+1} - \delta y g_y$$
(3.5.29)

Equation (3.3.2) at the vertical free-slip boundary is as follows:

$$u_{i+\frac{1}{2},j} = 0; v_{i+1,j+\frac{1}{2}} = v_{i,j+\frac{1}{2}}; v_{i+1,j-\frac{1}{2}} = v_{i,j-\frac{1}{2}};$$

$$p_{i+1,j} = p_{ij} + \delta x g_x$$
(3.5.30)

The finite-difference formula of equation (3.3.3) at the horizontal no-slip boundary is expressed as follows:

$$u_{i+\frac{1}{2},j+\frac{1}{2}} = 0; u_{i+\frac{1}{2},j} = -u_{i+\frac{1}{2},j+1};$$

$$u_{i-\frac{1}{2},j+\frac{1}{2}} = 0; u_{i-\frac{1}{2},j} = -u_{i-\frac{1}{2},j+1};$$

$$v_{i,j-\frac{1}{2}} = v_{i,j+\frac{3}{2}}$$
(3.5.31)

$$p_{ij} = p_{i,j+1} - \delta y g_y - \frac{1}{R_e} \left( \frac{v_{i,j+\frac{3}{2}} - 2v_{i,j+\frac{1}{2}} + v_{i,j-\frac{1}{2}}}{\delta y^2} \right)$$

Similarly, equation (3.3.4) at the vertical no-slip boundary is expressed as follows:

**(3.5.32)**

$$\begin{aligned}
M_1 &= -\delta x v_{i+1/2, j+1/2} \left( \frac{u_{i+1/2, j} + u_{i+3/2, j+1}}{2} \right) \\
M_2 &= \delta y \left( \frac{u_{i-1/2, j} + u_{i+1/2, j}}{2} \right)^2 - \delta x \left( \frac{v_{ij-1/2} + v_{ij+1/2}}{2} \right) \left( \frac{u_{i-1/2, j} + u_{i+1/2, j}}{2} \right) \\
M_3 &= \delta x v_{ij-1/2} \left( \frac{u_{i+1/2, j} + u_{i-1/2, j-1}}{2} \right)
\end{aligned} \tag{3.5.33}$$

The area of the control volume is  $\delta x \delta y$ . Therefore, by relating the net inflow of the u-momentum to its rate of increase, we obtain

$$\left( \frac{u_{i+1/2, j}^* - u_{i+1/2, j}}{\delta t} \right) (\delta x \delta y) = M_1 + M_2 + M_3 \tag{3.5.34}$$

It can be further be rearranged as:

$$u_{i+1/2, j}^* = u_{i+1/2, j} + \frac{\delta t}{\delta x \delta y} (M_1 + M_2 + M_3) \tag{3.5.35}$$

The total  $u_{i+1/2, j}^{n+1}$  on the sloping boundary can be obtained as follows:

$$u_{i+\frac{1}{2}, j}^{n+1} = u_{i+\frac{1}{2}, j}^* + \delta t * g_x + \frac{\delta t}{\delta x} (p_{ij} - p_{i+1, j}) \tag{3.5.36}$$

It is noted that equation (3.5.36) is derived by substituting equation (3.5.35) into equation (3.5.3).

Substitution of equation (3.5.35) into the equation (3.3.6) leads to the computation of the value  $v_{i+1/2}^{n+1}$ . The total  $v_{i+1/2}^{n+1}$  on the sloping boundary is then

$$v_{i+1/2}^{n+1} = v_{i+1/2}^* + \delta t * g_y + \frac{\delta t}{\delta y} (p_{ij} - p_{i,j+1}) \quad (3.5.37)$$

The pressure  $P_{ij}$  (Figure 3.8), which lies on the sloping beach, can be derived from the conservation of mass in the following expression:

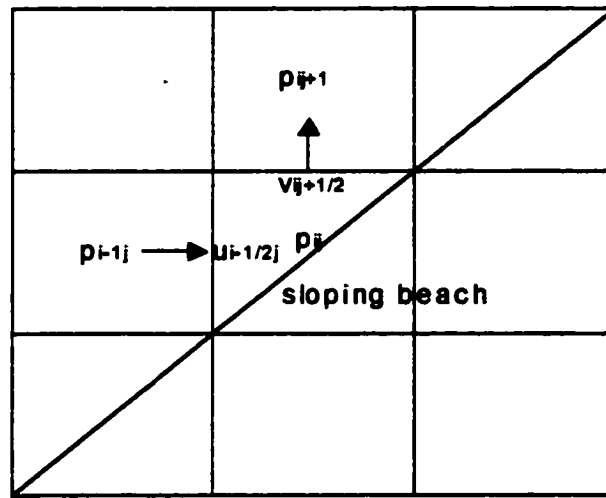


Figure 3.8 sketch of pressure  $p$  on sloping boundary

$$u_{i-1/2,j}^{n+1} \delta y - v_{i,j+1/2}^{n+1} \delta x = 0 \quad (3.5.38)$$

An analog of equation (3.5.36) and (3.5.37) can be used to evaluate  $u_{i-1/2,j}^{n+1}$  and  $v_{i,j+1/2}^{n+1}$  by

$$u_{i-1/2j}^{n+1} = u_{i-1/2j}^* + \delta t * g_x + \frac{\delta t}{\delta x} (p_{i-1j} - p_{ij}) \quad (3.5.39)$$

$$v_{ij+1/2}^{n+1} = v_{ij+1/2}^* + \delta t * g_y + \frac{\delta t}{\delta y} (p_{ij} - p_{ij+1}) \quad (3.5.40)$$

Substitution of equation (3.5.39) and (3.5.40) into equation (3.5.38) leads to

$$p_{ij} = \frac{1}{\frac{1}{\delta x^2} + \frac{1}{\delta y^2}} \left( \frac{p_{i-1j}}{\delta x^2} + \frac{p_{ij+1}}{\delta y^2} + R_{ij} \right) \quad (3.5.41)$$

where

$$R_{ij} = \frac{1}{\delta t} \left( \frac{u_{i-1/2j}^*}{\delta x} - \frac{v_{ij+1/2}^*}{\delta y} \right) + \left( \frac{g_x}{\delta x} - \frac{g_y}{\delta y} \right) \quad (3.5.42)$$

For analyzing the run-up of waves on a sloping beach, the special velocity adjustment near the intersection of free surface and the sloping boundary is shown in Figure 3.9.

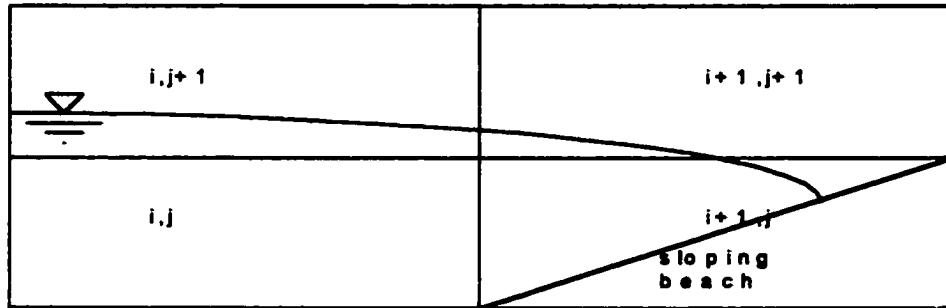


**Figure 3.9 propagation of velocities near the intersection of free surface and sloping boundary**

If the cell (i,j) is defined as the free surface cell, i.e. the marker particle is inside the cell, or the cell (i,j) is defined as the full cell, and the cell (i+1,j) is the sloping boundary, then the following relations are established:

$$\begin{aligned} u_{i+1/2,j} &= u_{i-1/2,j} \\ v_{i+1,j+1/2} &= u_{i+1/2,j} * \Delta y / \Delta x \end{aligned} \quad (3.5.43)$$

Eq.(3.5.20), Eq.(3.5.3), and Eq.(3.5.4) are used to compute the pressure and the values of velocity u, v for various conditions. Substituting velocity u, v into Eq.(3.5.21) and Eq.(3.5.22), the surface particles are advanced by Eulerian formulation Eq. (3.5.26) or Lagrangian formulation Eq. (3.5.27). The results of the numerical model will be presented in Chapter 4.

## **Chapter 4**

### **Presentation and Discussion of Modeling Results**

Application of the numerical model described in Chapter 3 has been made to a number of practical problems in coastal engineering. Wherever possible, available experimental data are used to compare with the results of the computer model. In Section 4.1, results on wave overtopping a submerged rectangular breakwater are presented and compared with available experimental data. In Section 4.2, model results on run-up of a solitary wave on a vertical wall are presented. The model results are also compared with a number of experiments conducted by previous investigators. Results on the run-up of solitary wave on sloping beaches with various beach slopes are presented in Section 4.3. Results of computer simulation on wave-induced loading on various semi-buried pipes are presented in Section 4.4. The computed results are also compared with the experimental data obtained by other investigators.

#### **4.1 Wave Overtopping on the Submerged Rectangular Structure**

In order to verify the present numerical model, the present numerical model has been applied to several breakwater configurations where experiments conducted in



the laboratory wave tank were available (Lee et al. (1993)). The computational domain is shown in Fig. 4-1. The initial position of the solitary wave crest is chosen such that neither the left-hand wall nor the breakwater influenced the wave at the beginning of the computer simulation.

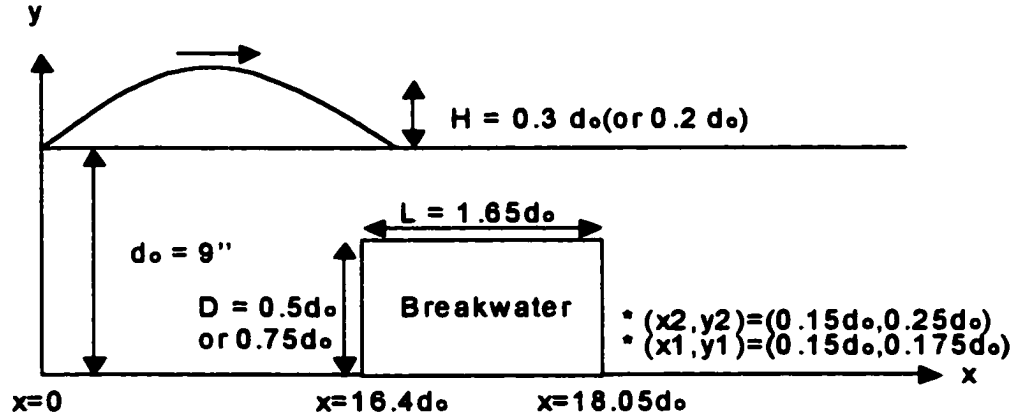


**Fig. 4-1 Solitary wave propagates over breakwater**

The undisturbed water depth,  $d_o$ , is nine inches; the breakwater width,  $L$ , is 14.85 inches, and the breakwater height,  $D$ , is  $4 \frac{1}{2}$  inches. The wave height,  $H$ , of solitary wave is 30% of the water depth. Variables used in the numerical model are all dimensionless normalized by the water depth,  $d_o$ . For the present computation, the water depth,  $d_o/d_o$ , is one; the breakwater width,  $L/d_o$ , is 1.65; the breakwater height,  $D/d_o$ , is one-half; the wave height,  $H/d_o$ , is 0.3; Reynolds number,  $Re$ , is 80,000; the time increment,  $dt(g/d_o)^{0.5}$ , is 0.05; the space increment,  $dx/d_o$ , is 0.05;  $dy/d_o$ , is 0.05; particle space increment,  $dl/d_o$ , is 0.05; the dimensionless time,  $t$ , is defined as  $t(g/d_o)^{0.5}$ ; and the observation points are at  $(x_1/d_o, y_1/d_o) = (0.15, 0.175)$ ,

$(x_2/d_o, y_2/d_o) = (0.15, 0.25)$  measured from the bottom and the breakwater shoreward face.

Fig.4-2 shows the comparisons of particle velocity time history at position  $(x_1/d_o, y_1/d_o) = (0.15, 0.175)$  among the present computer model, the experimental data (Lee et al.1993), and the combined rotational flow model(Zhuang, 1994). The ordinate is the normalized velocity w.r.t. the wave celerity  $(gd_o)^{0.5}$  ( the wave celerity in water depth  $d_o$ ) and the abscissa is normalized time as  $t(g/d_o)^{0.5}$ . The u and v velocity history obtained by the present model and the experiment shows that the time history trend agrees fairly well. It reveals that the horizontal velocity changes the direction from positive to negative and the vertical velocity changes from negative to positive within the time period shown. These kinematic properties show that the flow at the location  $(x_1/d_o, y_1/d_o) = (0.15, 0.175)$  first move forward (shoreward) then downward followed by backward (seaward) and upward motions. There exists a rotational motion occurring at the shoreward side of the breakwater when the solitary wave propagates over the breakwater. The present model predicts this feature of particle movement better than the combined rotational flow model proposed by Zhuang, (1994).

Fig.4-3 shows comparisons of particle velocity time history at another position  $(x_2/d_o, y_2/d_o) = (0.15, 0.25)$  among the present model ,the experiment, and the combined rotational flow model. The present computer model results agree well

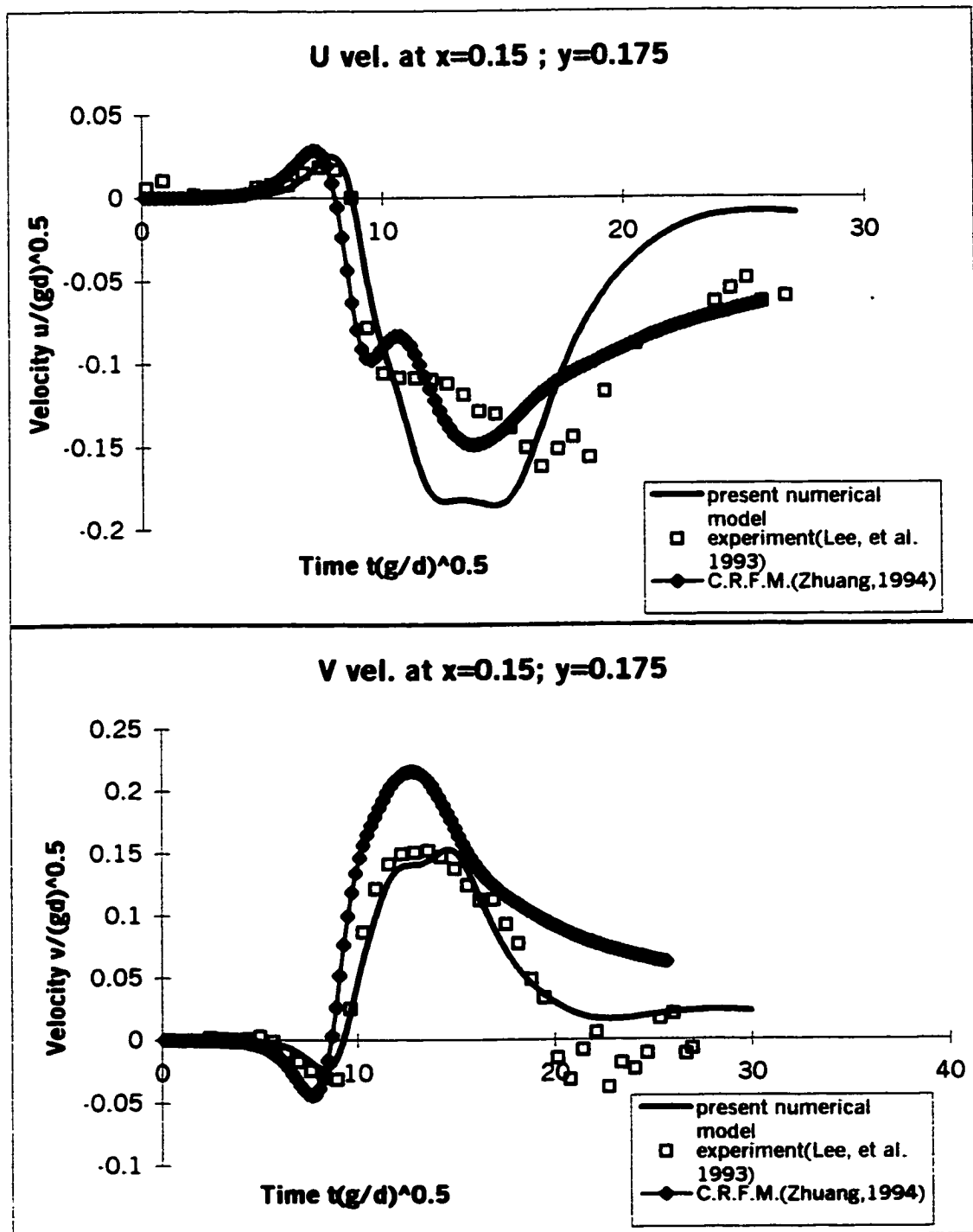


**Fig. 4-2 Comparison of velocities of the present model, experiment (Lee, et al., 1993), and combined rotational flow model (C.R.F.M)(Zhuang, 1994) at  $x=0.15$  and  $y=0.175$ , which are measured from bottom bed and shoreward face of the breakwater. ( $D/d_o=0.5$ ,  $H/d_o=0.3$ ,  $d_o=0.9\text{in}$ )**

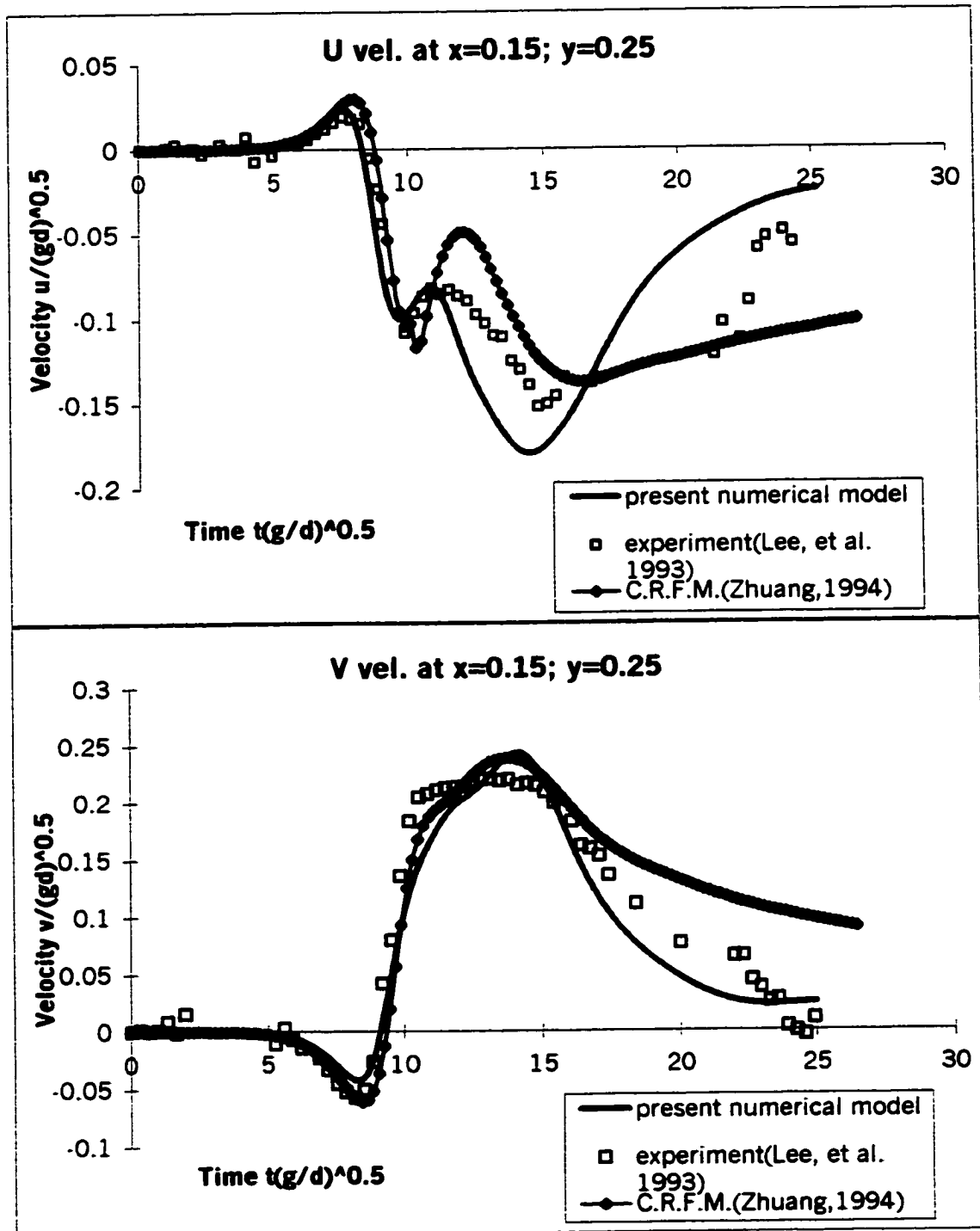
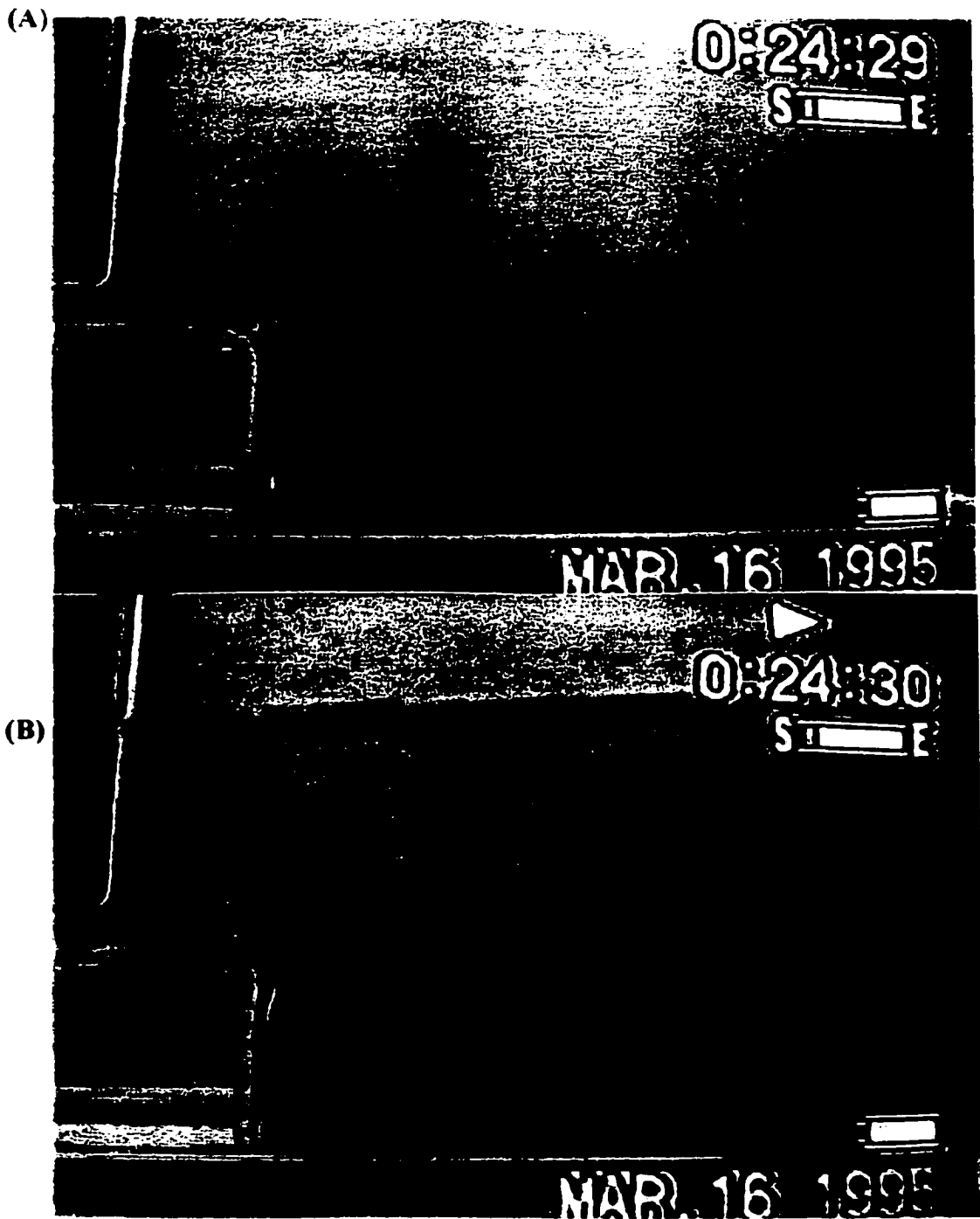


Fig. 4-3 Comparison of velocities of the present model, experiment (Lee, et al., 1993), and combined rotational flow model (C.R.F.M)(Zhuang, 1994) at  $x=0.15$  and  $y=0.25$ , which are measured from bottom bed and shoreward face of the breakwater. ( $D/d_o=0.5$ ,  $H/d_o=0.3$ ,  $d_o=0.9\text{in}$ )

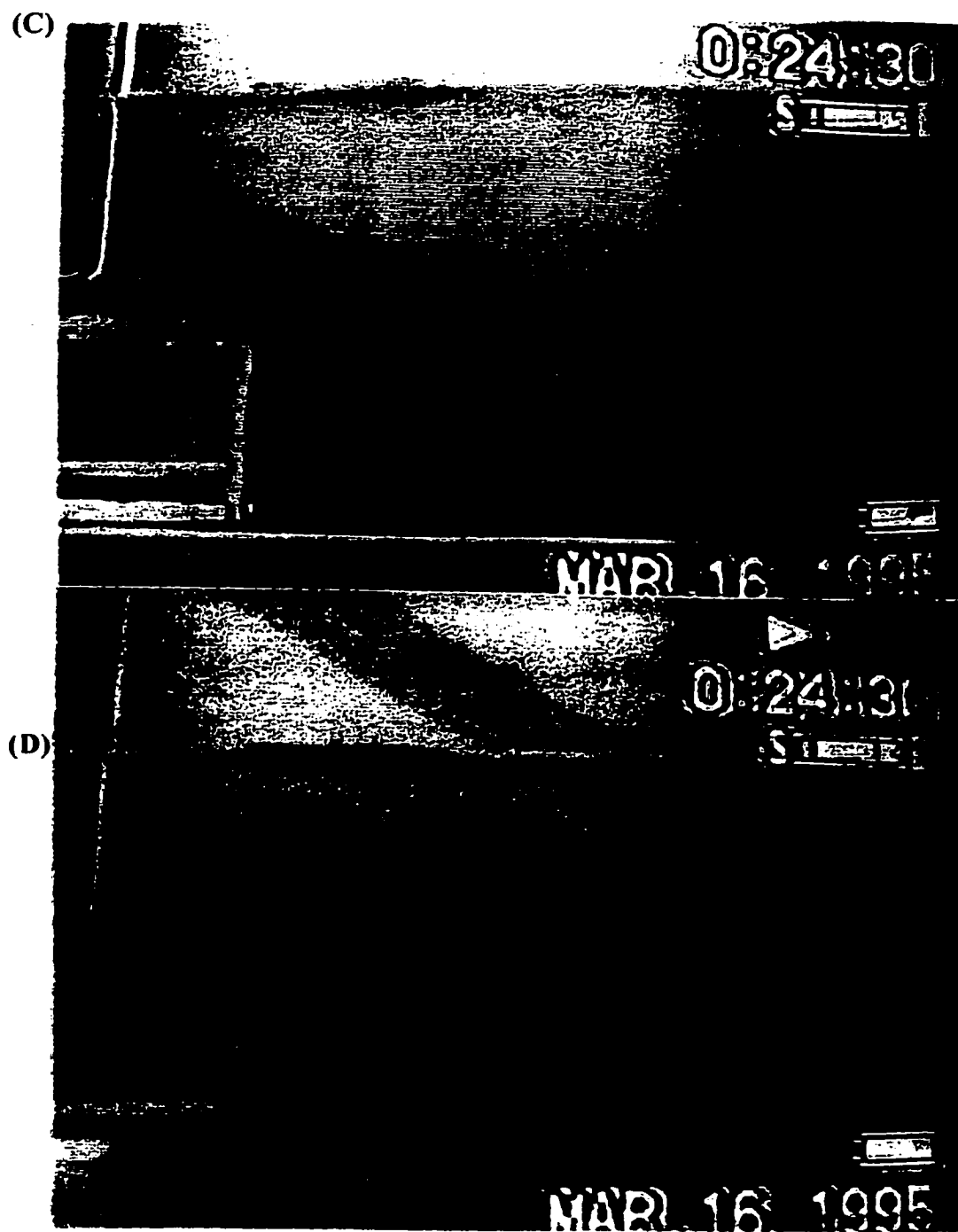
with experimental data and appear to fit the experimental data better than the numerical results predicted by the combined rotational flow model of Zhuang, (1994). Based on these available data for comparison, the present numerical model is shown to be capable of predicting the temporal variations of flow field for the case of solitary wave propagating over a submerged breakwater.

Fig.4-4 and Fig.4-5 present a series of photographs at different time sequence taken during one experimental run of  $H/d_o = 0.3$  solitary wave overtopping on a submerged breakwater (height=4.5 inches and width=14.85 inches) with water depth at  $d_o=9$  inches. The blue dye is injected in the shoreward region of the breakwater before the wave is generated. The solitary wave propagates from left to right direction in the pictures. The breakwater can be seen at the lower left corner of the pictures. It is observed that a strong rotational flow field is generated when the wave propagates over the breakwater in the vicinity of the shoreward region of the breakwater. Since it is a transient process, the vortex will grow bigger and bigger after the wave has passed and moves downstream toward the right and is disintegrated eventually.

Fig.4-6 presents computer model result when the solitary wave crest is about one breakwater length away from the submerged breakwater at time  $T=10.0$  ( $t(g/d_o)^{0.5}=10.0$ ). Fig.4-6(a) shows the variations of the wave surface profile while the solitary wave is passing over the breakwater. Fig.4-6(b) shows the close-up of



**Fig. 4-4 Pictures (A) and (B) of an experimental observation of vortex generation for solitary wave overtopping submerged breakwater.  $D/d_o=0.5$ ,  $H/d_o=0.3$ ,  $d_o=0.9$ in. (Lee, et al., 1993)**



**Fig. 4-5 Pictures (C) and (D) of an experimental observation of vortex generation for solitary wave overtopping submerged breakwater.  $D/d_o=0.5$ ,  $H/d_o=0.3$ ,  $d_o=0.9$ in. (Lee, et al., 1993)**

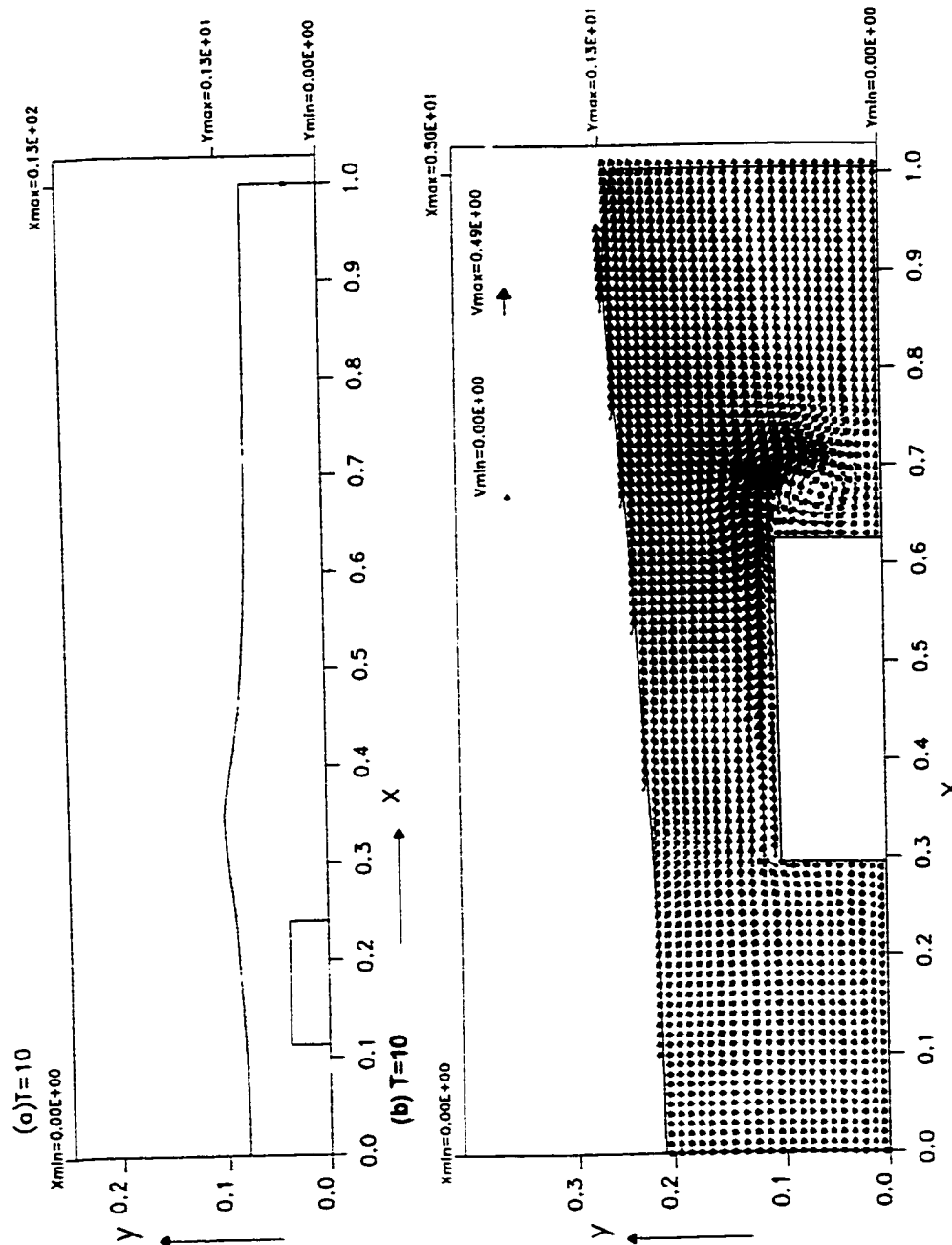


Fig. 4-6 Velocity field at non-dimensional time  $T=10.0$  ( $t\sqrt{g/d_o}=10.0$ ) by the present model. The ordinate is  $y/d_o$  and the abscissa is  $x/d_o$ .  $D/d_o=0.5$ ,  $H/d_o=0.3$ ,  $d_o=0.9$ in. (a) the variation of water surface while the solitary wave passing over the breakwater (b) close-up of velocity field in the vicinity of the breakwater



the velocity field in the vicinity of the breakwater. From Fig.4-6 it is seen that flow separates from both upper edges of the submerged breakwater. This behavior is caused by the large curvature of the sharp edges because it would take an infinite pressure gradient across the streamlines to cause the fluid to turn a sharp corner. This is physically impossible therefore the fluid must separate at the sharp corner.

Fig.4-6 shows that the complete vortex is shed from the shoreward edge of the submerged obstacle. However, at this time ( $T=10$ ) the separation region is still small compared to the submerged obstacle. It can be seen that the flow separation modifies the fluid kinematics around the shoreward edge of the submerged obstacle, but it has no effect on the overall flow pattern in the near field.

Fig.4-7 shows that the solitary wave crest is about two breakwater length away from the submerged breakwater at time  $T=12.0$  ( $t(g/d_o)^{0.5}=12.0$ ). Fig.4-7(a) shows the variations of the wave surface profile while the solitary wave is passing over the breakwater. Fig.4-7(b) is the close-up of the velocity field in the vicinity of the breakwater. The strong clockwise rotational motion is generated in the vicinity of the shoreward region of the breakwater. The clockwise vortex appears to be strong in its right and bottom region. Thus the rotational flow will impact the bottom bed and could scour the foundation of shoreward side of the breakwater. This rotational flow could affect the stability of the breakwater. Fig.4-8 shows that the rotational flow continues to grow at time  $T=14.0$  ( $t(g/d_o)^{0.5}=14.0$ ). The intense clockwise

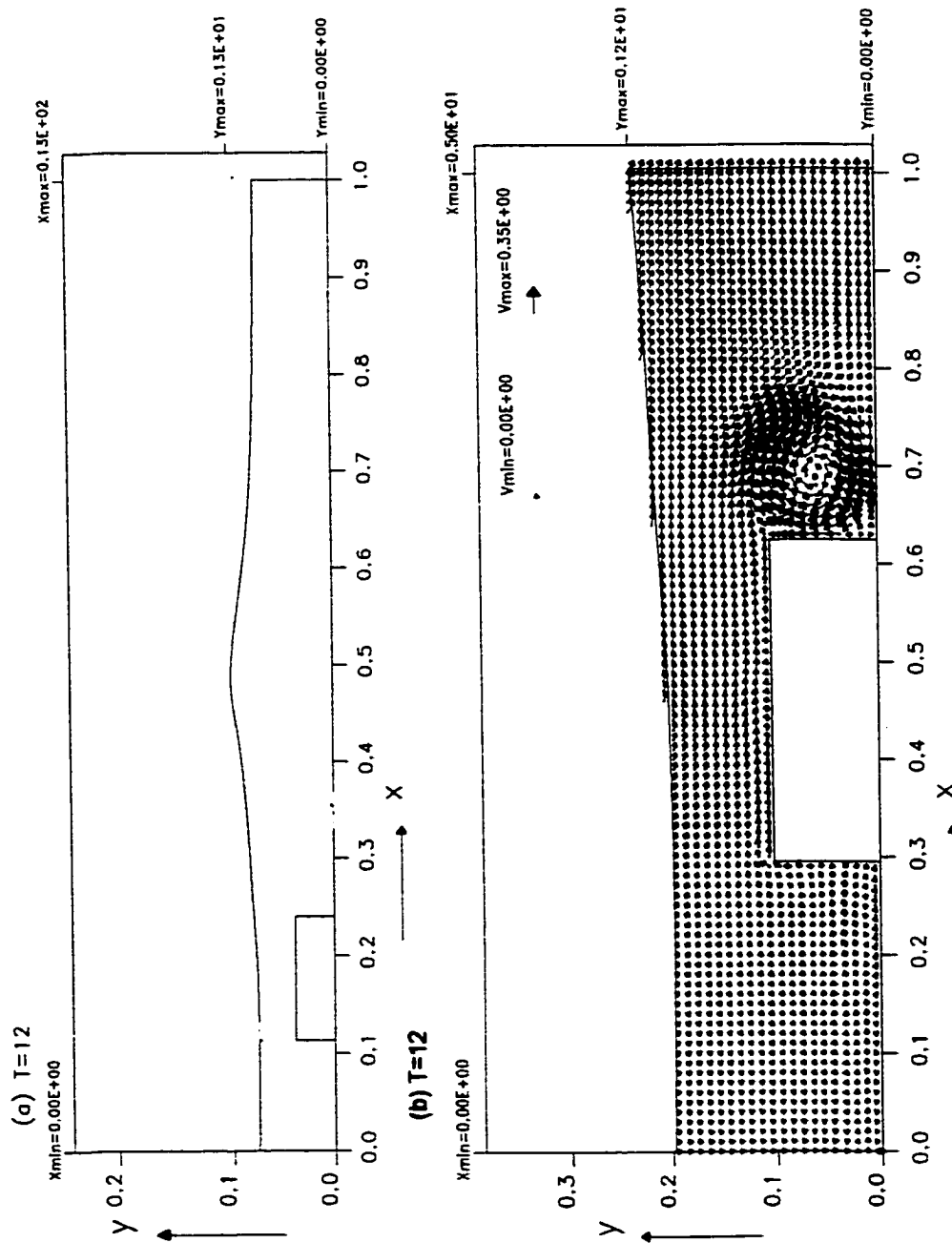


Fig. 4-7 Velocity field at non-dimensional time  $T=12.0$  ( $\sqrt{g/d_0} = 12.0$ ) by the present model. The ordinate is  $y/d_0$  and the abscissa is  $x/d_0$ .  $D/d_0=0.5$ ,  $H/d_0=0.3$ ,  $d_0=0.9$ in. (a) the variation of water surface while the solitary wave passing over the breakwater (b) close-up of velocity field in the vicinity of the breakwater

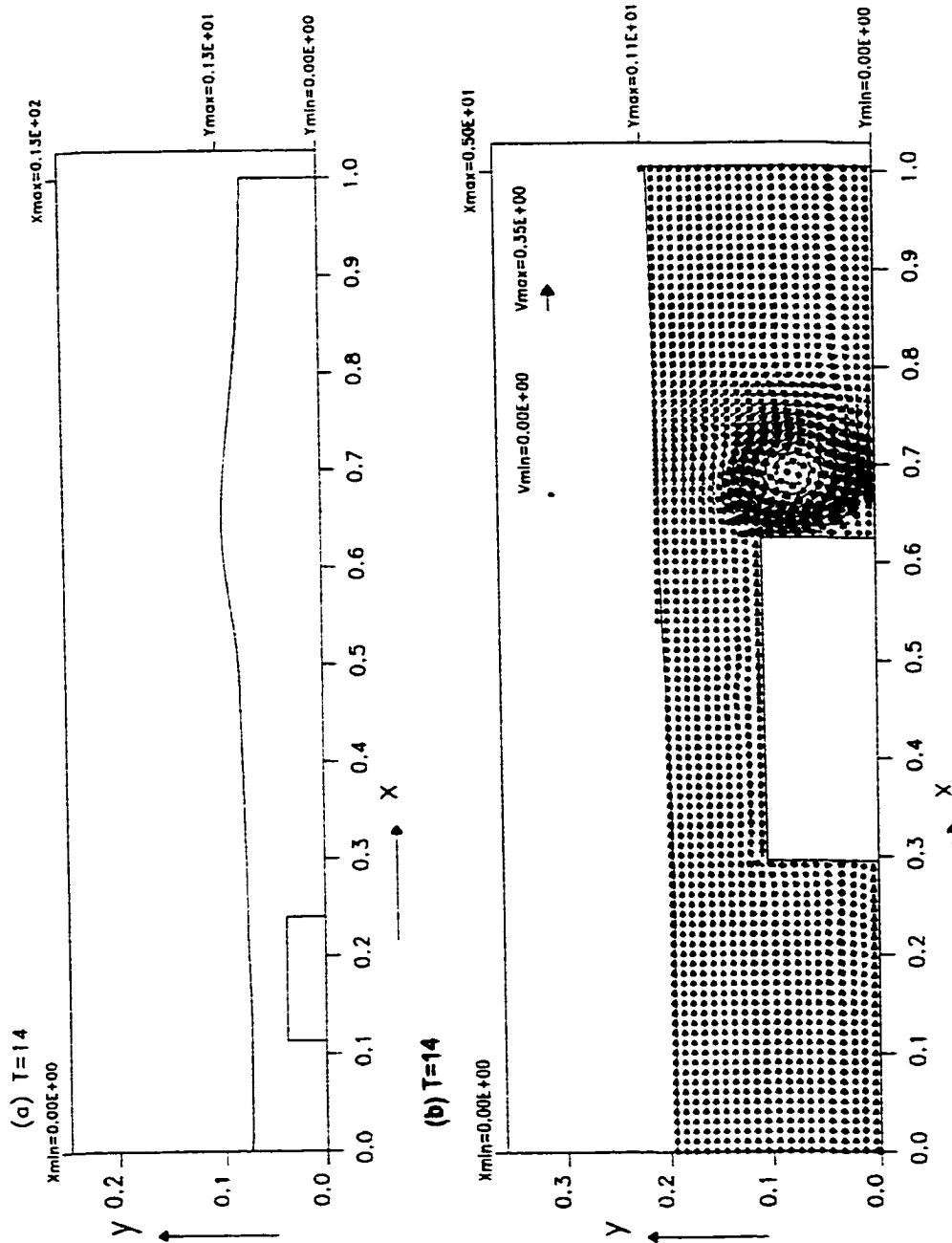


Fig. 4-8 Velocity field at non-dimensional time  $T=14.0$  ( $\sqrt{g/d_0} = 14.0$ ) by the present model. The ordinate is  $y/d_0$  and the abscissa is  $x/d_0$ .  $D/d_0=0.5$ ,  $H/d_0=0.3$ ,  $d_0=0.9$ in. (a) the variation of water surface while the solitary wave passing over the breakwater (b) close-up of velocity field in the vicinity of the breakwater

vortex appears in the bottom portion and on the breakwater shoreward face. The rotational flow still scours the bottom bed and impacts shoreward face of the breakwater. And the clockwise vortex moves upward. The phenomena agree well with experiments of Lee et al. (1993) as well as the results of Ting et al. (1994). The oscillatory wave trains are gradually formed behind the solitary wave.

Fig.4-9 shows the further growth of the clockwise rotational motion at time  $T=16.0$  ( $t(g/d_o)^{0.5}=16.0$ ), when the solitary wave peak is further away from the breakwater. The rotational flow moves upward at this time, it is found to be away from the foundation of the breakwater. Therefore, the foundation of the breakwater is no longer scoured at this time interval. But the force impacts the upper section of the breakwater shoreward face. Fig.4-10 shows the upward movement of the clockwise vortex affecting the water surface at time  $T=18.0$  ( $t(g/d_o)^{0.5}=18.0$ ). The oscillatory wave trains are found to be behind the solitary wave. Since the solitary wave has been away from the submerged breakwater, there is no more energy to support the clockwise vortex. The clockwise vortex continues to grow but it is weaken. Fig.4-11 shows that the clockwise vortex significantly affects the water surface elevation as it moves away from the breakwater at time  $T=20.0$  ( $t(g/d_o)^{0.5}=20.0$ ). The vortex existed at location sufficiently away from the bottom. Thus, it is no longer impacting the foundation of breakwater. But the shoreward corner of the breakwater may experience erosion due to the clockwise vortex. The

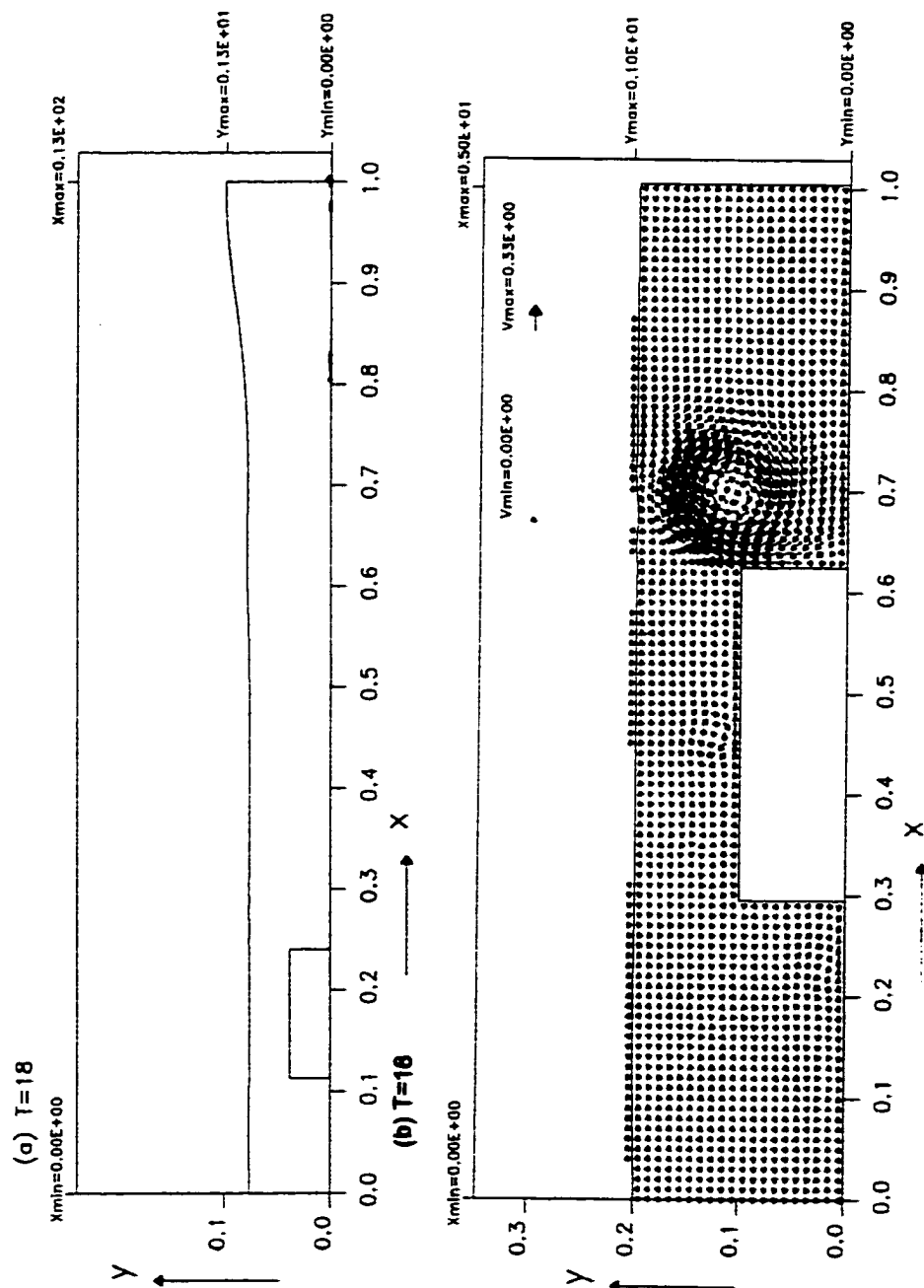


Fig. 4-10 Velocity field at non-dimensional time  $T=18.0$  ( $\sqrt{g/d_0} = 18.0$ ) by the present model. The ordinate is  $y/d_0$  and the abscissa is  $x/d_0$ .  $D/d_0=0.5$ ,  $H/d_0=0.3$ ,  $d_0=0.9$ m. (a) the variation of water surface while the solitary wave passing over the breakwater (b) close-up of velocity field in the vicinity of the breakwater

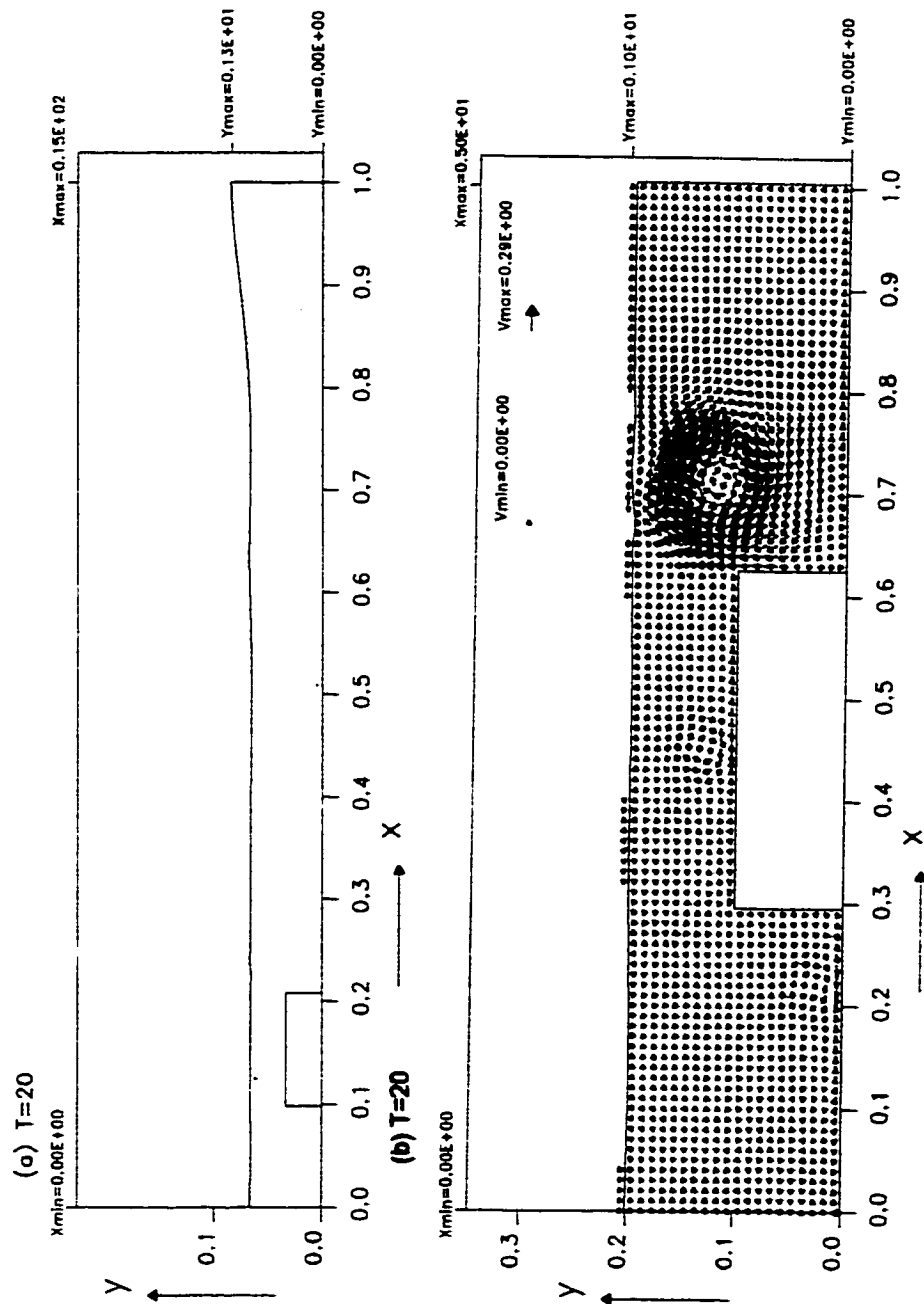


Fig. 4-11 Velocity field at non-dimensional time  $T=20.0$  ( $t\sqrt{g/d_o} = 20.0$ ) by the present model. The ordinate is  $y/d_o$  and the abscissa is  $x/d_o$ .  $D/d_o=0.5$ ,  $H/d_o=0.3$ ,  $d_o=0.9$ in. (a) the variation of water surface while the solitary wave passing over the breakwater (b) close-up of velocity field in the vicinity of the breakwater

vortex intensity becomes weaker since the crest of the solitary wave moves further away from the breakwater. The transmitted wave height ( $=0.28653$ ) indicates a 4.5% reduction in incident wave height because the wave loses the energy due to the viscous vortex when the solitary wave passes over the submerged breakwater.

Fig.4-12 shows that the reversal wave propagates over the submerged breakwater from right to left direction at time  $T=50.0$  ( $t(g/d_0)^{0.5}=50.0$ ). As it can be seen from the figure, the clockwise vortex in the shoreward region disappears. There are two counterclockwise vortices generated at the seaward region and at the top of submerged breakwater. The two counterclockwise vortices are weak since the reversal solitary wave is further away from the breakwater. The processes of the rotational flow growing in the seaward region of the breakwater are similarly to ones from Fig.4-6 to Fig.4-11. The transmitted wave height ( $=0.261$ ) indicates a 13% reduction in incident wave height. This result indicates that the breakwater reduces the wave energy.

The critical failure areas in structures of caisson are the toe and underlying foundation due to the wave-induced scouring, liquefaction and large stresses in the foundation soil. (Tsai, et al. 1986) The results based on the Fig.4-6 to Fig.4-12 show that if the incident wave propagates over the submerged breakwater from the seaward region to the shoreward region, the shoreward side of the breakwater is significantly impacted, and the scouring and erosions could occur. Liu, et al.(1999)

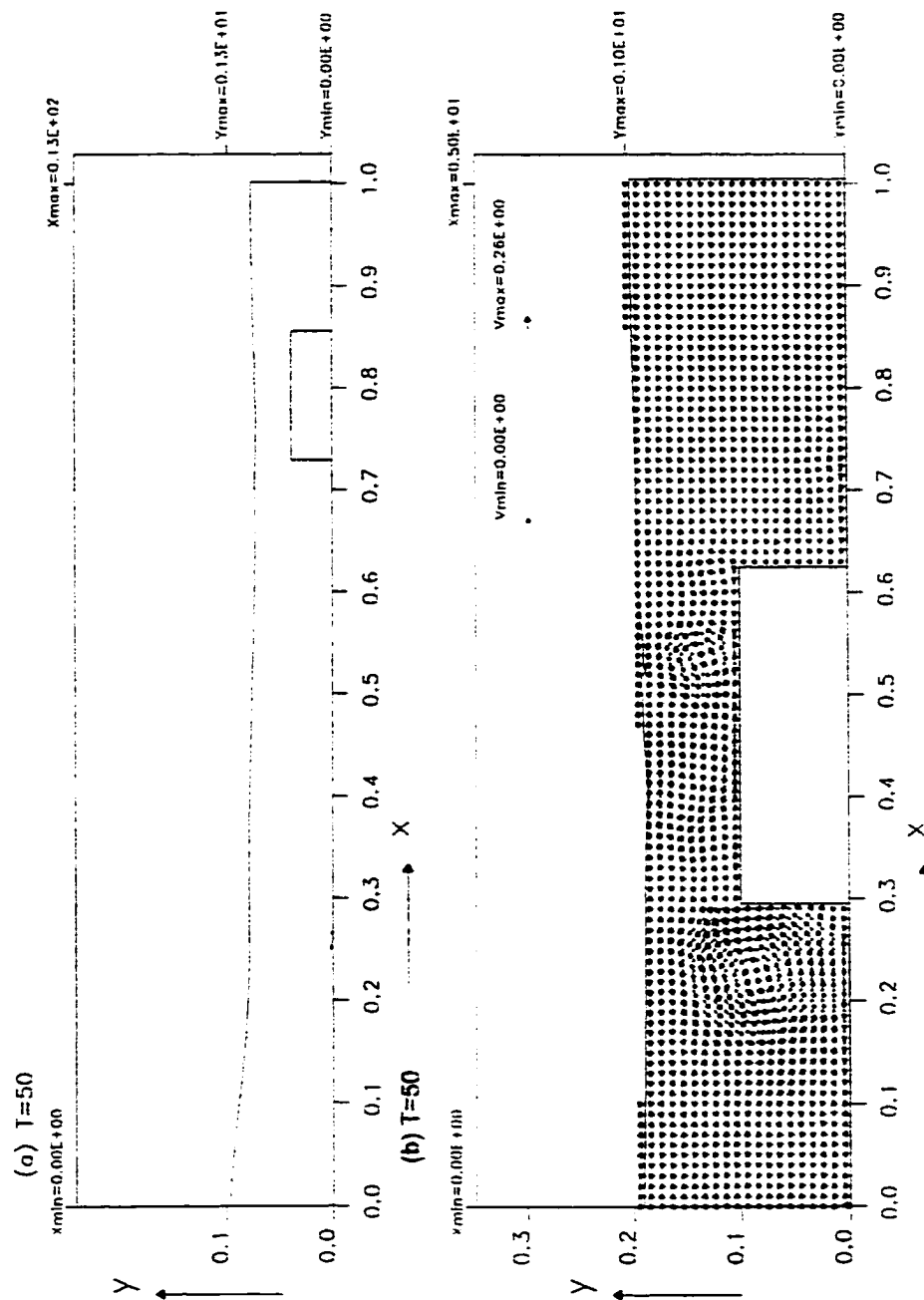
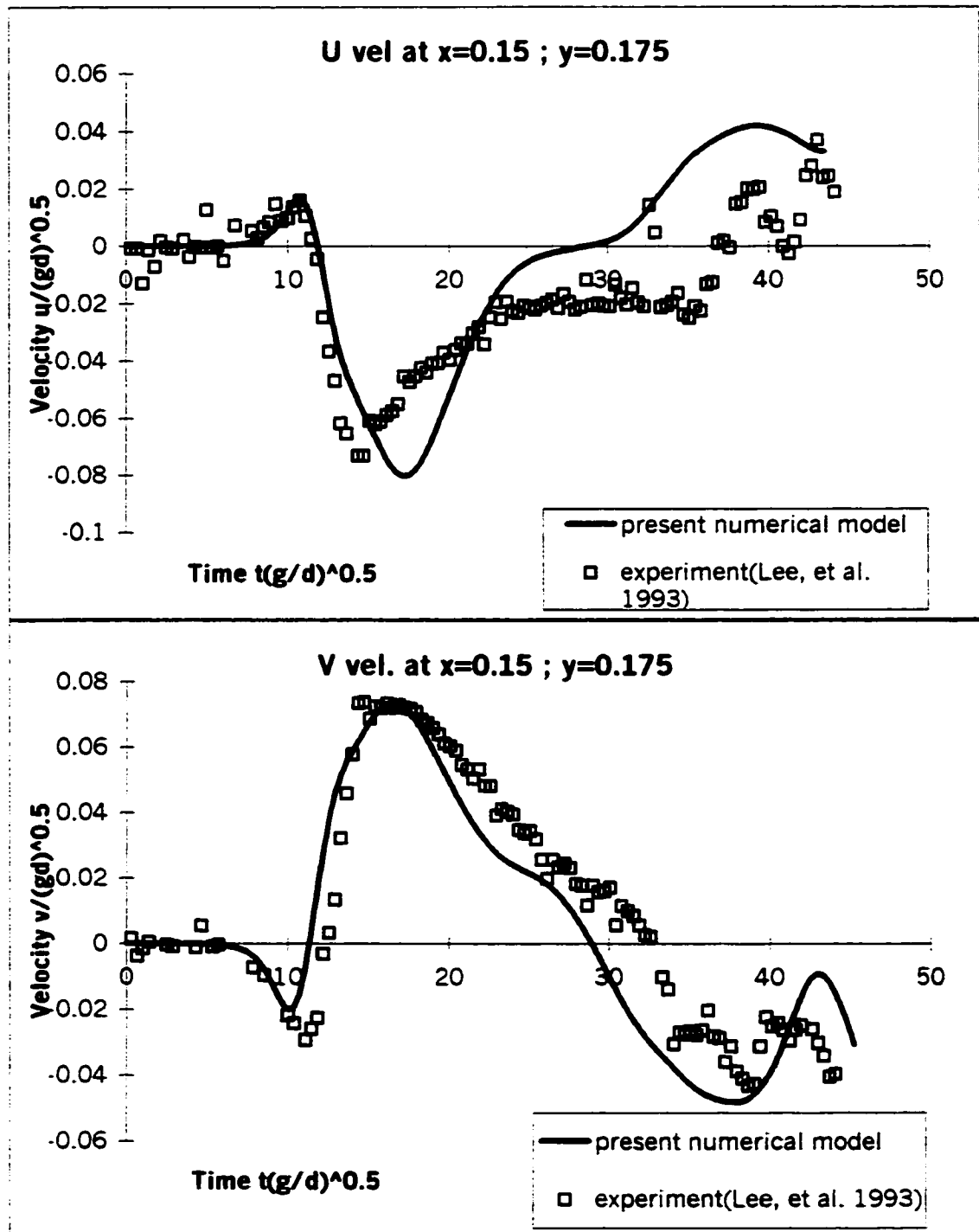


Fig. 4-12 Velocity field at non-dimensional time  $T=50.0$  ( $\sqrt{g/d_0} = 50.0$ ) by the present model. The ordinate is  $y/d_0$  and the abscissa is  $x/d_0$ .  $D/d_0=0.5$ ,  $H/d_0=0.3$ ,  $d_0=0.9$ in. (a) the variation of water surface while the solitary wave passing over the breakwater (b) close-up of velocity field in the vicinity of the breakwater



shows that the porous armor layer is effective in reducing the overtopping rate as well as in preventing the caisson breakwater from the bottom scouring effect. If the transmitted wave reflects from the right-hand vertical boundary, the seaward side of the breakwater will suffer the same problems and the breakwater can deteriorate quickly. In addition, the rotational flow occurring around the breakwater will consume some energy from the overtopping wave thus reducing the amplitude the transmitted wave.

Comparisons of  $u$  and  $v$  velocity time history between the present numerical model and the experiment at the location  $(x_1/d_o, y_1/d_o) = (0.15, 0.175)$  for another breakwater configuration are shown in Fig.4-13. Zhuang (1994) did not provide the computational result in this case for comparison. For this configuration, the breakwater height  $D/d_o$  is increased to 0.75, wave height  $H/d_o$  is 0.2, and the time increment  $dt(g/d_o)^{0.5}$  is 0.08, other variables are the same as that shown in Fig.4-2. The definitions of these variables are previously shown in Fig.4-1. The present model results agree well with the experimental data and there exists a phenomenon that rotational motion occurs at the shoreward side of the breakwater when the solitary wave transmits over the breakwater. The magnitude of the velocities shown in Fig.4-13 is smaller than that shown in Fig.4-2. However, the trend predicted by the present computer model fit well with the experimental data even though the magnitude is small which is the result of the increased breakwater height.



**Fig. 4-13 Comparison of velocities of the present model and experiment (Lee, et al., 1993), at  $x=0.15$  and  $y=0.175$ , which are measured from bottom bed and shoreward face of the breakwater. ( $D/d_o=0.75$ ,  $H/d_o=0.2$ ,  $d_o=0.9\text{m}$ )**

Fig.4-14 shows the velocity distribution at time dimensionless  $T=10.0$  ( $t(g/d_0)^{0.5}=10.0$ ), as the incident solitary wave propagates over the breakwater. The clockwise vortex is shed from the shoreward face of breakwater. Fig.4-15 shows that the clockwise vortex continues to grow but it doesn't reach the bottom bed at time  $T=12.0$  ( $t(g/d_0)^{0.5}=12.0$ ), since the height of breakwater is large. In Fig.4-16, it can be seen that the clockwise vortex expands outward and hardly impacts the bottom bed at time  $T=14.0$  ( $t(g/d_0)^{0.5}=14.0$ ). Since the water depth is above the top of the breakwater is shallow, thus the horizontal velocities is quite large, creating a large clockwise vortex as the incident wave moves away from the top of breakwater. At this time, the rotational flow is seen to affect the region near the water surface.

The figures from Fig.4-17 to Fig.4-19 show the clockwise vortex gradually moves away from the breakwater and its intensity is gradually weaken. The upward movement significantly affects the water surface from time  $T=16.0$  ( $t(g/d_0)^{0.5}=16.0$ ) to  $T=20.0$ . The rotational flow hardly reaches the bottom bed. As discussed earlier in Fig.4-13, the velocities are small at the separation zone at the location  $(x_1/d_0, y_1/d_0)=(0.15, 0.175)$ . This presents that the rotational flow doesn't scour strongly around the foundation of breakwater in this case. Fig.4-20 shows that the wave reflected from the right boundary propagates over the submerged breakwater from the right to the left direction at time  $T=50.0$  ( $t(g/d_0)^{0.5}=50.0$ ).

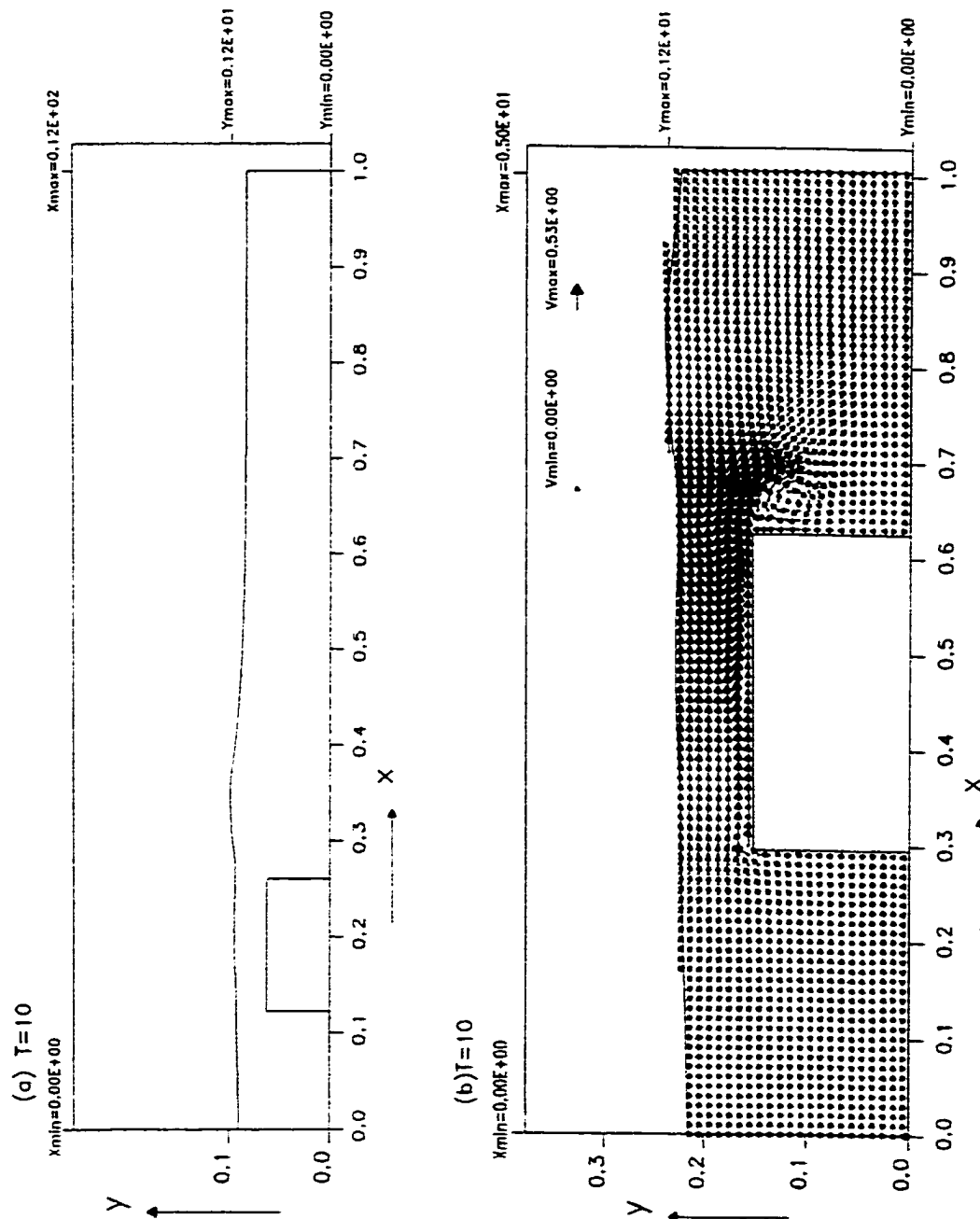


**Fig. 4-14 Velocity field at non-dimensional time  $T=10.0$  ( $\sqrt{g/d_n}=10.0$ ) by the present model. The ordinate is  $y/d_0$  and the abscissa is  $x/d_0$ .  $D/d_0=0.75$ ,  $H/d_0=0.2$ ,  $d_0=0.9$ m. (a) the variation of water surface while the solitary wave passing over the breakwater (b) close-up of velocity field in the vicinity of the breakwater**

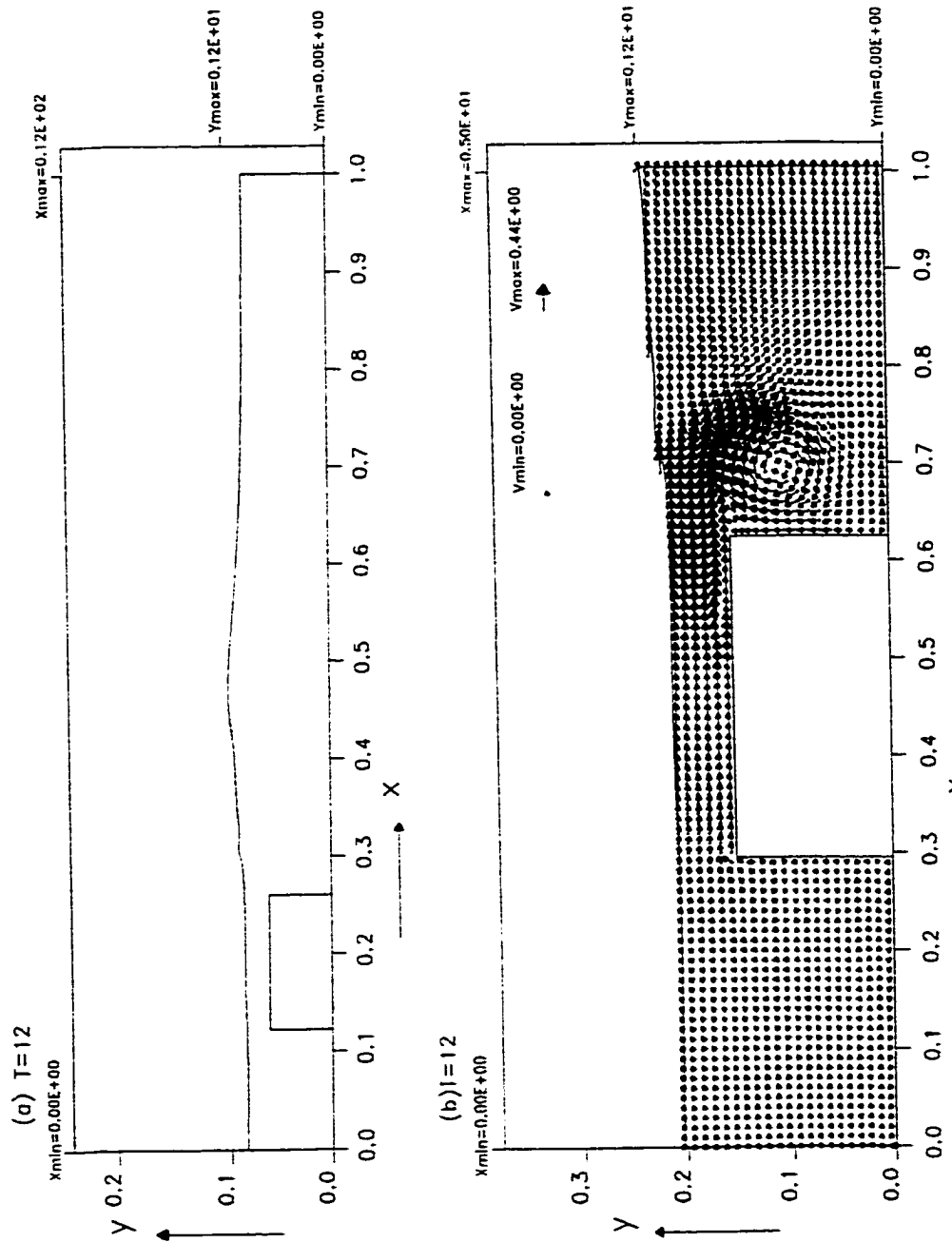


Fig. 4-15 Velocity field at non-dimensional time  $T=12.0$  ( $t\sqrt{g/d_0} = 12.0$ ) by the present model. The ordinate is  $y/d_0$  and the abscissa is  $x/d_0$ .  $D/d_0=0.75$ ,  $H/d_0=0.2$ ,  $d_0=0.9$ in. (a) the variation of water surface while the solitary wave passing over the breakwater (b) close-up of velocity field in the vicinity of the breakwater

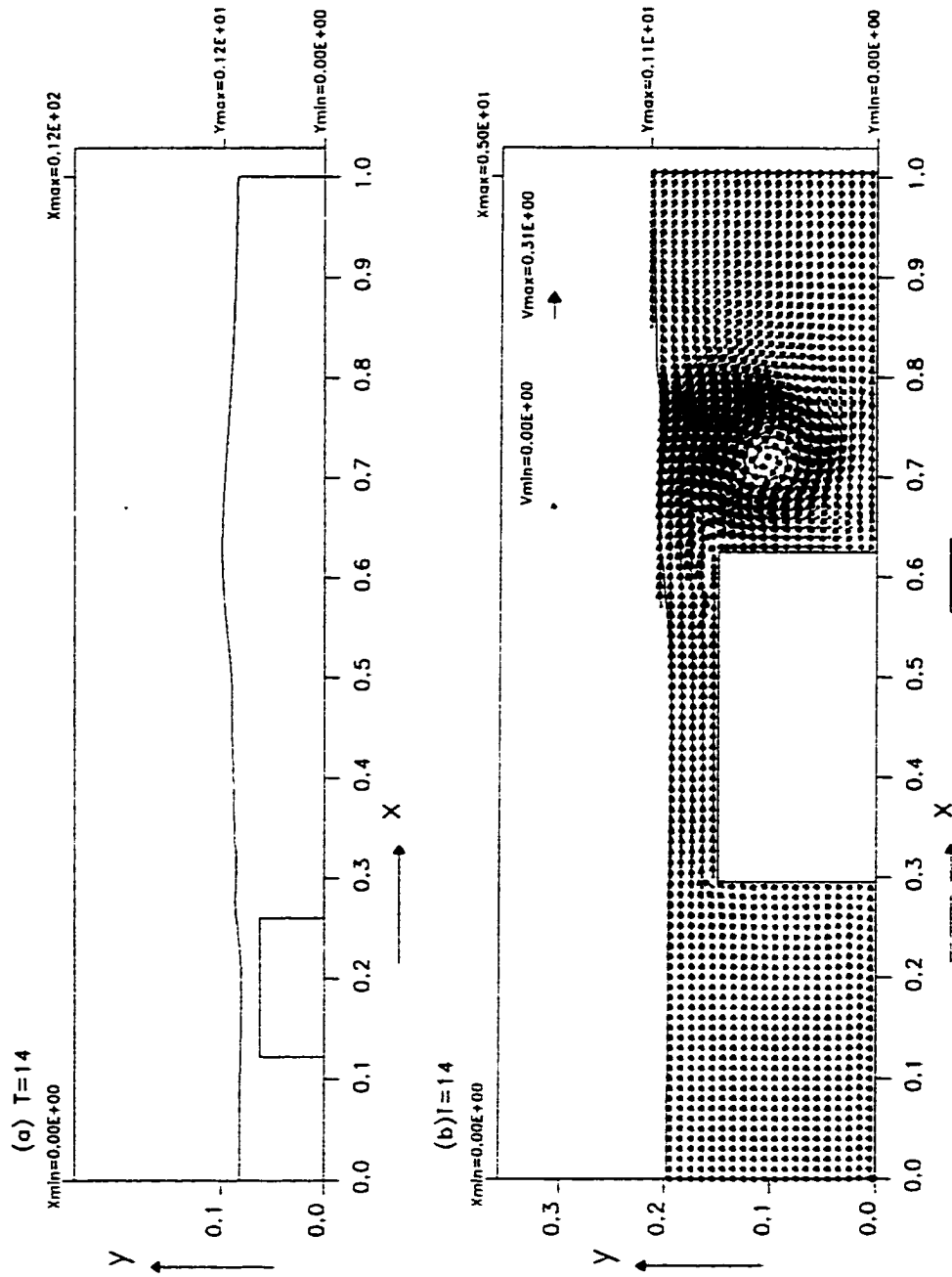


Fig. 4-16 Velocity field at non-dimensional time  $T=14.0$  ( $\sqrt{g/d_o} = 14.0$ ) by the present model. The ordinate is  $y/d_o$  and the abscissa is  $x/d_o$ .  $D/d_o=0.75$ ,  $H/d_o=0.2$ ,  $d_o=0.9$ in. (a) the variation of water surface while the solitary wave passing over the breakwater (b) close-up of velocity field in the vicinity of the breakwater

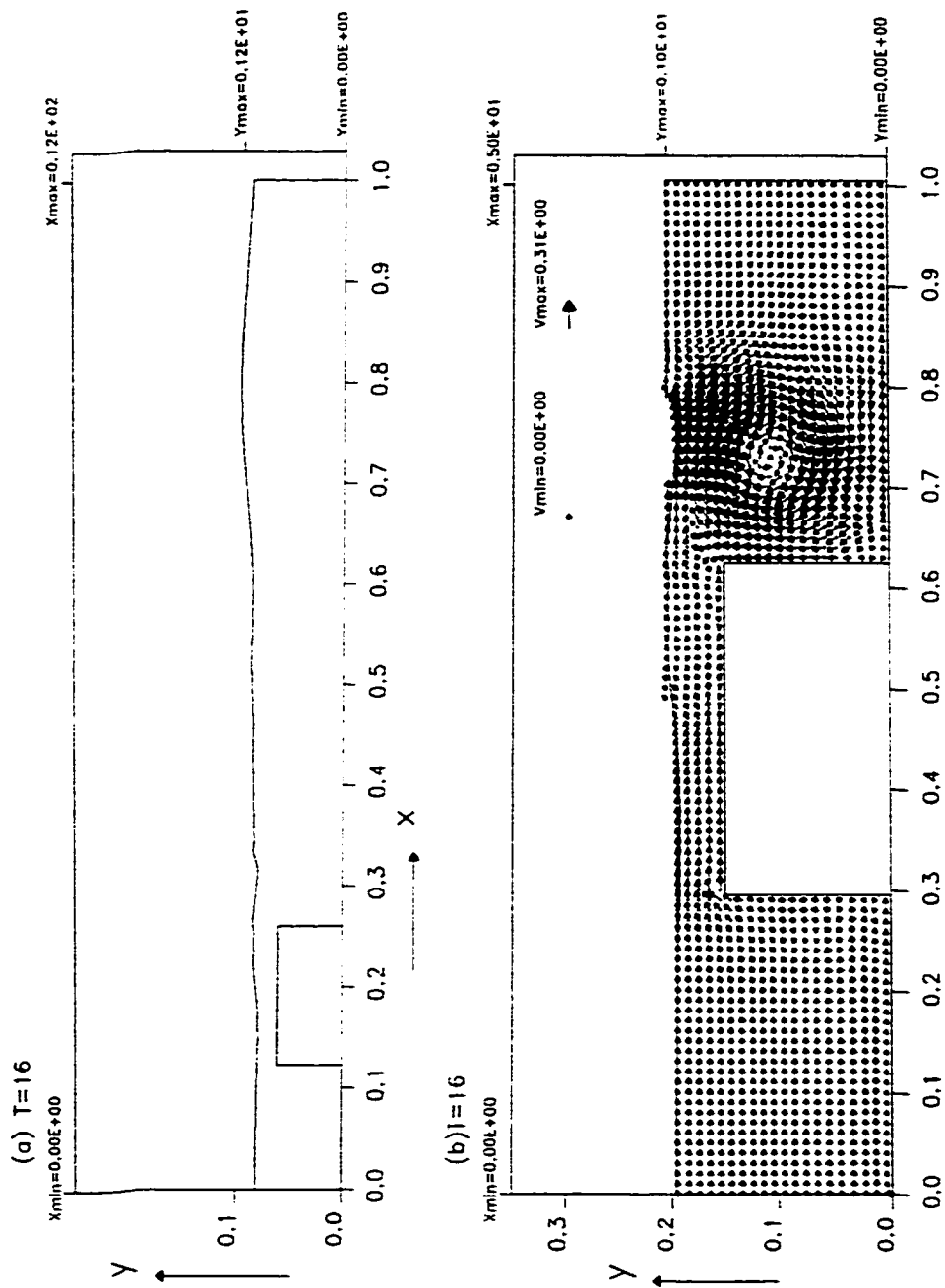


Fig. 4-17 Velocity field at non-dimensional time  $T=16.0$  ( $\sqrt{g/d_n} = 16.0$ ) by the present model. The ordinate is  $y/d_0$  and the abscissa is  $x/d_0$ .  $D/d_0=0.75$ ,  $H/d_0=0.2$ ,  $d_0=0.9$ in. (a) the variation of water surface while the solitary wave passing over the breakwater (b) close-up of velocity field in the vicinity of the breakwater

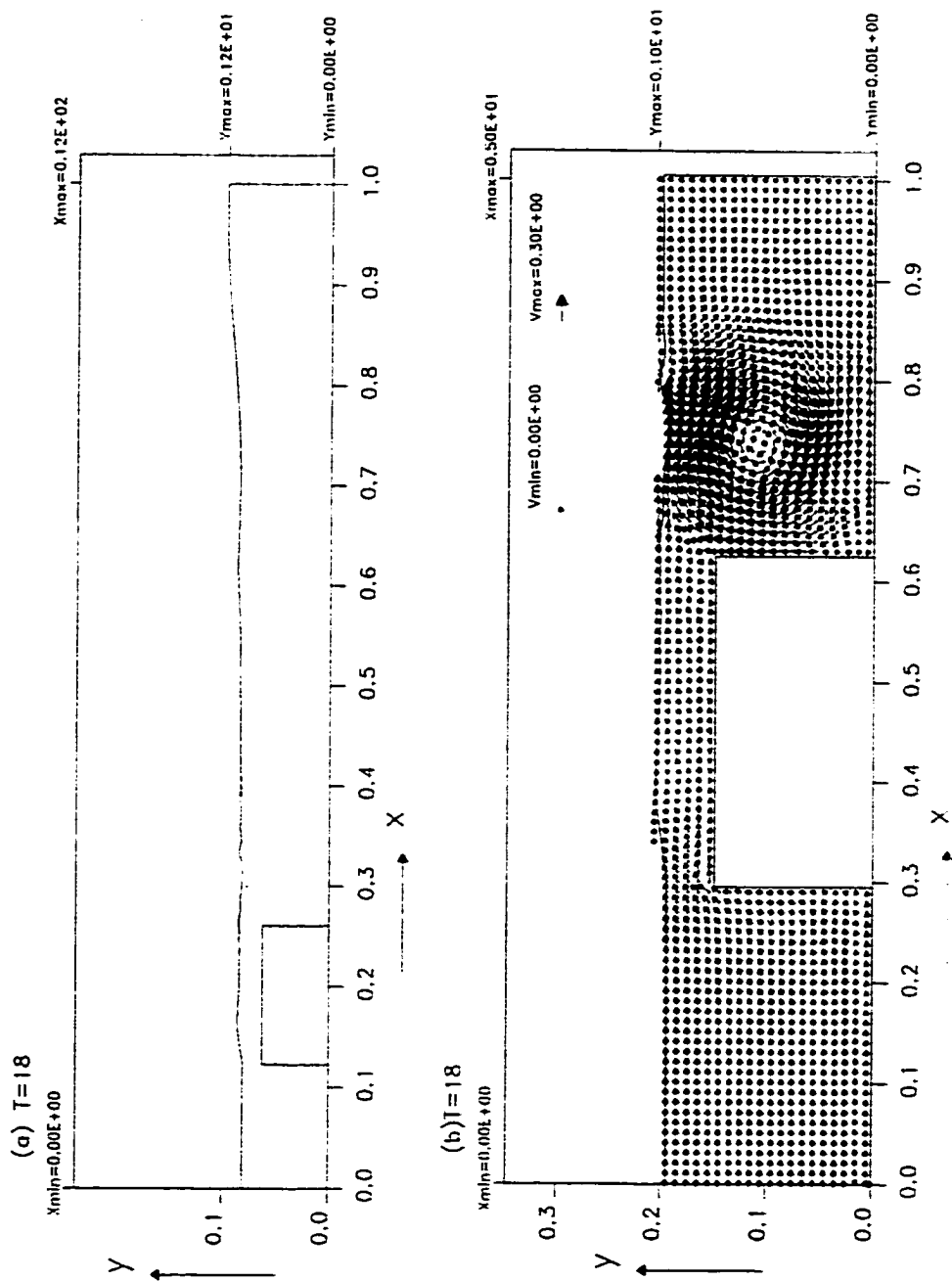


Fig. 4-18 Velocity field at non-dimensional time  $T=18.0$  ( $\sqrt{g/d_o} = 18.0$ ) by the present model. The ordinate is  $y/d_o$  and the abscissa is  $x/d_o$ .  $D/d_o=0.75$ ,  $H/d_o=0.2$ ,  $d_o=0.9$ in. (a) the variation of water surface while the solitary wave passing over the breakwater (b) close-up of velocity field in the vicinity of the breakwater



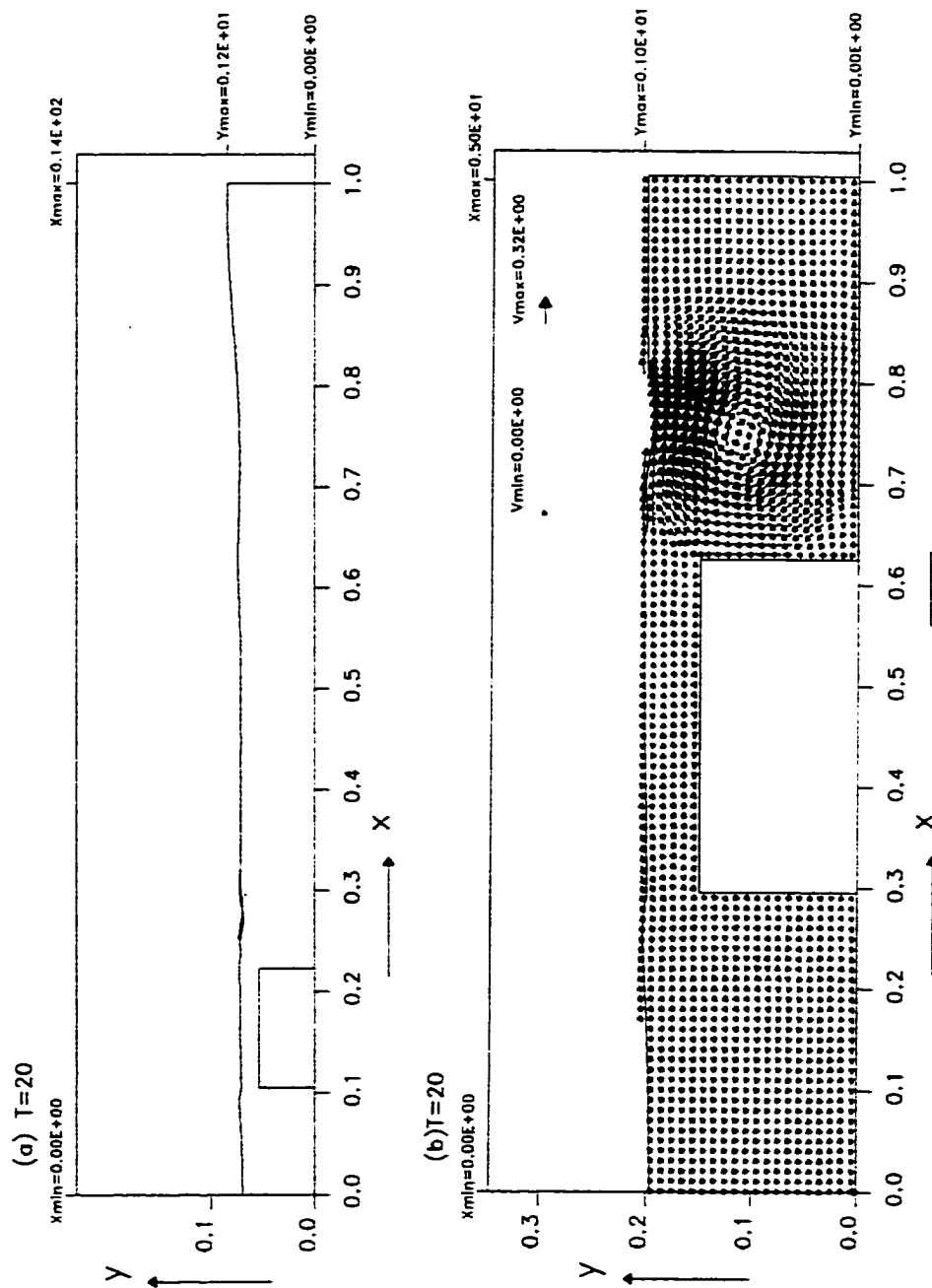


Fig. 4-19 Velocity field at non-dimensional time  $T=20.0$  ( $\sqrt{g/d_0} = 20.0$ ) by the present model. The ordinate is  $y/d_0$  and the abscissa is  $x/d_0$ .  $D/d_0=0.75$ ,  $H/d_0=0.2$ ,  $d_0=0.9$ in. (a) the variation of water surface while the solitary wave passing over the breakwater (b) close-up of velocity field in the vicinity of the breakwater

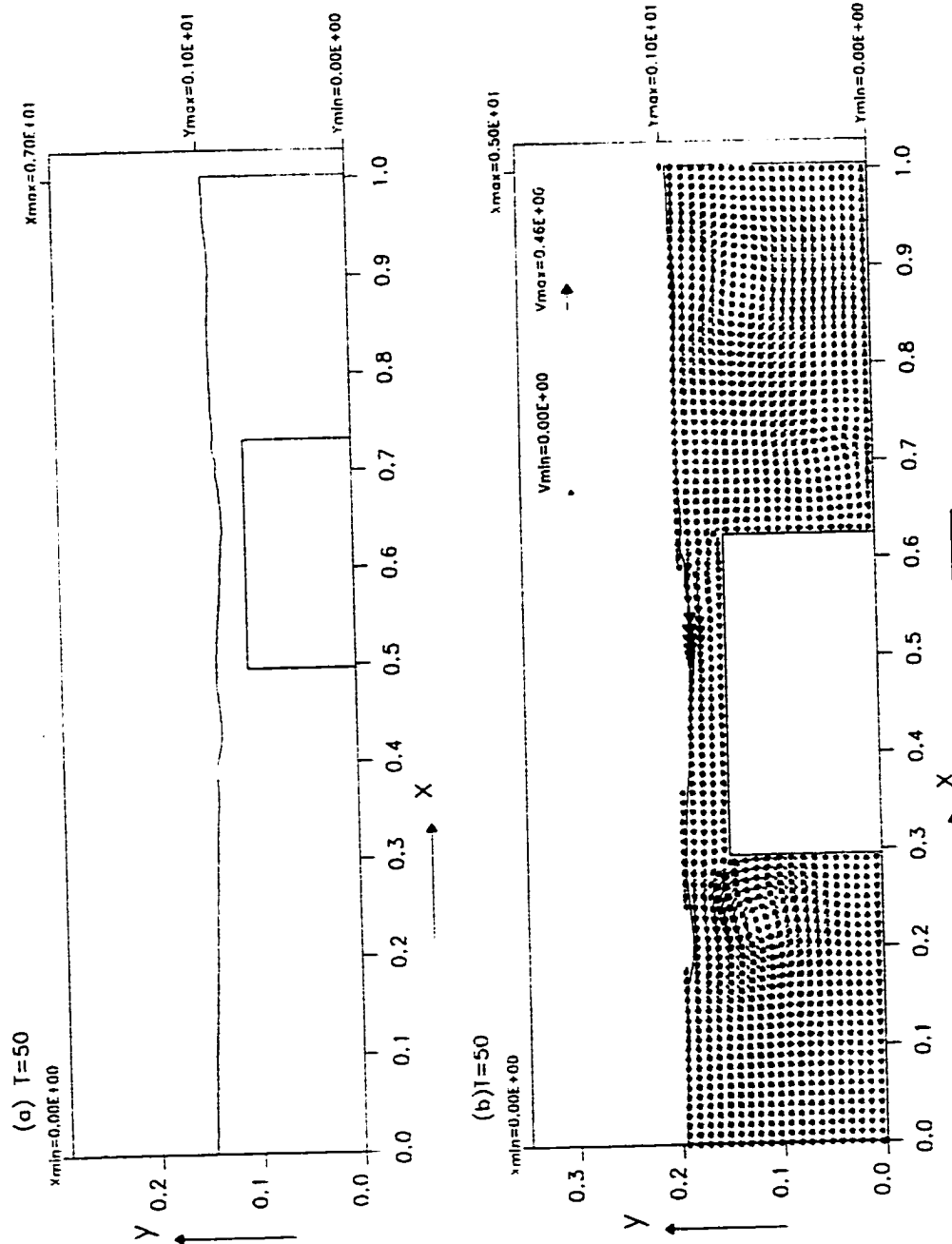


Fig. 4-20 Velocity field at non-dimensional time  $T=50.0$  ( $\sqrt{g/d_0} = 50.0$ ) by the present model. The ordinate is  $y/d_0$  and the abscissa is  $x/d_0$ .  $D/d_0=0.75$ ,  $H/d_0=0.2$ ,  $d_0=0.9$  in. (a) the variation of water surface while the solitary wave passing over the breakwater (b) close-up of velocity field in the vicinity of the breakwater

The clockwise vortex and counterclockwise vortex in the shoreward region appear to be very weak. As the reflected wave propagates over the breakwater it is seen that a counterclockwise vortex is generated in the seaward region. The water depth at top of the submerged breakwater is shallow, thus incapable of generating a vortex in this region. However, the horizontal component of the particle velocity is large in this region. The counterclockwise vortex in the seaward region is fairly weak as the reflected solitary wave moves further away from the breakwater. The processes of the counterclockwise rotational flow growing in the seaward region of breakwater are similarly to those shown from Fig.4-14 to Fig.4-19. The transmitted wave height ( $=0.1520$ ) indicates a 24% reduction in wave height. This result indicates that the breakwater takes away a significant portion of the wave energy.

If the breakwater height  $D/d_0$  is maintained at 0.75, and the wave height  $H/d_0$  is increased to 0.3, the velocity distribution in the vicinity of breakwater at time  $T=14.0$  ( $=t(g/d_0)^{0.5}=14.0$ ) and  $T=16.0$  are shown in Fig.4-21. By comparing Fig.4-16 with Fig.4-21 it is seen that the rotational flow becomes very strong and could scour the bottom bed when the wave height,  $H/d_0$ , is increased from 0.2 to 0.3. This result strongly suggests that the danger of the transmitted waves is increased, when the submergence of the breakwater is shallow and the incident wave amplitude is large.

## 4.2 Run-up of Solitary Wave on Vertical Wall

To examine the normalized maximum run-up height  $R/d_0$  of a solitary wave on a vertical wall, the propagation of a solitary wave in a rectangular channel and the run-up on the vertical wall has been calculated. The computational domain is defined in Fig. 4-22.

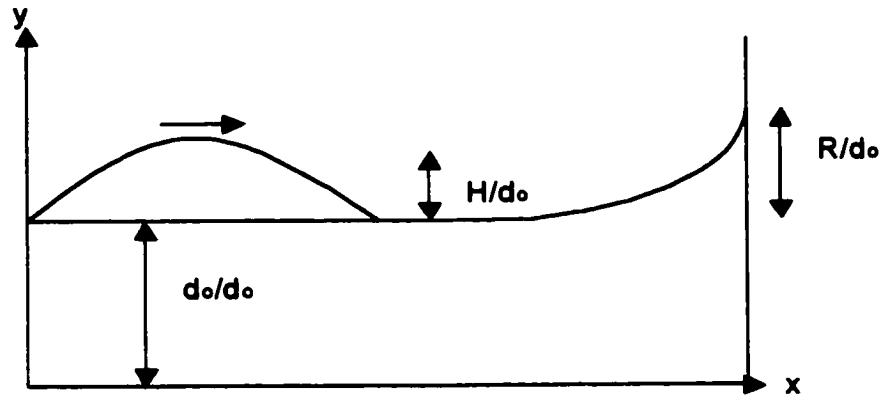


Figure 4-22: Solitary wave propagates and runs up a vertical beach

Application of the present numerical model to solve the Navier-Stokes equation in a Eulerian description has been made for wave run-up on vertical walls. An analytical approximation for the normalized maximum run-up ( $R/d_0$ ) has been suggested by Laitone's approximation (1960).

$$\frac{R}{d_0} = 2H' + \frac{H'^2}{2} \quad H' : \text{normalized wave height} = H / d_0$$

Two solitary waves with normalized wave height  $H/d_0$  at 0.05 and at 0.2 are used for the present numerical simulation. These two problems use the meshes of 700x40 elements. The Reynolds number  $Re$  is computed to 100,000, time increment  $dt$  is set

for 0.05, space increment  $dx$  at 0.05,  $dy$  at 0.05, particle space increment  $dl$  is set for 0.01. The water surface profiles obtained from the present numerical model with a solitary wave climbing up the vertical wall are shown in Fig.4-23 and Fig.4-24. From Fig.4-23 and Fig.4-24 it is seen that the wave heights at the vertical walls are greater than twice of the incident wave height as expected. The present numerical results of normalized maximum run-up are compared with Laitone's analytical solution (1960), and the numerical results from Hayashi (1991), Ramaswamy (1987), Grilli (1994) and Pirooz (1996). The comparisons are shown in Tables 4.1 and 4.2. From Table 4.1 and Table 4.2, the results of present numerical model are fairly close to the results of other researchers, and are much closer to the analytical solutions. It should be noted that Grilli solved the run-up problem using potential flow theory. Pirooz, Hayashi and Ramaswamy employed the Navier-Stokes equation with a Lagrangian description in their numerical models.

<i>Normalized Amplitude <math>H/d_0 = 0.05</math></i>			
<u>Numerical model</u>	<u><math>dt</math></u>	<u>No. of element</u>	<u><math>R/d_0</math> ( maximum run-up)</u>
Present study (2001)	0.05	700	0.1015
Pirooz (1996)	0.025	960	0.1028
Hayashi (1991)	0.01	1920	0.1026
Analytical solution (1960)	N/A	N/A	0.1012

**Table 4.1 Comparison of the maximum run-up for a solitary wave with a normalized amplitude  $H/d_0 = 0.05$  at the time when the wave climbs on the vertical wall.**

$H/d_0 = 0.05 ; T = 9.89$



Fig. 4-23 The numerical results of normalized free surface profile ( $y/d_0$ ) for the solitary wave with  $H/d_0=0.05$  when the run-up height on the right wall becomes maximum.

$H/d_0 = 0.2 ; T = 9.41$

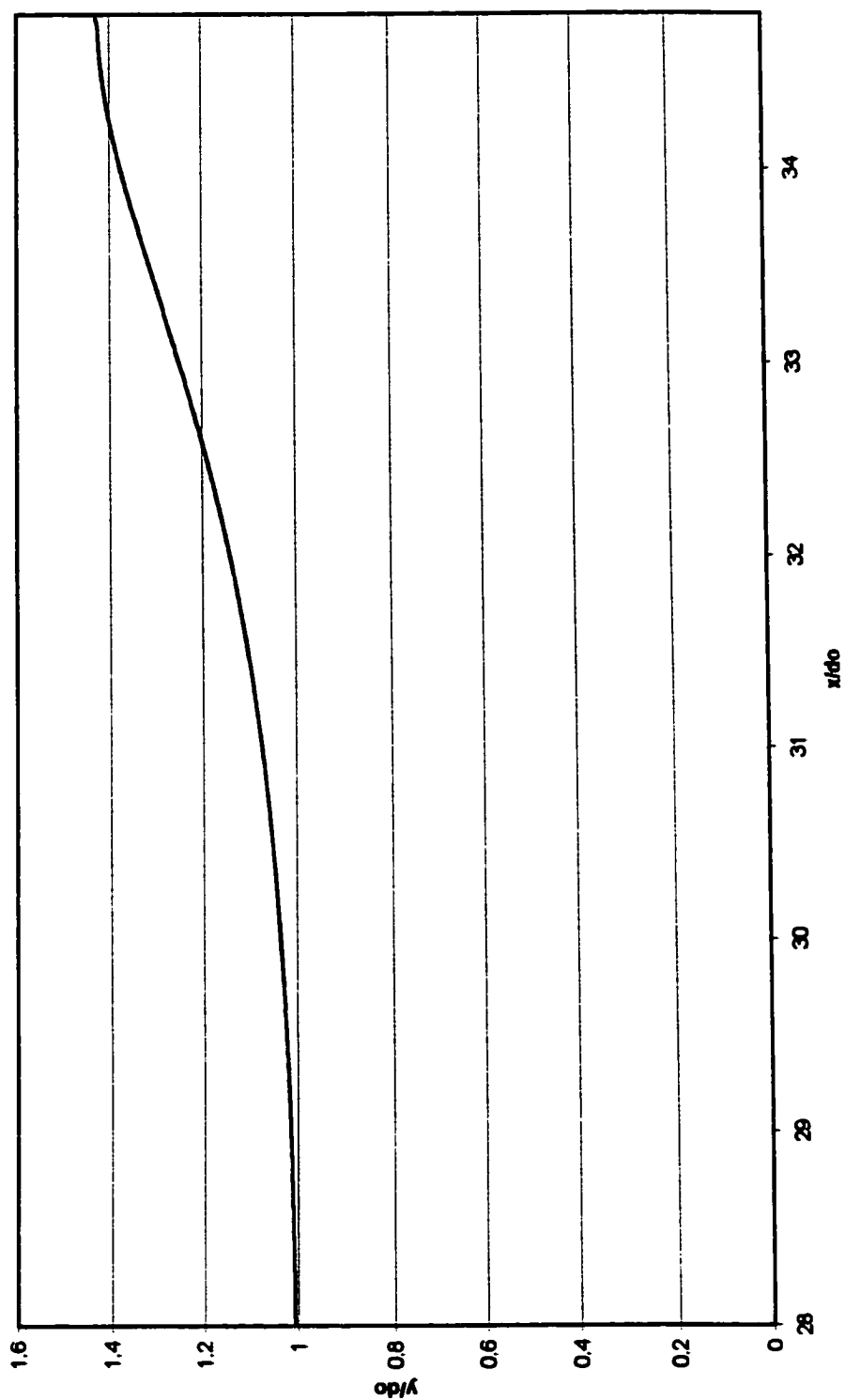


Fig. 4-24 The numerical results of normalized free surface profile ( $y/d_0$ ) for the solitary wave with  $H/d_0=0.2$  when the run-up height on the right wall becomes maximum.

<i>Normalized Amplitude <math>H/d_0 = 0.2</math></i>			
<u>Numerical model</u>	<u>dt</u>	<u>No. of element</u>	<u>R/d<sub>0</sub> ( maximum run-up)</u>
Present study (2001)	0.05	700	0.4297
Pirooz (1996)	0.025	640	0.4478
Hayashi (1991)	0.01	2048	0.4486
Ramaswamy (1987)	0.02	2048	0.448
Grilli (1994)	N/A	N/A	0.425
Analytical solution (1960)	N/A	N/A	0.420

**Table 4.2 Comparison of the maximum run-up for a solitary wave with a normalized amplitude  $H/d_0 = 0.2$  at the time when the wave climbs on the vertical wall.**

Chan and Street (1970) stated that the Eulerian method is more stable than the Lagrangian method after long time steps for problems of wave propagation in the constant water depth medium. The method of computing the free surface positions in the present numerical model is based on the Eulerian method. The present numerical model modifies the free-surface boundary condition. Near the free surface, the pressure  $p = p_a$  ( $p_a$  is defined as the applied pressure on the free surface) is applied at the exact location of the surface and not in a nearby cell center where pressures are usually defined. Due to these two modifications, it is shown that the larger time step,  $\Delta t$ , and fewer mesh elements (when compared with other numerical models) can be used in the present numerical model. The numerical results compare well with analytical results. The present model will save computation time and computer memory when compared with other numerical models.



### 4.3 Run-up of Solitary Wave on Different Sloping Beaches

In this application, the present study employed a different description, using the Lagrangian method to simulate the free surface problem for a solitary wave propagating in the rectangular channel and shoaling onto three different sloping beaches: steep slope ( $S=1, 0.58$ ) and mild slope ( $S=0.05$ ). Fig.4-25 provides a definition sketch used for this application.

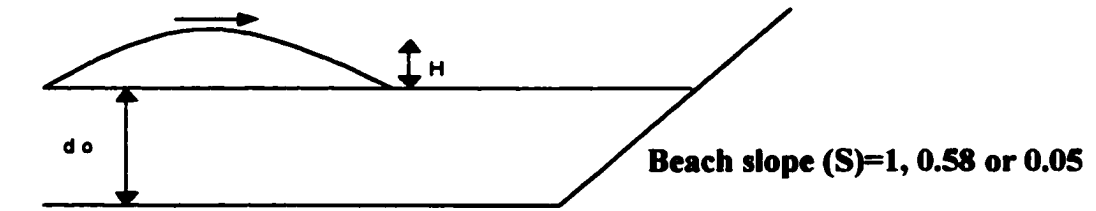


**Figure 4-25: Solitary wave propagating and running up a sloping beach**

In 1997, Grilli, et al. stated that the limit between breaking and non-breaking solitary waves was determined by the non-dimensional parameter  $S_o$ , called the slope parameter and defined as  $SL_o/d_o$ .  $S$  is the beach slope,  $d_o$  is the constant water depth, and the  $L_o$  is a characteristic horizontal length scale for the initial wave. Using Boussinesq's solitary wave theory, one obtains

$$L_o = \frac{2d_o}{\sqrt{3H_o/d_o/4}} \arctan h \frac{\sqrt{3}}{3}.$$

When this length scale is inserted into the breaking criteria for  $S_o = SL_o/d_o$ , one obtains:

$$S_o = 1.521 \frac{S}{\sqrt{H_o/d_o}} .$$

Grilli (1997) summarized different type of breaking phenomena as follows:

- (1)  $S_o > 0.37$ , the wave doesn't break
- (2)  $0.3 < S_o < 0.37$  with  $5.8 < H_b/d_b < 9.1$ , the surging breaking
- (3)  $0.025 < S_o < 0.3$  with  $1.0 < H_b/d_b < 5.8$ , the plunging breaking
- (4)  $S_o < 0.025$  with  $H_b/d_b < 1.0$ , the spilling breaking

In the present model, the incident solitary wave height is set at  $H_o/d_o = 0.48$ . Thus, for the slope beach,  $S = 1$  ( $45^\circ$ ), the value of  $S_o$  is computed to be 2.195, so the solitary wave won't break on this slope. For wave at  $H_o/d_o = 0.17$ , with the slope beach,  $S = 0.58$  ( $30^\circ$ ), the value of  $S_o$  is found to be 2.14, so the solitary wave will not break on this slope. For wave amplitude at  $H_o/d_o = 0.28$  and with the slope beach,  $S = 0.05$  ( $2.88^\circ$ ), the value of  $S_o = 0.144$ ; thus, the solitary wave will break and the breaker type will be plunging breaker.

#### 4.3.1 Run-up of Solitary Wave on a $S = 1$ Slope ( $45^\circ$ )

This first example of present numerical study on run-up of solitary wave used the experimental condition of Camfield and Street (1968). The solitary wave, with finite amplitude  $H/d_0 = 0.48$  and constant depth  $d_0 = 1$ , propagates onto a  $45^\circ$  sloping beach (steep slope). The beach slope is steep, so the solitary wave does not break on the beach. The present model employs the meshes consisting  $300 \times 50$  elements and the Reynolds number,  $Re = 80,000$ , time increment  $dt = 0.05$ , space increment  $dx = 0.08$ ,  $dy = 0.08$ , ( $S = \tan 45^\circ = dy/dx = 1$ ), particle space increment  $dl = 0.01$ , and normalized time  $T = t(g/d)^{0.5}$ . The normalized free surface depths in terms of the normalized distance for the above solitary wave are presented from Fig. 4-26 to Fig. 4-28 at different times. The solid lines are the present numerical results, the dotted lines are experimental data obtained by Camfield and Street (1968). It is seen from these figures that the free surface profiles of the present model compared well with the data of Camfield and Street. The normalized maximum run-up ( $R/d_0$ ) in the present study is 1.2824 and the experimental data in Camfield and Street is 1.27. Based on these comparisons of free surface profiles and normalized maximum run-up ( $R/d_0$ ), the present numerical model is found to be applicable for simulating run-up of solitary waves onto steep slope.

#### **4.3.2 Run-up of Solitary Wave on a $S = 0.58$ Slope ( $30^\circ$ )**

This present numerical model is also applied to the same experimental conditions conducted by Lin, et al. (1999). Lin, et al. employed a particle image velocimetry

$H/d_0 = 0.48$  ;  $T = 5$

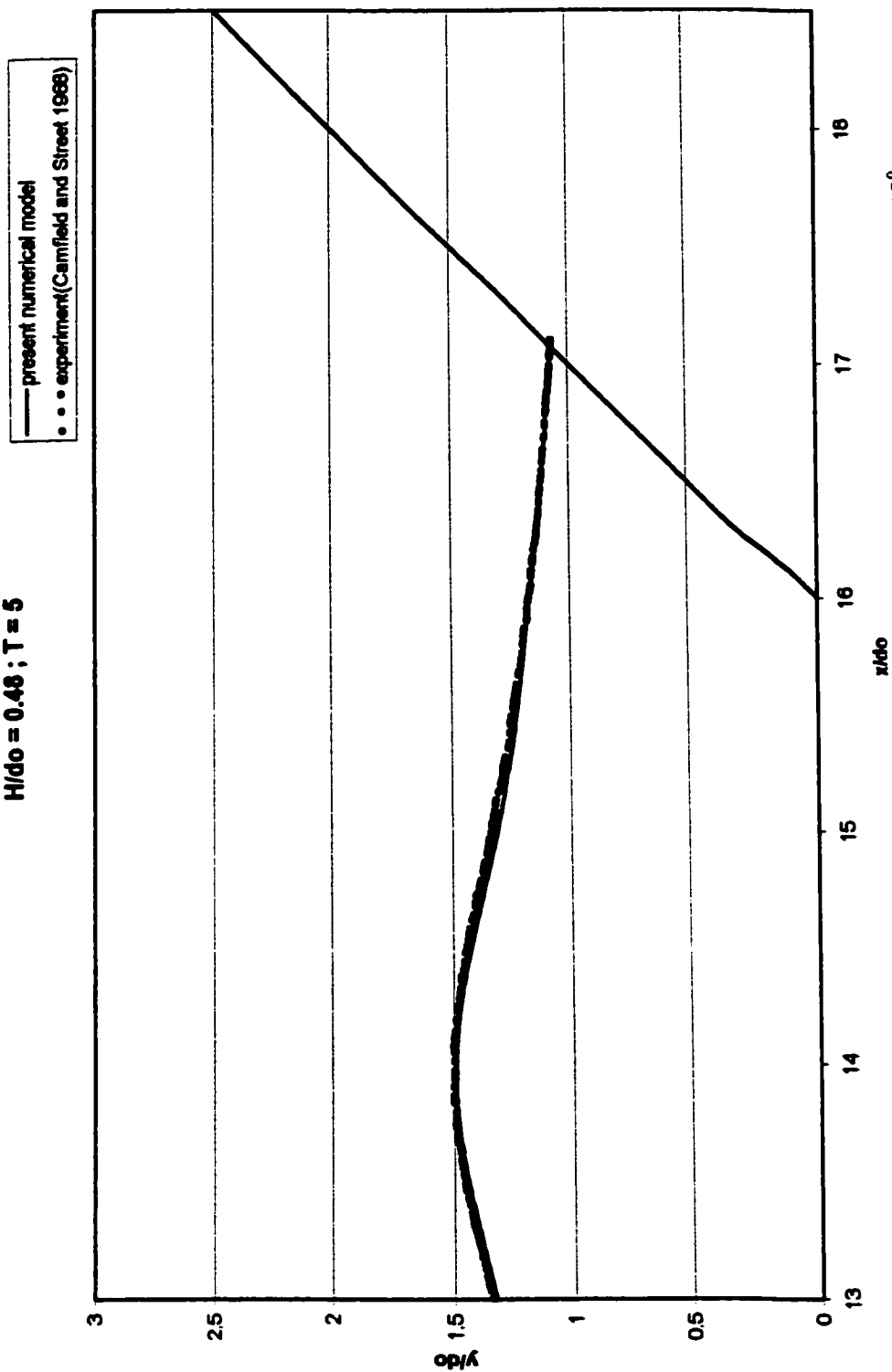
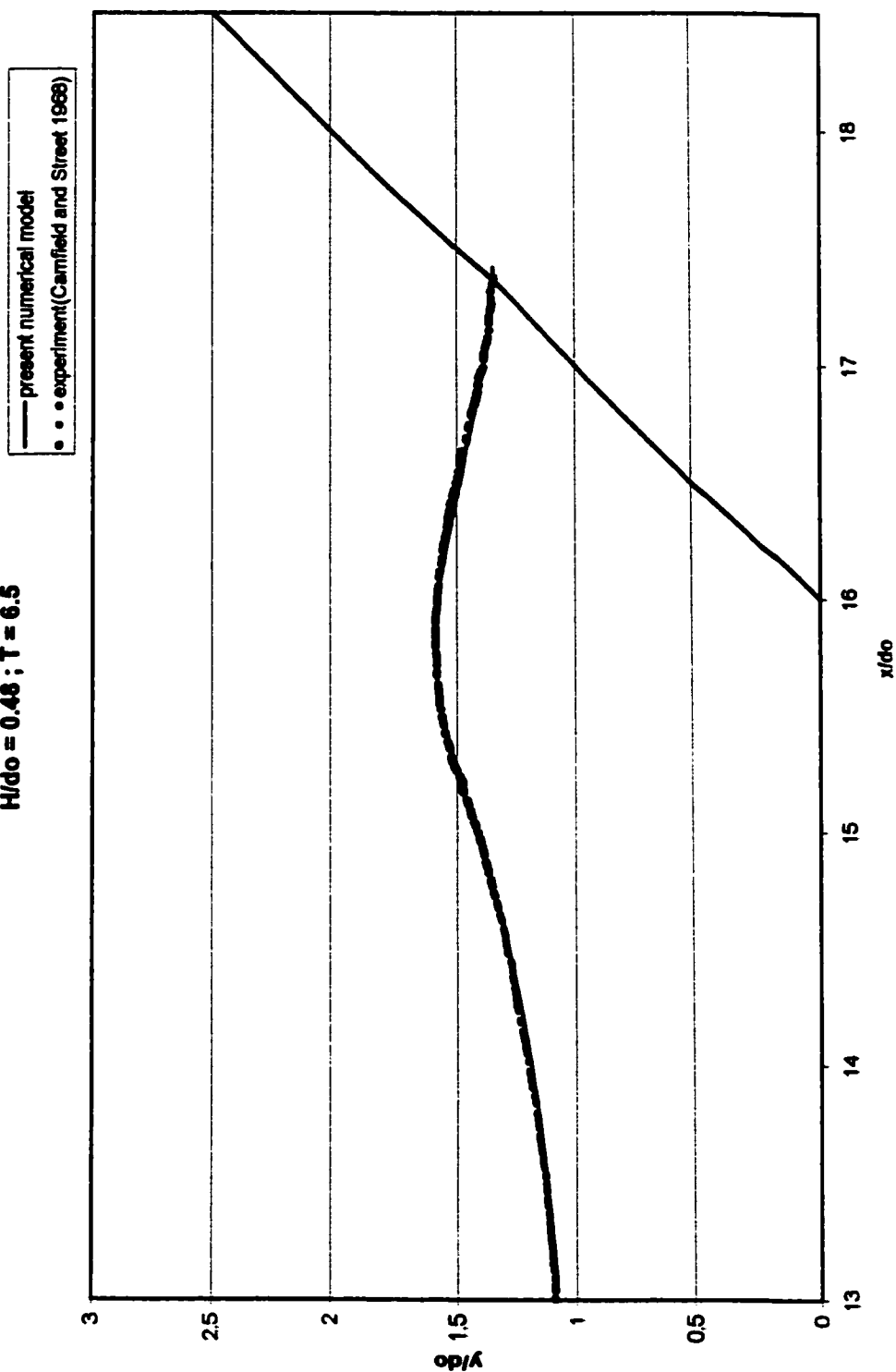
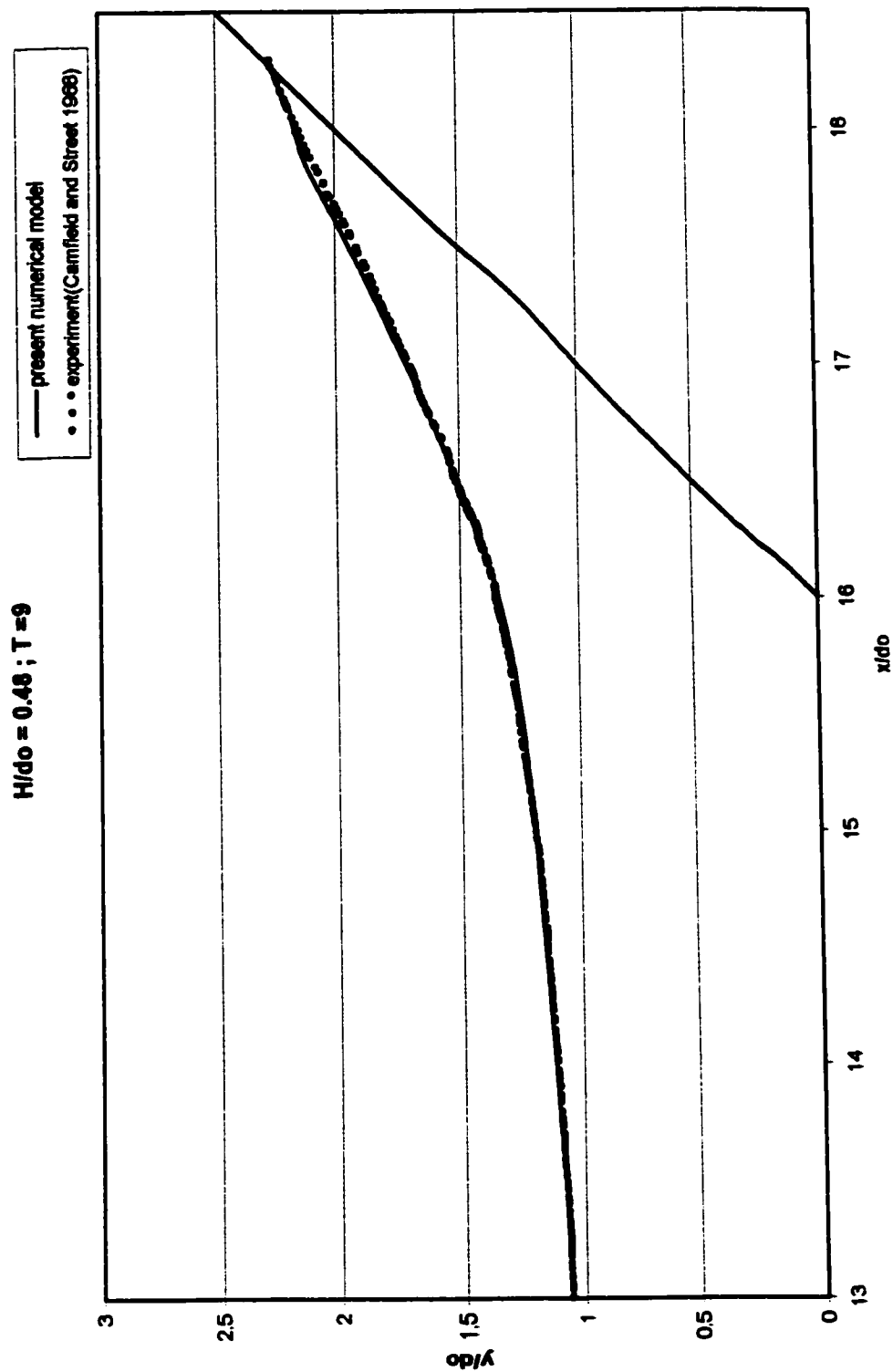


Fig. 4-26 Comparison of the free surface profiles of a solitary wave with  $H/d_0=0.48$  running up on a  $45^\circ$  slope at non-dimensional time  $T=5$ . The solid line is the results of present model and the dotted lines are the experimental data of Camfield and Street. (1968)

$H/d_0 = 0.48$  ;  $T = 6.5$



**Fig. 4-27 Comparison of the free surface profiles of a solitary wave with  $H/d_0=0.48$  running up on a  $45^\circ$  slope at non-dimensional time  $T=6.5$ . The solid line is the results of present model and the dotted lines are the experimental data of Camfield and Street. (1968)**



**Fig. 4-28 Comparison of the free surface profiles of a solitary wave with  $H/d_0=0.48$  running up on a  $45^\circ$  slope at non-dimensional time  $T=9$ . The solid line is the results of present model and the dotted lines are the experimental data of Camfield and Street. (1968)**

(PIV) to measure the free surface profile and the spatial distribution of velocity for solitary wave run-up on steep beach. The solitary wave, with finite amplitude  $H/d_0$  at 0.17 and the constant depth  $d_0$  at 0.16 meter, propagates toward a  $30^\circ$  sloping beach (steep slope). Since the sloping beach for this case is steep, thus, the solitary wave does not break on the beach. The present model employs the meshes consisting  $300 \times 50$  elements and the Reynolds number,  $Re = 80,000$ , time increment  $dt = 0.05$ , space increment  $dx = 0.08$ ,  $dy = 0.046$ , ( $S = \tan 30^\circ = dy/dx = 0.58$ ). Particle space increment  $dl$  is 0.01, and normalized time  $T$  is  $t(g/d)^{0.5}$ . The normalized free surface depths in terms of the normalized distance for the above solitary wave are presented in Fig. 4-29 and Fig. 4-31 for different values of dimensionless time ( $T$ ). Fig.4-30 and Fig.4-32 show the velocity field and free surface varied simultaneously on the sloping beach at different times. It is obvious that the solitary wave does not break on this steep slope.

Fig.4-29 and Fig.4-30 show the wave climbing up the sloping beach at normalized time  $T = 8.5$ . From Fig.4-30 the fluid particles on the slope are found to be moving in the direction parallel to the sloping beach. As can be seen from the computed results the horizontal velocity component in constant water depth region is nearly uniform throughout the depth (Fig.4-33,  $x/d_0 = 15.4$ ). However, the horizontal velocity components on the sloping beach region increase linearly from the bottom to the free surface (Fig.4-33,  $x/d_0 = 16.4$ , and  $17.4$ ). This non-uniform

$H/d_0 = 0.17$   $T = 8.5$

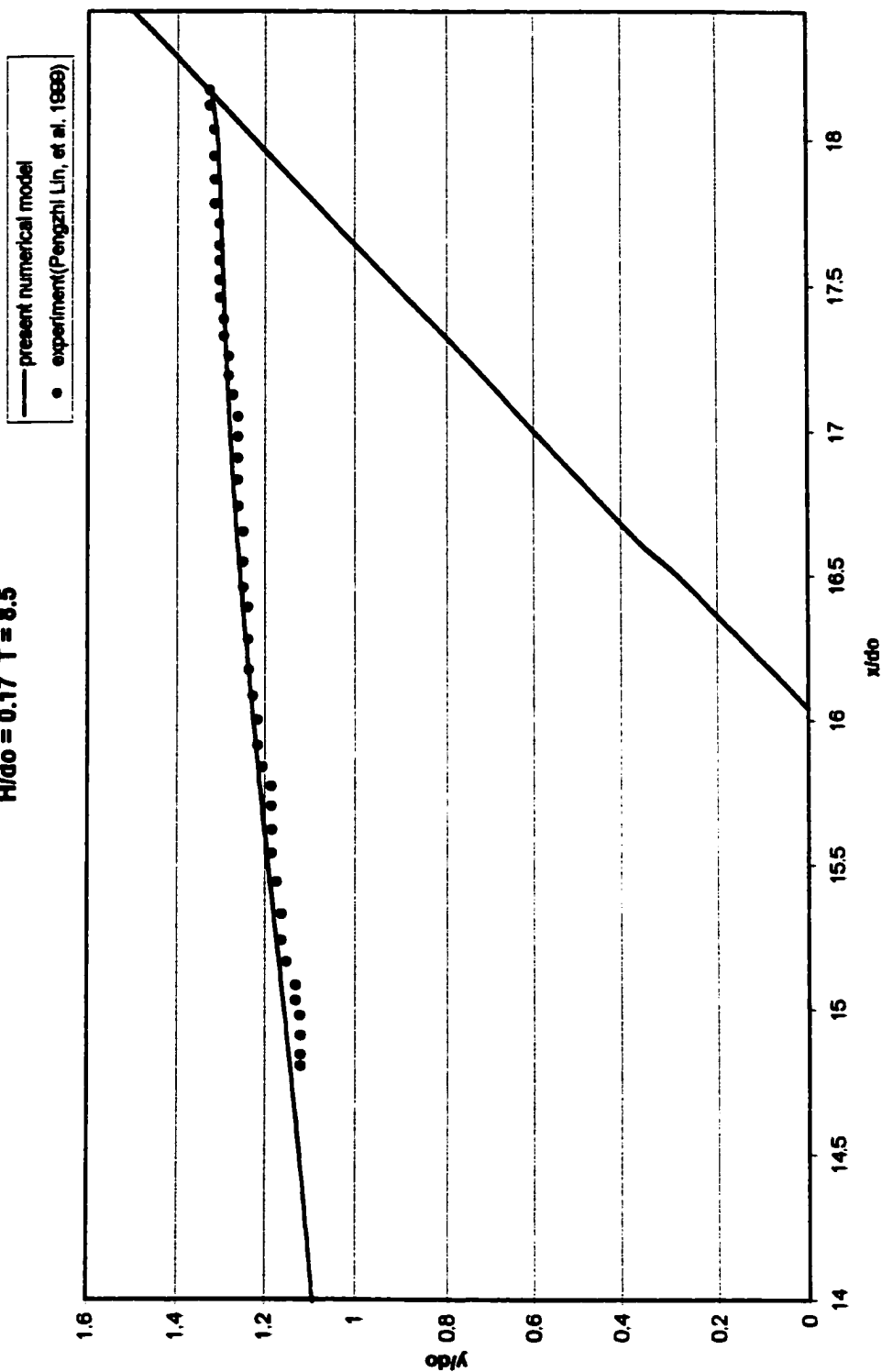


Fig. 4-29 Comparison of the free surface profiles of a solitary wave with  $H/d_0=0.17$  running up on a  $30^\circ$  slope at non-dimensional time  $T=8.5$ . The solid line is the results of present model and the solid circles are the experimental data of Pengzhi Lin, et al. (1999)



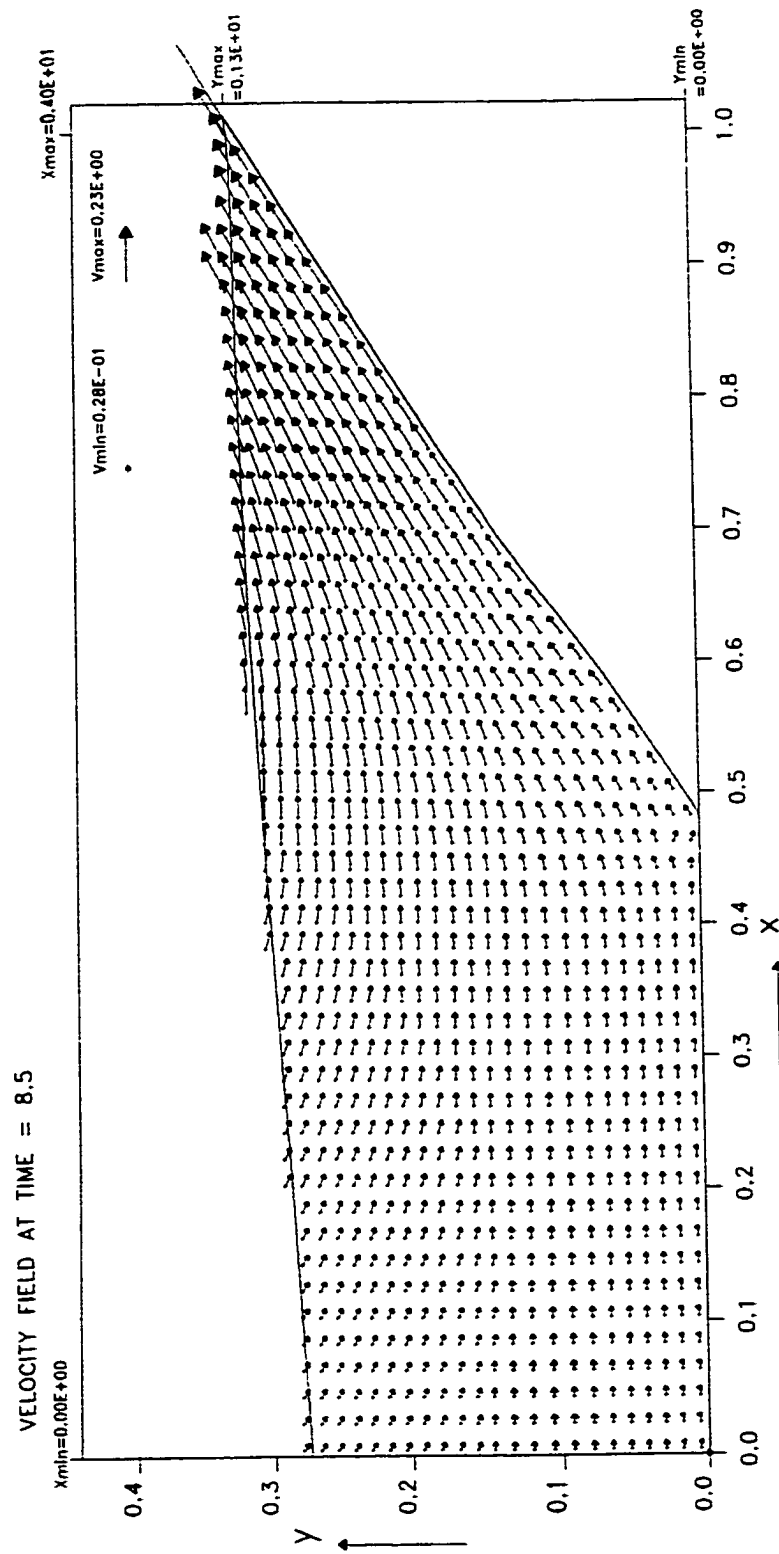


Fig. 4-30 Velocity field on a  $30^\circ$  slope at non-dimensional time  $T(\sqrt{g/d_0}) = 8.5$  by the present model. The ordinate is  $y/d_0$  and the abscissa is  $x/d_0$ .

vertical distribution of horizontal velocity component on the slope shows that the long wave approximation used by the traditional shallow water wave equations may not be correct. In Fig.4-33, it is seen that the numerical results of the present model compares well with the experimental data. It even shows a better comparison with experimental data than the turbulent model, based on the Reynolds Averaged Navier-Stokes (RANS) equation, with molecular viscosity being set to zero as employed by Lin et al (1999).

Fig.4-31 and Fig.4-32 show the velocity distribution at normalized time  $T=10.3$  when the wave almost reaches its highest run-up point, which is about  $R(\text{run-up height})/d_o = 0.454$  and is close to the experimental results of  $R/d_o = 0.431$ . In Fig.4-32, except the very small wedge region where the particles still move upward, the major portion of flow on the slope has started the rundown process. The horizontal velocity component in constant water depth is nearly uniform throughout the depth (Fig.4-34,  $x/d_o=15.4$ ), but the horizontal velocity component on the slope increase linearly from bottom to free surface (Fig.4-34,  $x/d_o=16.4$ ).

Based on Fig.4-33 and Fig.4-34, the disagreements of the horizontal velocity between the RANS turbulent model (Lin, et al., 1999) and experimental measurements are obvious, but the results of the present model appear to agree better with the experimental data. The present computer model results suggest that the shallow water waves approximation may not be valid here and the shallow water

$H/d_0 = 0.17$   $T = 10.3$

— present numerical model  
 • experiment (Pengzhi Lin, et al. 1999)

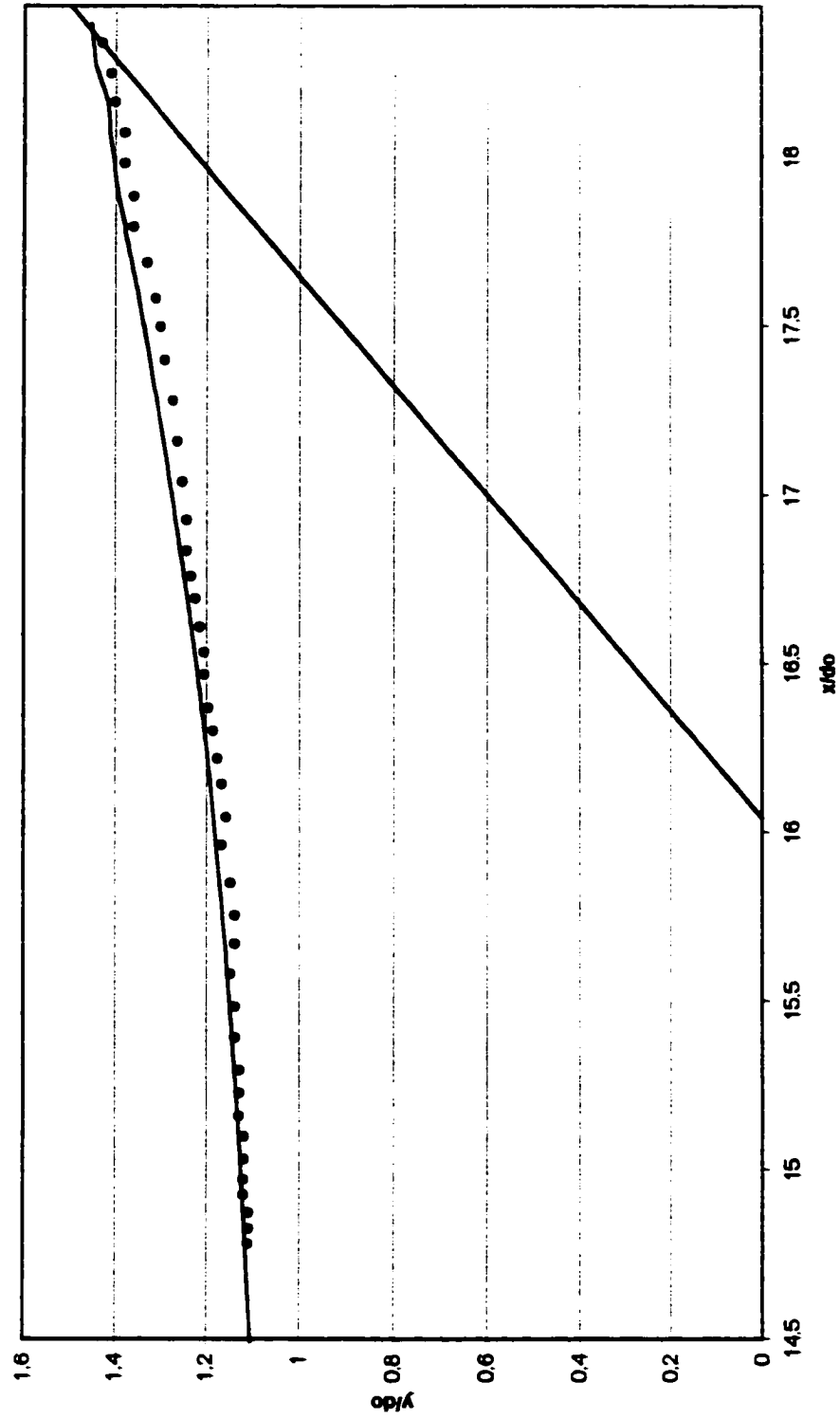


Fig. 4-31 Comparison of the free surface profiles of a solitary wave with  $H/d_0=0.17$  running up on a  $30^\circ$  slope at non-dimensional time  $T=10.3$ . The solid line is the results of present model and the solid circles are the experimental data of Pengzhi Lin, et al. (1999)

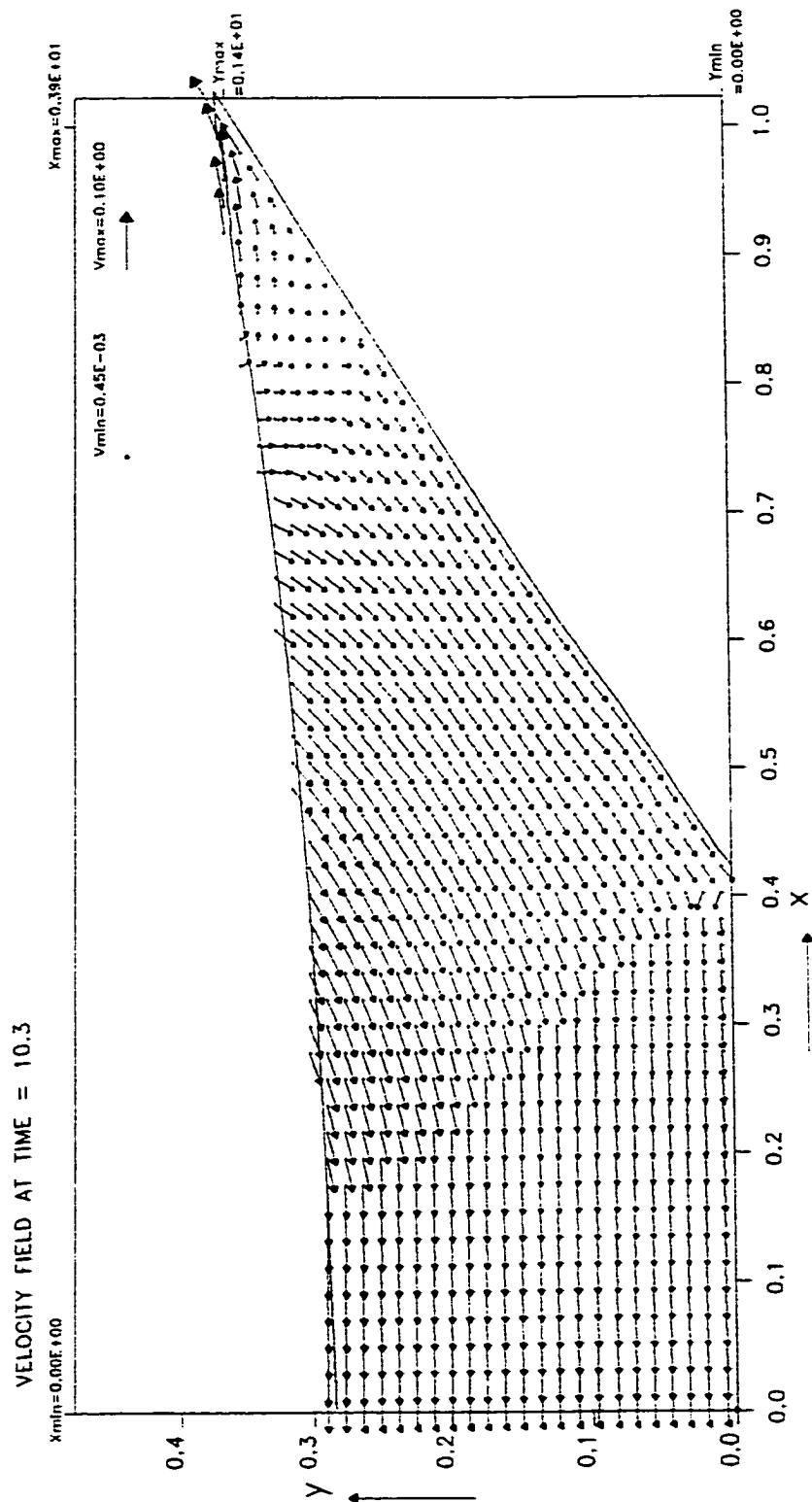


Fig. 4-32 Velocity field on a  $30^\circ$  slope at non-dimensional time  $T(t\sqrt{g/d_n}) = 10.3$  by the present model. The ordinate is  $y/d_n$  and the abscissa is  $x/d_n$ .

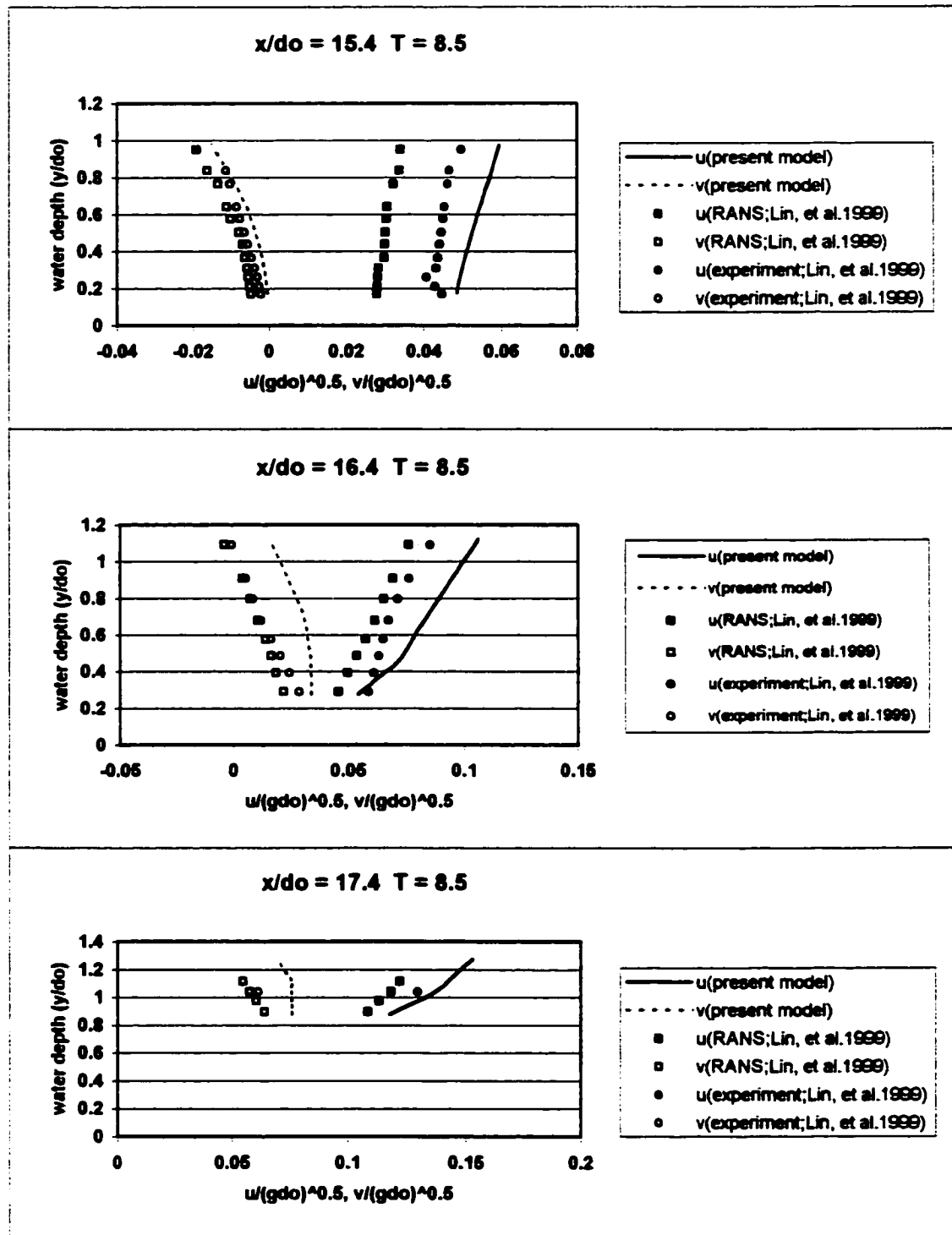


Fig. 4-33 Solitary wave run-up at  $T=8.5$ . Comparisons of vertical variation of velocities at  $x/d_o=15.4, 16.4$ , and  $17.4$ . The lines are present model, the circles are experiment by Lin, et al (1999), and the squares are numerical results by RANS method. (Lin, et al, 1999)

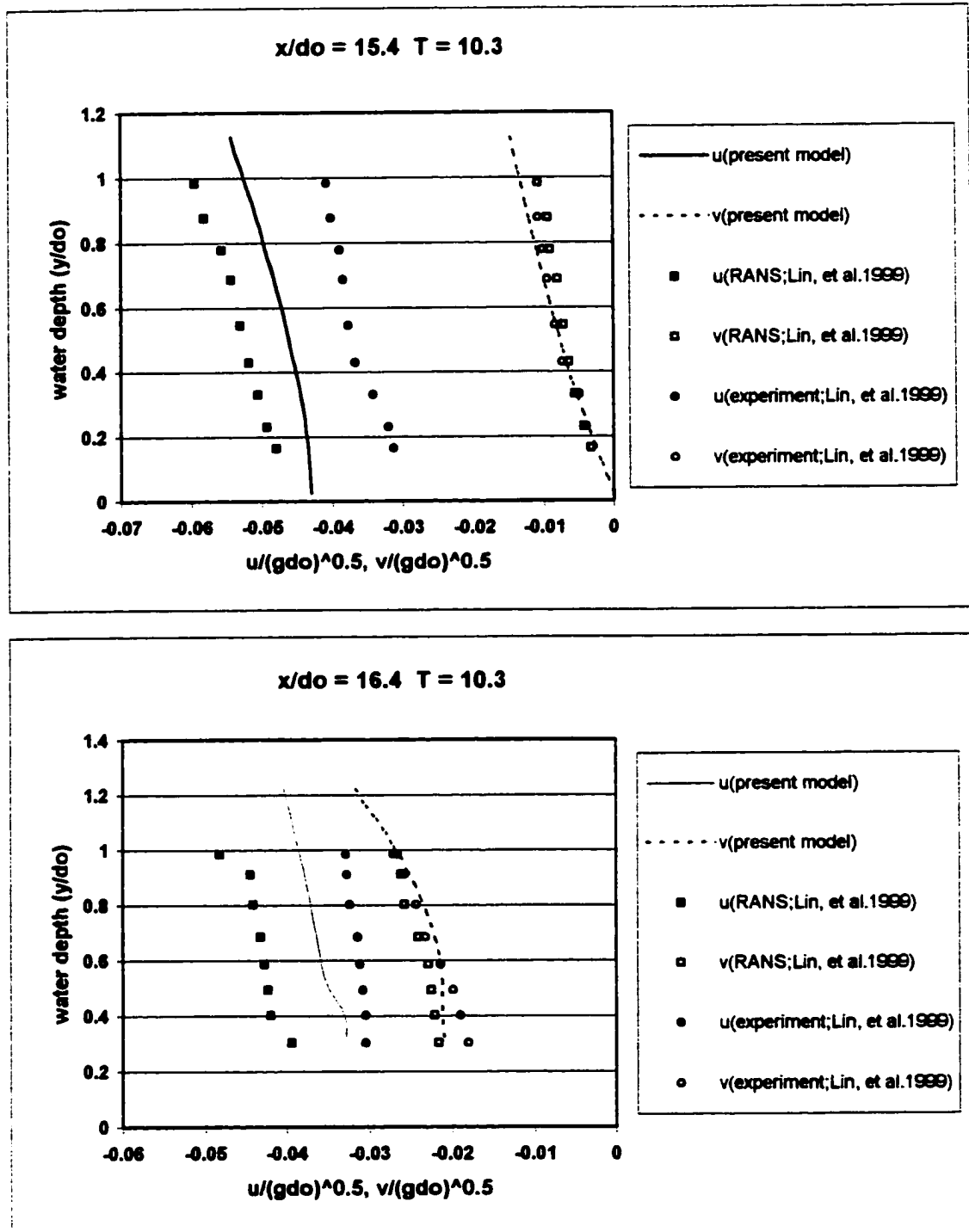


Fig. 4-34 Solitary wave run-up at  $T=10.3$ . Comparisons of vertical variation of velocities at  $x/d_o=15.4$ , and  $16.4$ . The lines are present model, the circles are experiment by Lin, et al (1999), and the squares are numerical results by RANS method. (Lin, et al, 1999)

wave equation model may produce inaccurate results in simulating long wave run-up on a steep beach, especially on velocity field computation. From the above comparisons, it is found that the overall agreement of free surface profiles is good and the velocity distribution on the slope is reasonable. So the present model also works well for simulating solitary wave shoaling on steep beaches.

If the sloping beach is viewed as the slope of the dikes or sea walls, to minimize the effect of extra scouring due to reflection of waves, the slope of sea walls or dikes should not be more than 1 in 3. This could be one of the reasons that Dutch dikes mostly have slopes of 1 in 4 or even milder. (Herbich, 1999)

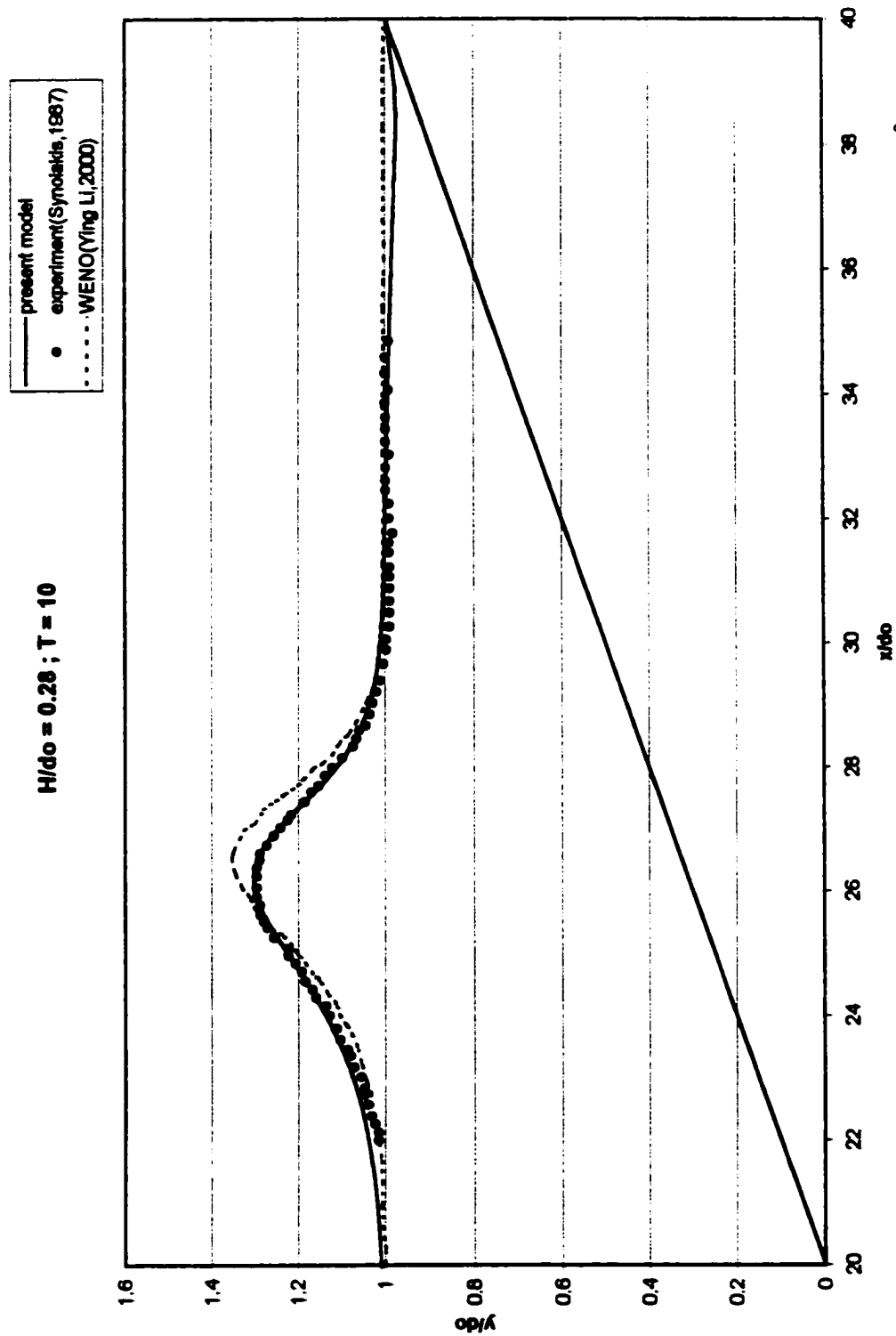
#### **4.3.3 Run-up of Solitary Wave on a $S = 0.05$ Slope ( $2.88^\circ$ )**

An experimental setup for the breaking solitary wave study is presented in detail by Synolakis (1987). For the breaking wave case, only the free surface profile is available from experiments. The solitary wave, with finite amplitude  $H/d_0 = 0.28$  and the constant depth  $d_0$  region, propagates unto a  $2.88^\circ$  sloping beach. Since the sloping beach is mild, so the solitary wave will break on the beach. The domain of simulation for the present study has the meshes  $300 \times 160$  elements, and the Reynolds number,  $Re = 100,000$ , time increment  $dt = 0.025$ , space increment  $dx = 0.3$ ,  $dy = 0.015$ , ( $S = \tan 2.88^\circ = dy/dx = 0.05$ ), particle space increment  $dl = 0.05$ , and normalized time  $T$  is defined as  $t(g/d)^{0.5}$ . The normalized free surface depths in terms of the normalized distance for the above solitary wave are presented in Fig.4-

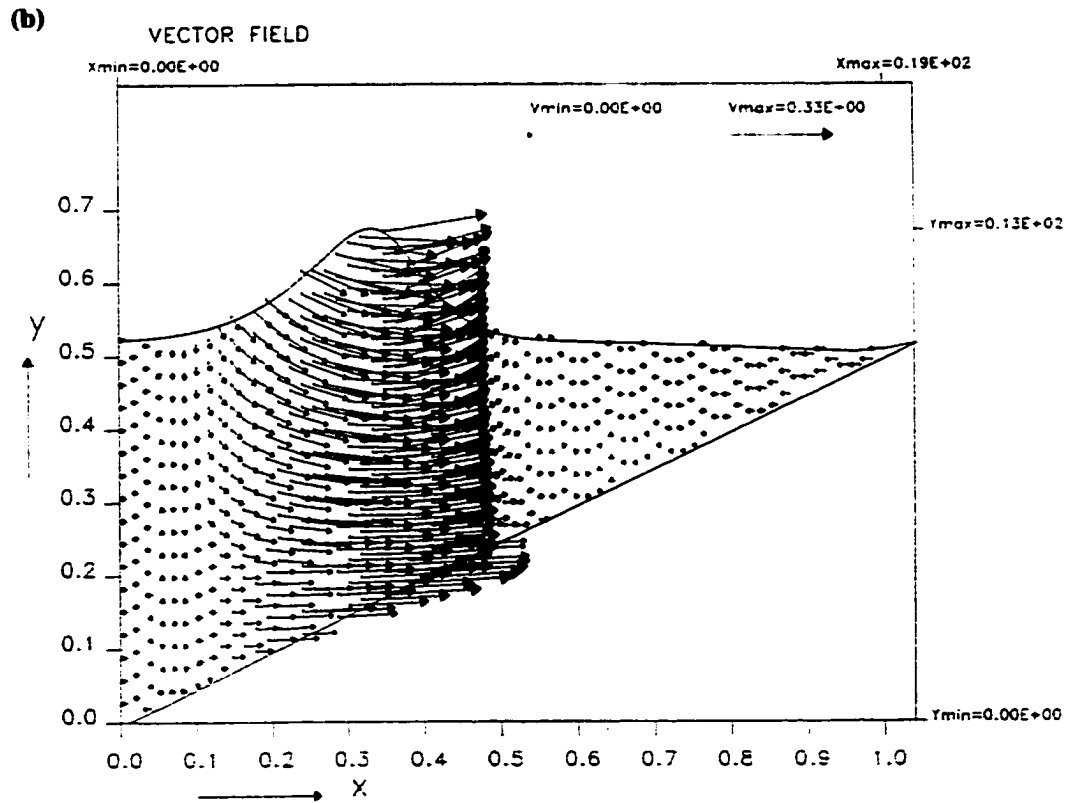
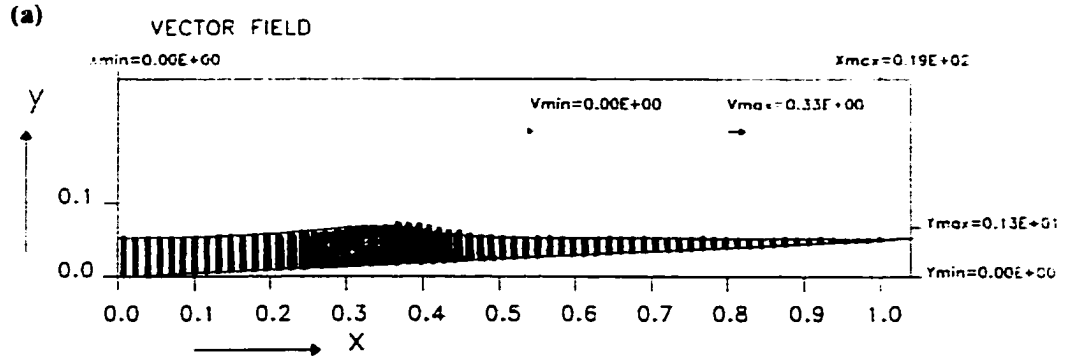
35, Fig.4-37, and Fig.4-39 for different times. The solid lines present the current solution, the solid circles are experimental data obtained by Synolakis (1987), and the dash lines are numerical results obtained by the weighted essentially non-oscillatory scheme (WENO) employed by Li (2000). Fig. 4-36, Fig.4-38, and Fig.4-40 show the velocity field and free surface varied simultaneously on the sloping beach at different times. It is obvious that the solitary wave does break on this mild slope. The horizontal and vertical velocities obtained by the present model are also compared with the numerical method called Reynolds Averaged Navier-Stokes (RANS) by Lin et al. (1999) and are shown from Fig.4-41 to Fig.4-43.

Fig.4-35 and Fig.4-37 show the shoaling of the solitary wave at  $T = 10$  and 15. The wave shape becomes asymmetric and the amplitude increases because of the decrease of water depth. Comparing Fig.4-35 with Fig.4-37, one observes that the further steepening of wave front causes the initiation of wave breaking process. Fig.4-39 shows the consequent rapid decrease of wave height and the fast change of surface profile. The velocity distributions of the shoaling process are shown in Fig.4-36, Fig.4-38, and Fig.4-40. Fig.4-35 and Fig.4-36 show the wave profile and the velocity field of the solitary wave when it starts to climb the slope. At this time, the wave profile is almost symmetric and the velocity distribution is similar to that of solitary wave in constant water depth, i.e., the horizontal velocity is nearly constant over water depth and the vertical velocity is zero on the bottom and





**Fig. 4-35 Comparison of the free surface profiles of a solitary wave with  $H/d_0=0.28$  running up on a  $2.88^\circ$  slope at non-dimensional time  $T=10$ . The solid line is the results of present model and the solid circles are the experimental data of Synolakis(1987), and the dash lines are the numerical results of WENO method by Ying Li(2000).**



**Fig. 4-36** The velocity field of a solitary wave with  $H/d_0=0.28$  running up on a  $2.88^\circ$  slope from  $x/d_0=20$  to  $x/d_0=40$  at non-dimensional time  $T=10$ . (a) The ordinate is  $y/d_0$  and the abscissa is  $x/d_0$ . (b) The ordinate is  $(y/d_0)*10$  and the abscissa is  $x/d_0$ .

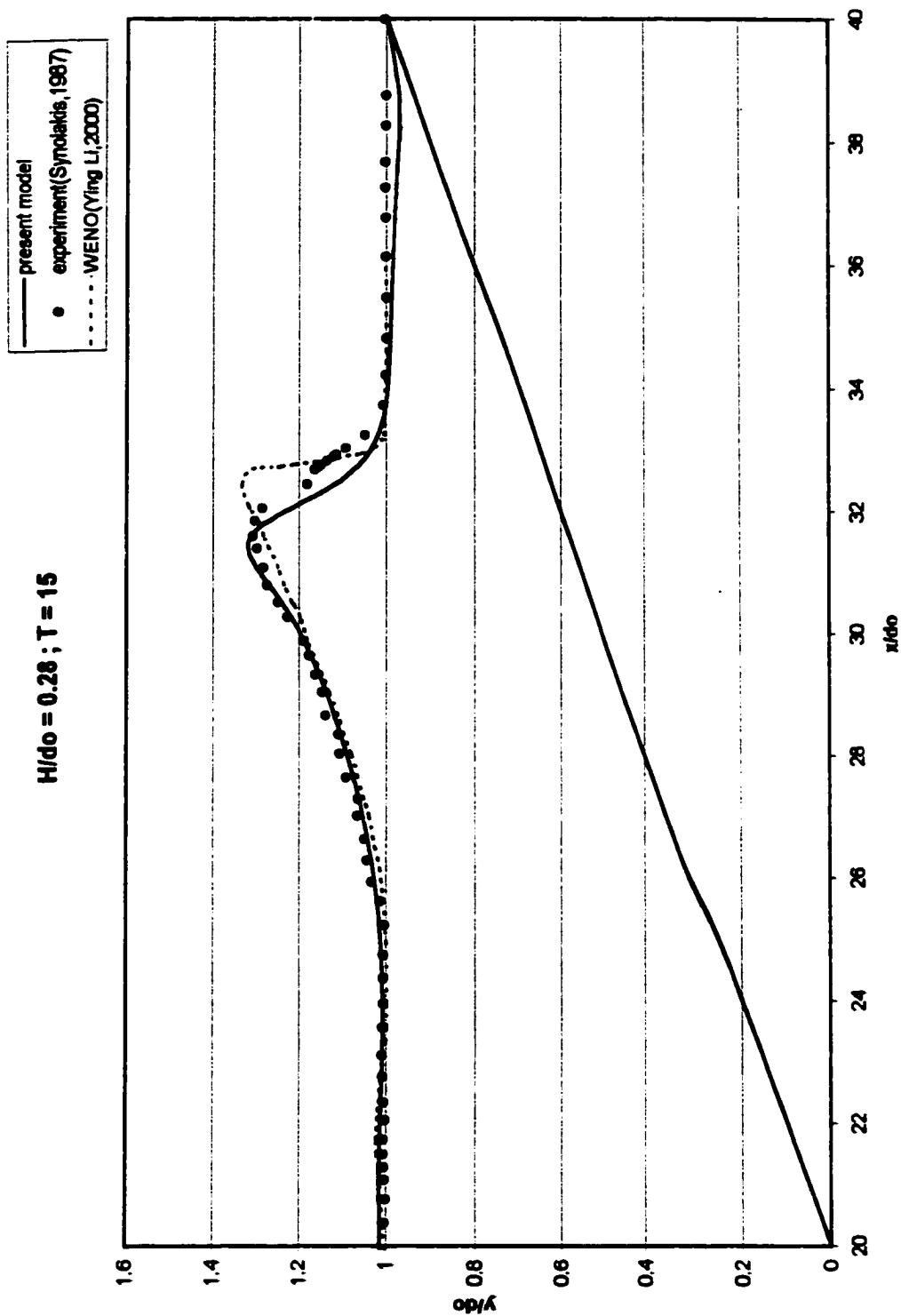
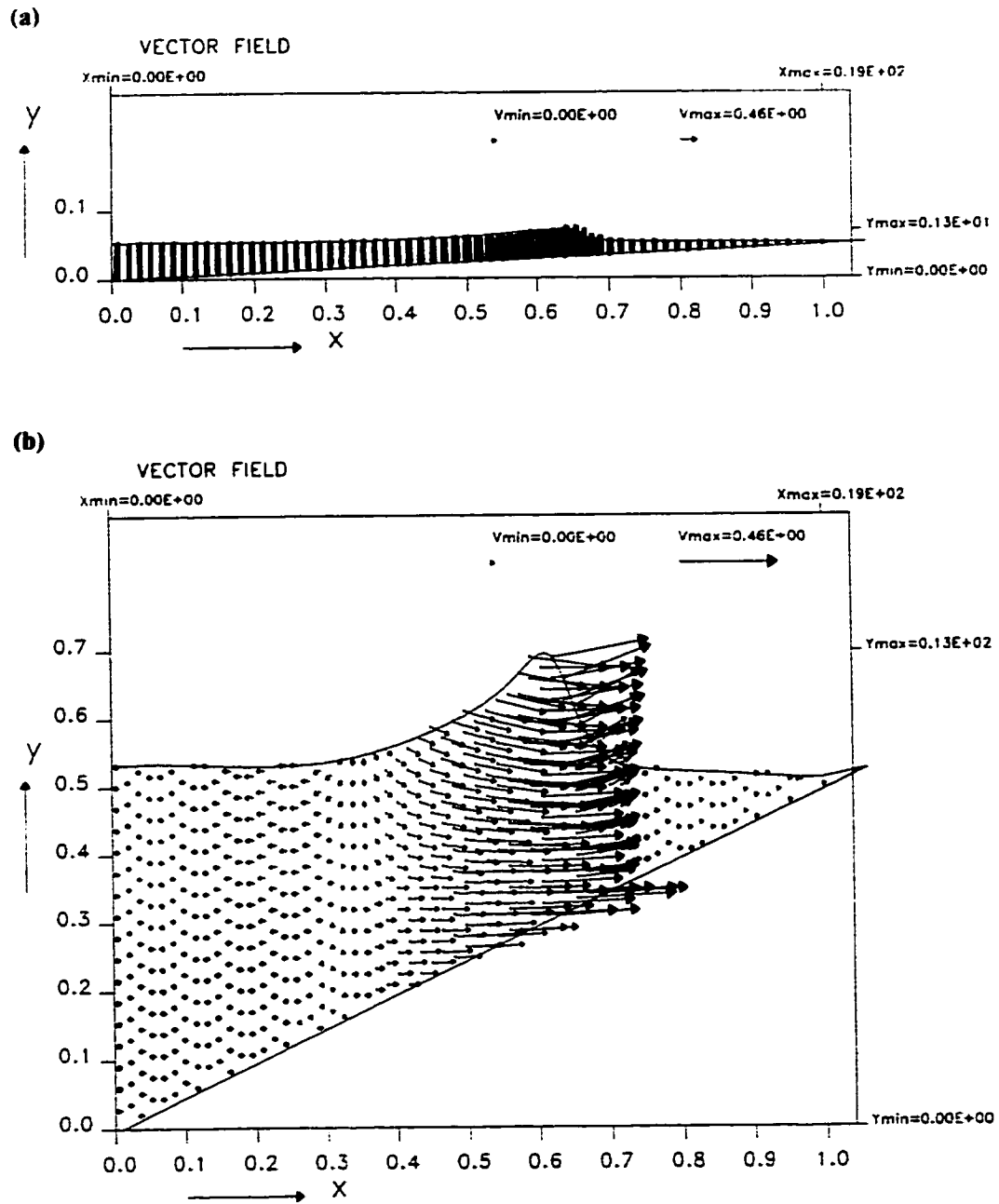


Fig. 4-37 Comparison of the free surface profiles of a solitary wave with  $H/d_0=0.28$  running up on a  $2.88^\circ$  slope at non-dimensional time  $T=15$ . The solid line is the results of present model and the solid circles are the experimental data of Synolakis(1987), and the dash lines are the numerical results of WENO method by Ying Li(2000).



**Fig. 4-38** The velocity field of a solitary wave with  $H/d_0=0.28$  running up on a  $2.88^\circ$  slope from  $x/d_0=20$  to  $x/d_0=40$  at non-dimensional time  $T=15$ . (a) The ordinate is  $y/d_0$  and the abscissa is  $x/d_0$ . (b) The ordinate is  $(y/d_0)*10$  and the abscissa is  $x/d_0$ .

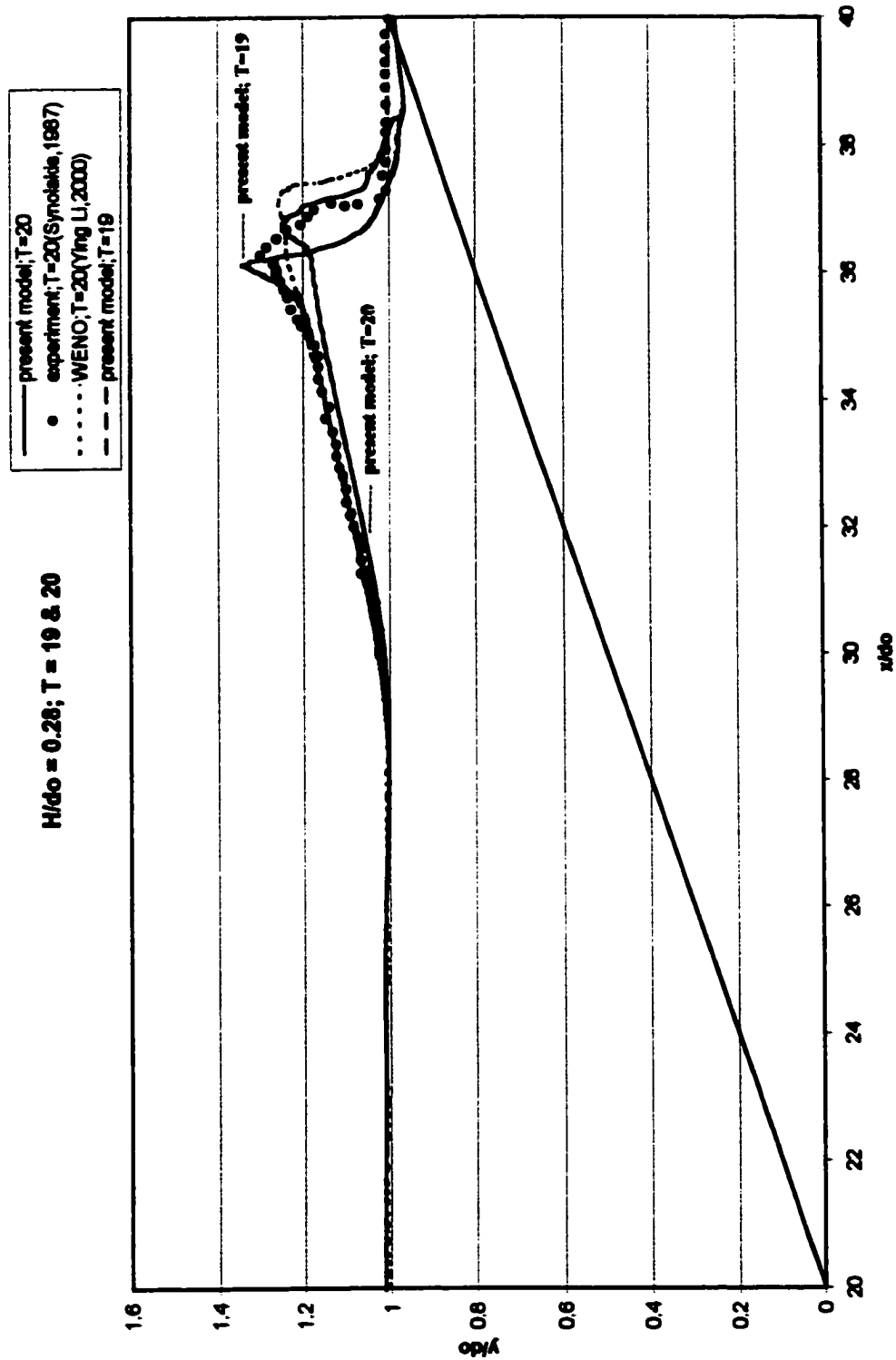
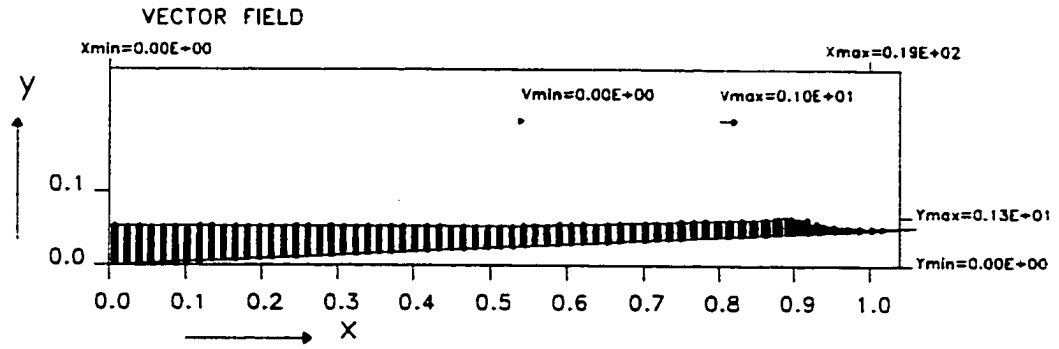
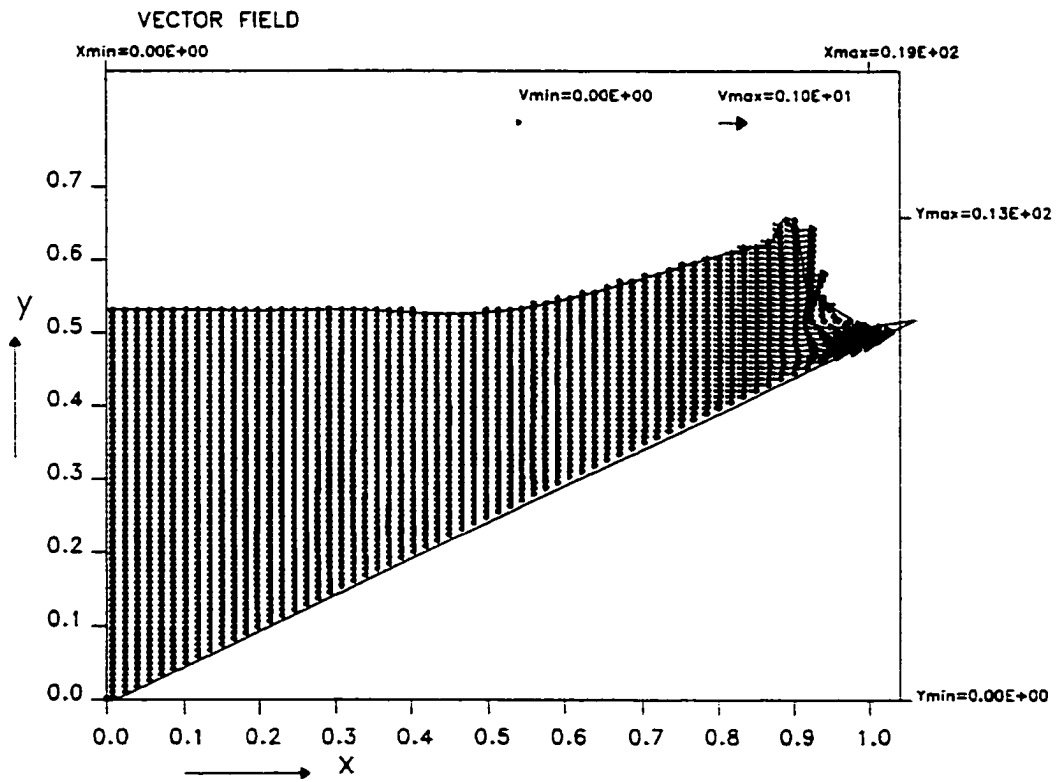


Fig. 4-39 Comparison of the free surface profiles of a solitary wave with  $H/d_0=0.28$  running up on a  $2.88^\circ$  slope at non-dimensional time  $T=20$ . The solid line is the results of present model and the solid circles are the experimental data of Synolakis(1987), and the dash lines are the numerical results of WENO method by Ying Li(2000).

(a)



(b)



**Fig. 4-40** The velocity field of a solitary wave with  $H/d_0=0.28$  running up on a  $2.88^\circ$  slope from  $x/d_0=28$  to  $x/d_0=40$  at non-dimensional time  $T=20$ . (a) The ordinate is  $y/d_0$  and the abscissa is  $x/d_0$ . (b) The ordinate is  $(y/d_0)*10$  and the abscissa is  $x/d_0$ .

increases linearly to the free surface (Fig.4-41). Fig.4-37 and Fig.4-38 show the wave profile and the velocity field when the wave crest is in the sloping beach, but before the wave breaks. The wave shape becomes asymmetric. The wave front is steepening. As a result, the horizontal velocity under the wave front is no longer constant but increases to the free surface. The vertical motion in front of the wave crest is also very strong. (Fig4-42,  $x/d_o=31.95$ ). At this time frame, Fig.4-37 shows the discrepancy at the front of the wave surface, so the Fig.4-42 at  $x/d_o=31.95$  shows the disagreement of the horizontal velocity component between the present numerical results and numerical results of RANS (Lin, 1999). But the vertical velocity shows less discrepancy in the comparison, probably because they are less sensitive to flow field. From the presented results, the present numerical results, comparing reasonably well with experimental measurements, and are closer to the experimental data than that by the WENO method (Li, 2000).

In the present model, the numerical results show that there is maximum wave height  $H_b = 0.3442$  and water depth  $d_b = 0.1942$  happening at  $T=19$ . The breaking index  $H_b/d_b = 1.77$  satisfies the condition proposed by Grilli, et al., (1997). Fig.4-39 shows the breaking process occurs between  $T=19$  and  $T=20$ . The present numerical results agree with the laboratory observations that the breaking process occurs between  $T=15$  and  $T=20$ . But the predicted water surface differs from the experimental measurements, because the horizontal velocities have large

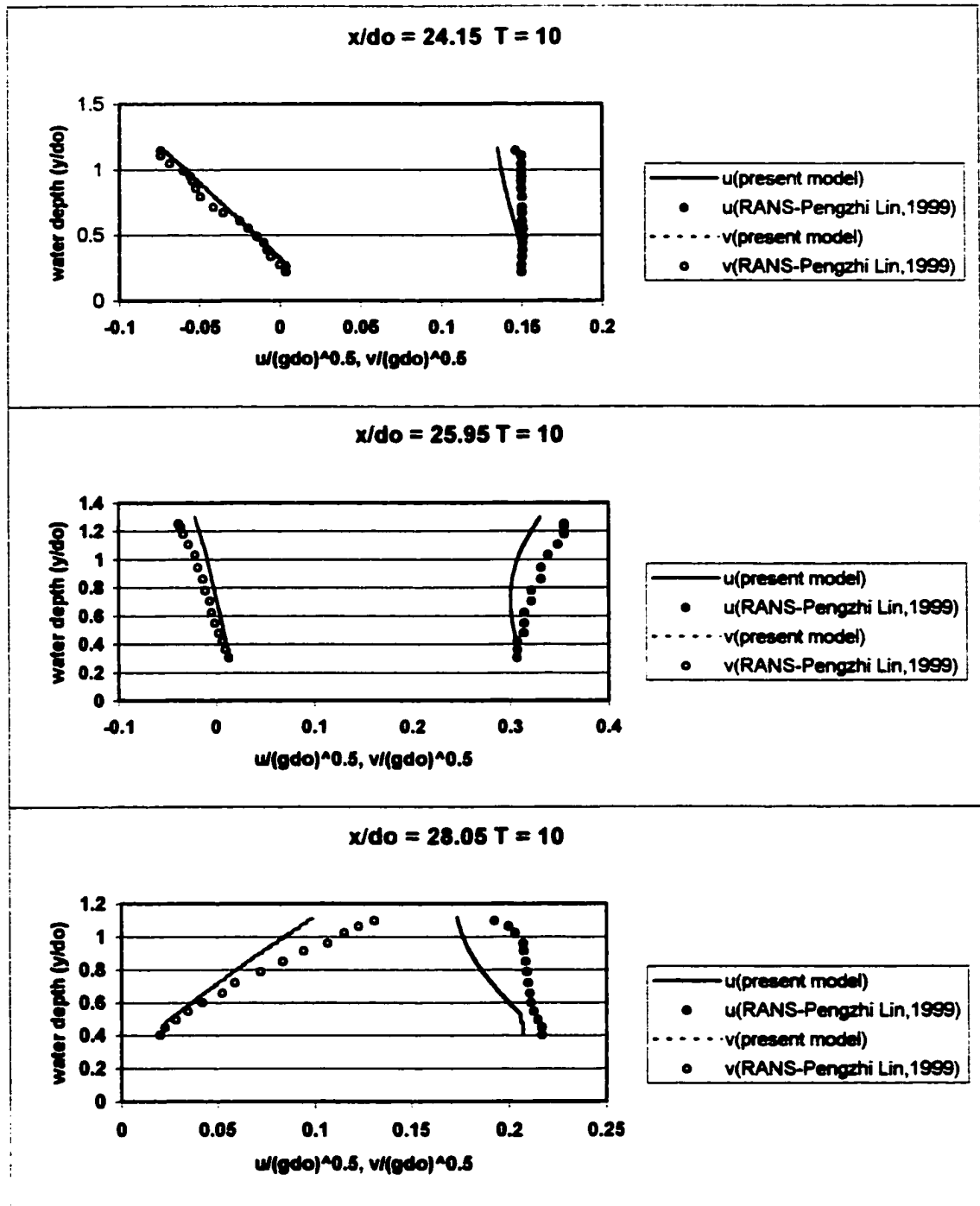


Fig. 4-41 Solitary wave run-up on a  $2.88^\circ$  slope at  $T=10$ . Comparisons of vertical variation of velocities at  $x/d_o=24.15$ ,  $25.95$ , and  $28.05$ . The wave crest is at  $x/d_o=26.21$ . The lines are present model, and the circles are numerical results by Lin, et al (1999)



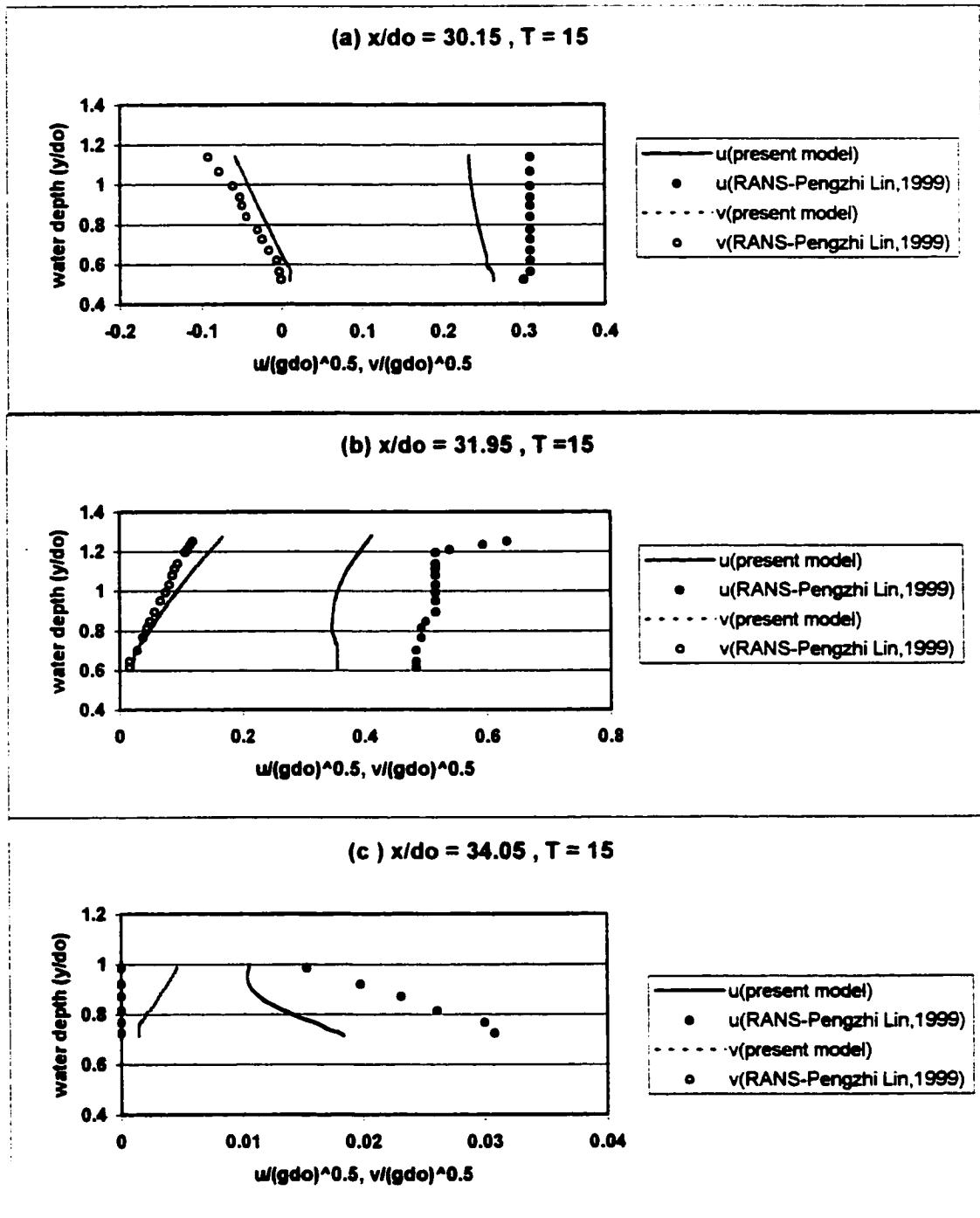


Fig. 4-42 Solitary wave run-up on a  $2.88^\circ$  slope at  $T=15$ . Comparisons of vertical variation of velocities at  $x/d_o=30.15$ ,  $31.95$ , and  $34.05$ . The wave crest is at  $x/d_o=31.44$ . The lines are present model, and the circles are numerical results by Lin, et al (1999)

discrepancy at wave front at  $T=15$ . After wave breaks, Fig.4-40 and 4-43 show the flow pattern becoming quite different. In the wave front, the particle velocity can exceed the phase velocity near the free surface, forming a layer possessing a much larger velocity than the region underneath. This layer is often referred to as the roller, which is used to generate turbulence and vorticity and is discussed by Lin and Liu (1998). Fig.4-43 at  $x/d_0=36.15$  shows that the vertical velocity under the wave crest is smaller and it is experiencing an opposite process of changing the direction from the positive to negative. This reduces the pressure underneath.

As the broken wave propagates, the present numerical model will stop. The present numerical model does not include the Reynolds stress, which may incorporate the turbulence occurring in the broken wave. But the present model can simulate the near breaking processes reasonably well. The breaking process dissipates energy in the form of turbulence and it also reduces the pressure under the wave crest and increases the pressure under the breaking wave front due to different features of the vertical acceleration of fluid particles. Therefore, the shallow water equation model, which assumes the hydrostatic pressure everywhere, may not be able to simulate the long wave shoaling on the slope, either.

#### **4.4 Wave-induced Loading on a Half-buried Pipe**

##### **4.4.1 Hydrodynamic Forces on a Half-buried Pipe Studied by Foda's Experiment**

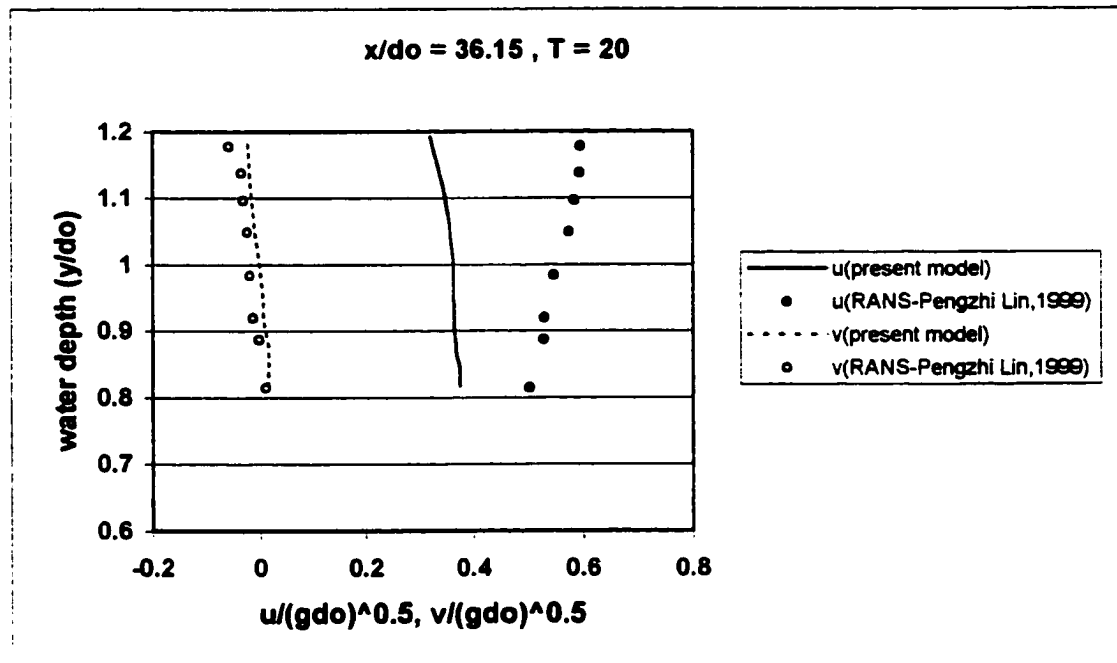
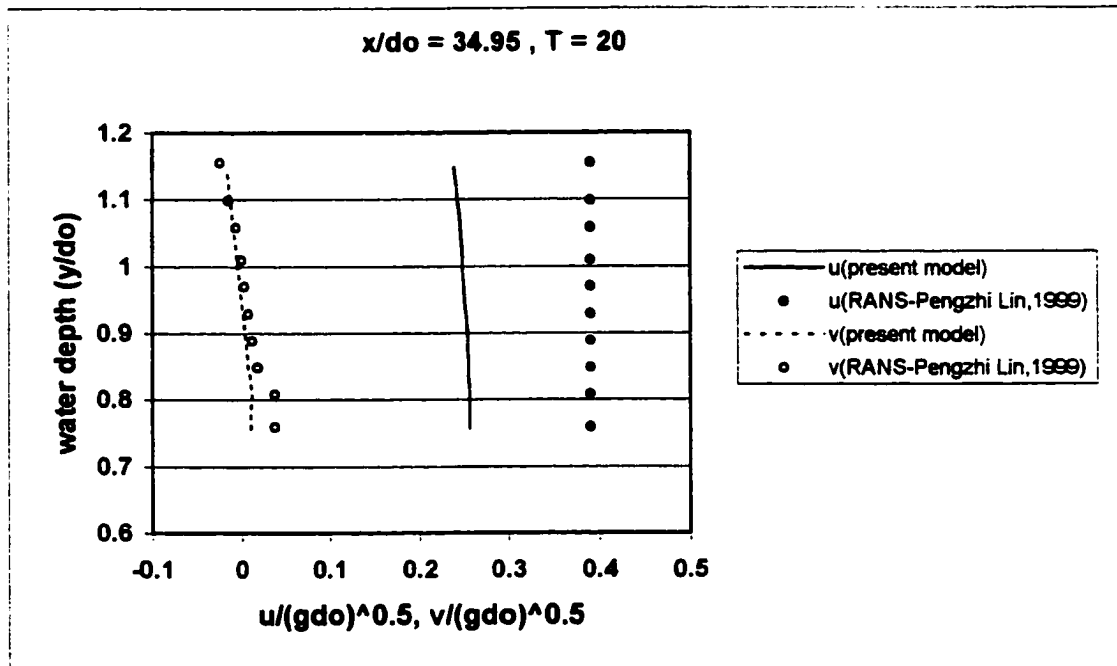


**Fig. 4-43 Solitary wave run-up on a  $2.88^\circ$  slope at  $T=20$ . Comparisons of vertical variation of velocities at  $x/d_o=34.95$ , and  $36.15$ . The wave crest is at  $x/d_o=36.76$ . The lines are present model, and the circles are numerical results by Lin, et al (1999)**

The present numerical model has also been applied to compute hydrodynamic forces on half-buried pipe. The half-buried pipe in the coastal zone is one of common coastal structures in ocean outfalls for sewage disposals. An experimental study on the periodic wave passing over the half-buried pipe is presented by Foda (1990). A layout of the experimental setup is shown in Fig.4-44.

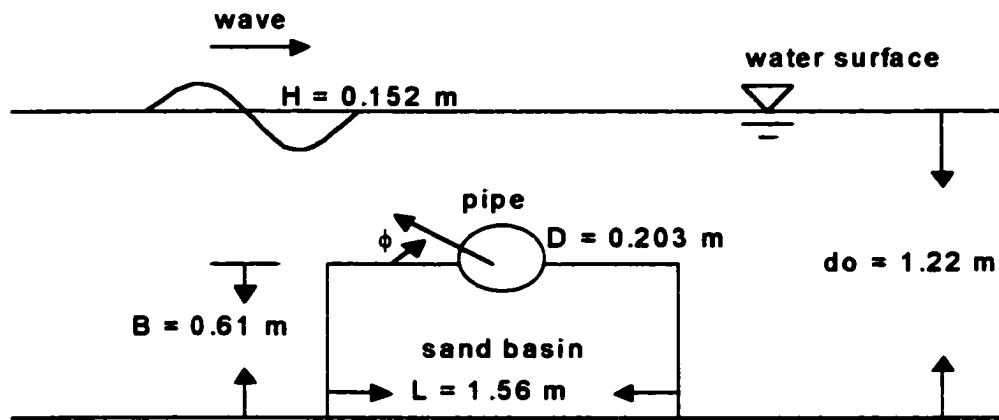


**Figure 4-44 Definition of the half-buried pipe used by Foda (1990)**

The undisturbed water depth  $d_o = 1.22$  meter, the sand basin length  $L = 1.56$  meter and height  $B = 0.61$  meter, wave height  $H = 0.152$  meter, frequency  $W = 3.0$  second, the diameter of PVC pipe  $D = 0.203$  meter. Variable used in the present numerical model are dimensionless numbers normalized by the water depth,  $d_o$ , and redefined as follows. The variables become  $d_o = 1$ ,  $L = 1.28$ ,  $B = 0.5$ ,  $H = 0.12$ ,  $W = 8.22$ ,  $D = 0.16$ , Reynolds number is computed to be 80,000, time increment  $dt =$

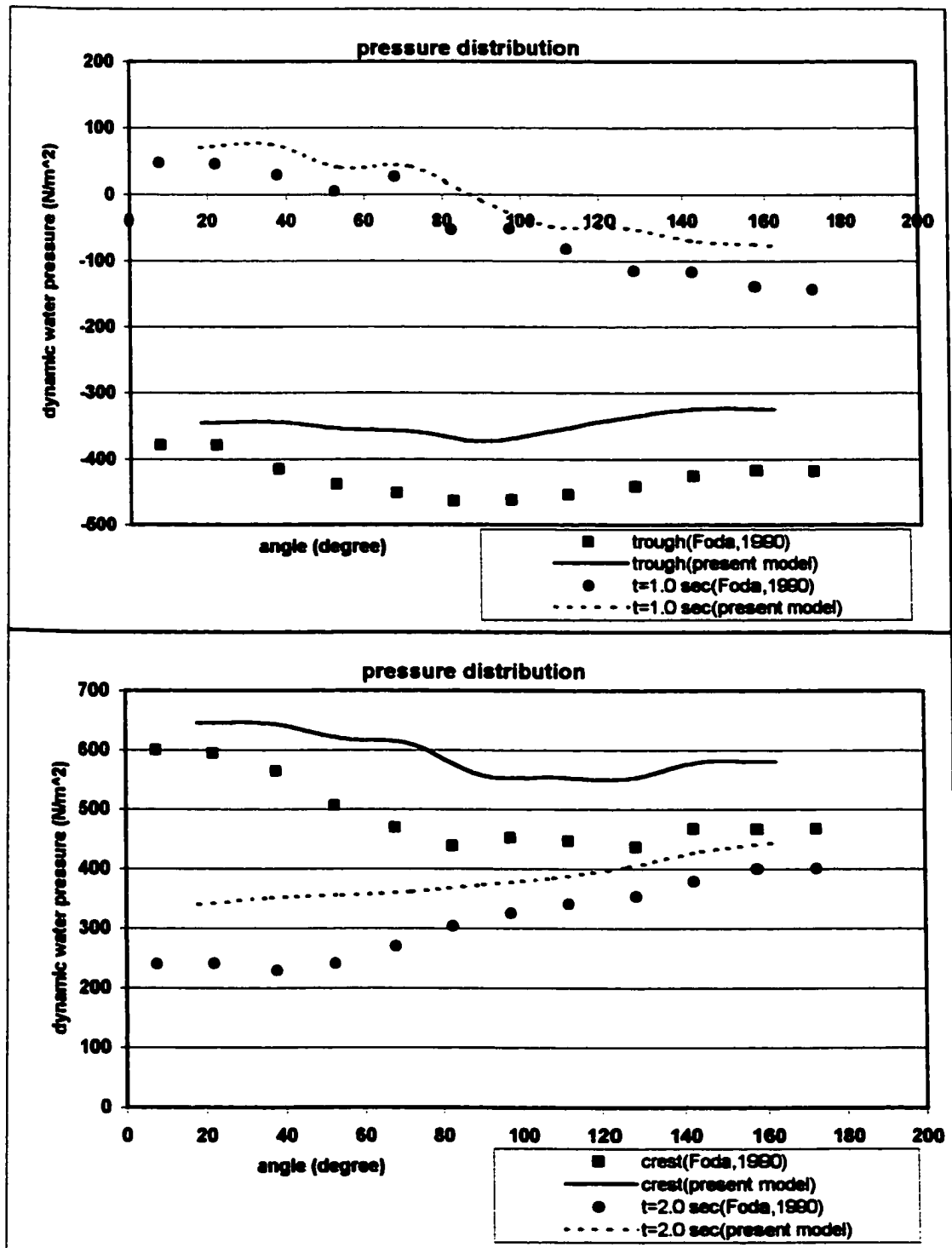


**Fig. 4-45 Comparison of water pressure of the present model and experiment (Foda, 1990) on exposed half-surface of pipe during one full wave cycle**

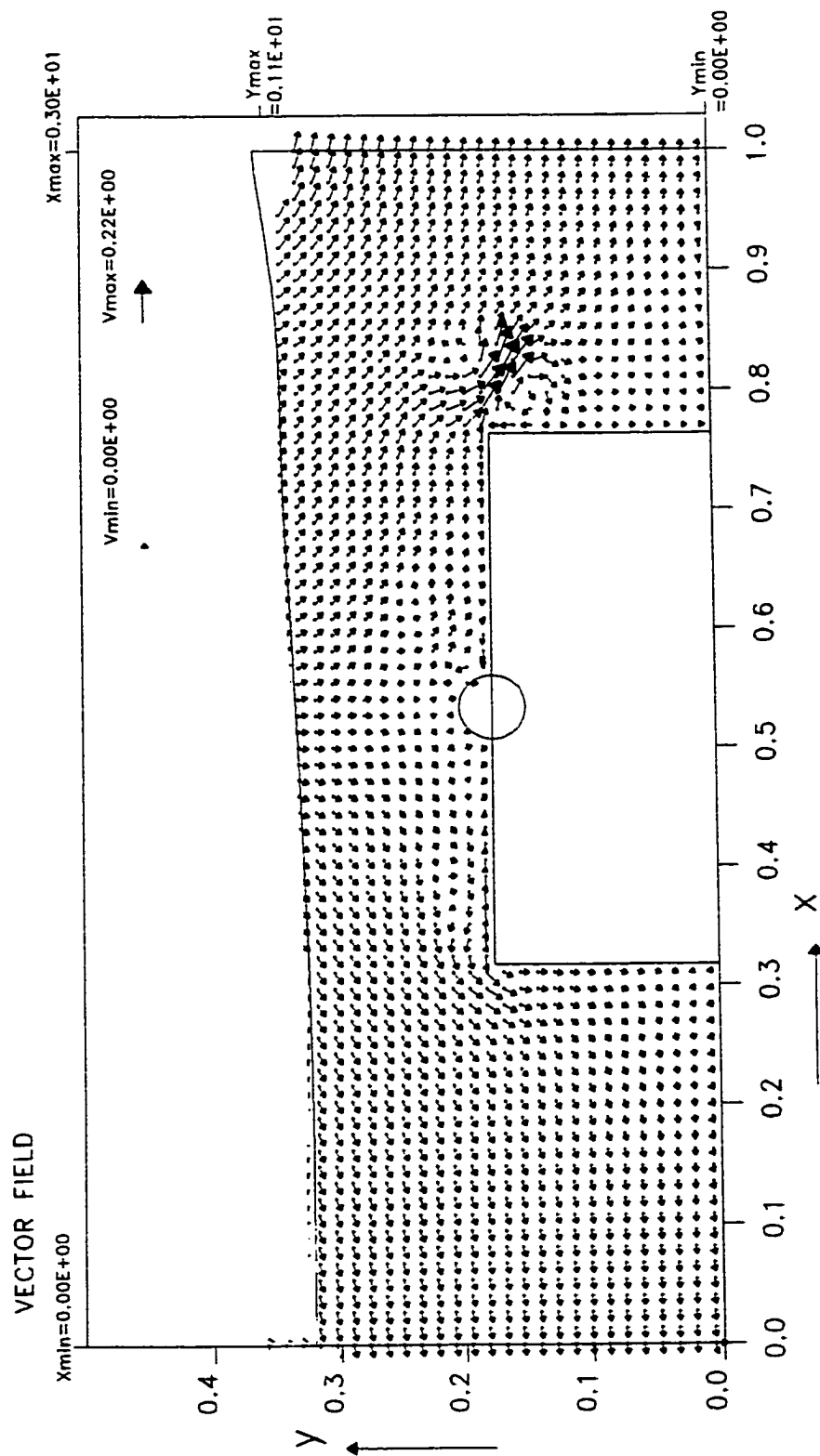
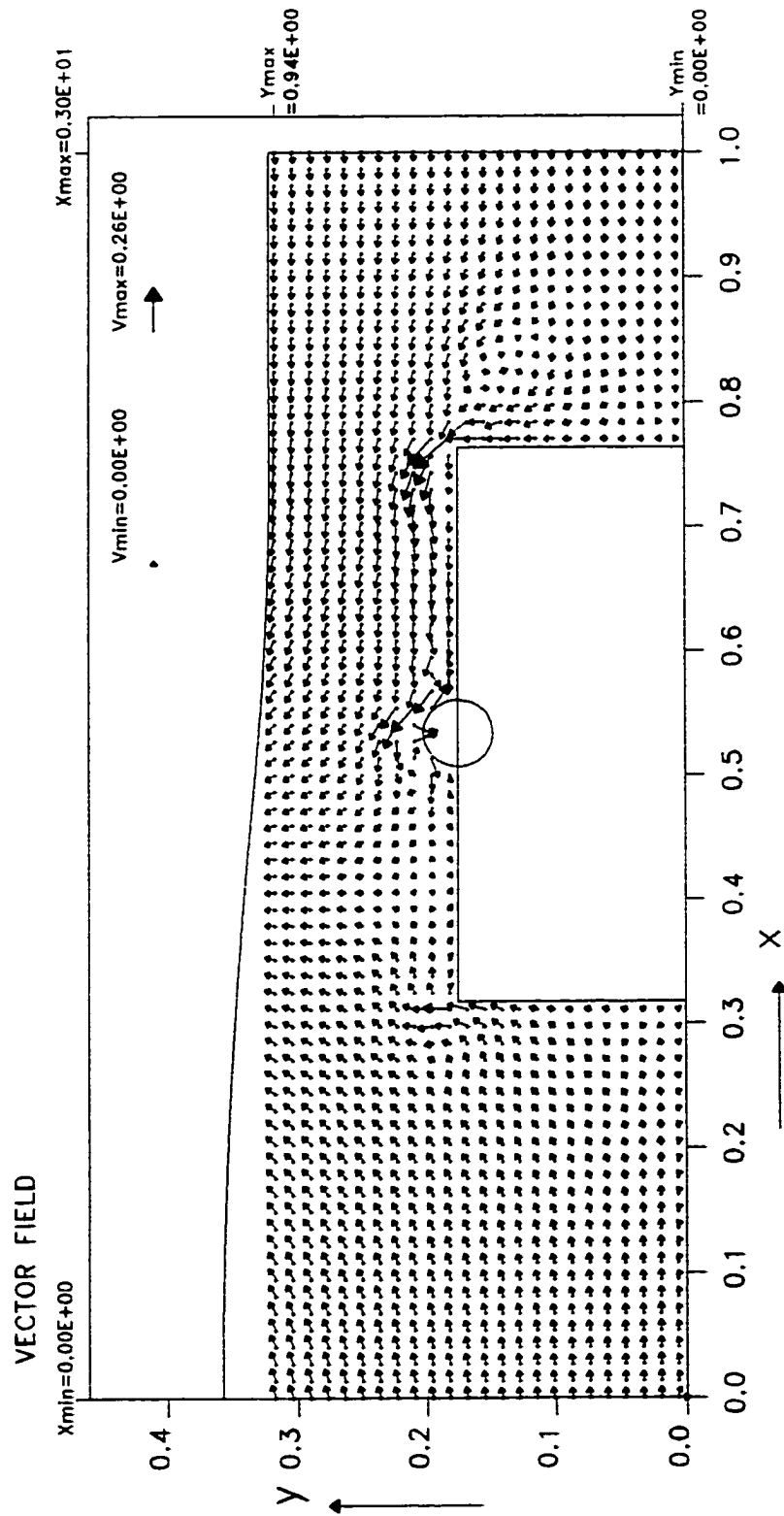


Fig. 4-46 Close-up of velocity field is around the sand basin and pipe by present model, while the wave crest just passes over the pipe.



**Fig. 4-47 Close-up of velocity field is around the sand basin and pipe by present model, while the wave trough just passes over the pipe.**

equation shown in Fig.4-48 for a half-buried pipe of diameter  $D$  are calculated by the Morison equation,

$$F_D = \frac{1}{2} C_D \rho \left( \frac{D}{2} \right) u |u| + C_M \rho \left( \frac{\pi D^2}{2} \right) \frac{du}{dt}$$

where  $u(t)$  = the unsteady ambient water velocity near the pipe;  $D$  = the pipe diameter;  $\rho$  = the water density;  $C_D$  = the drag coefficient; and  $C_M$  = the added-mass coefficient. The ambient water velocity was estimated using Dean's stream-function calculation. Over many selected wave cycles, the best-fit values for the drag coefficient ranged between  $-0.188$  and  $0.861$ , while the added-mass coefficient ranged from  $1.51$  to  $2.08$  (Foda, 1990). It can be seen that the negative maximum net drag force acts on the half-buried pipe in the seaward direction while the wave trough passes over the pipe. And the positive maximum net drag force acts on the half-buried pipe in shoreward direction while the wave crest passes over the pipe. Based on the results in Fig.4-48, the drag force acts on the half-buried pipe backward and forward during a wave period. With combination of the lift force and drag force acting on the pipe, Foda's experiment showed that the half-buried pipe would break away from the sand bed.

In the present numerical model, by necessity, the arc of pipe is replaced a series of the straight line. Thus pressure distribution on exposed pipe has some difference between the numerical and experimental results, especially when wave crest and



wave trough pass over the pipe. But the numerical results appear to be reasonable in explaining the physical phenomena around the pipe. And the maximum net pressure (drag force) acting on the pipe compares well with the experimental data, with some time delay.

#### **4.4.2 Hydrodynamic Forces on a Half-buried Pipe Studied by the Sanitation District of Orange County, CA.**

In July 1997, The Sanitation District of Orange County contracted Carollo engineers to investigate the rock sizes needed to protect the 120-inch outfall that was designed and constructed in the late 1960s and early 1970s. In addition, the forces to which the outfall is exposed are studied and computed. The 120-inch diameter outfall pipeline located at Newport Bay, Orange County is shown in Fig.4-49. The location 1 and location 2 of the pipeline are chosen for the studies of the hydrodynamic forces acting on the pipeline. The water depth  $h$  is 40.65 ft and 32.65 ft corresponding to high tide and low tide conditions, respectively, at location1, and depth  $h$  is 47.75 ft corresponding to low tide condition at location 2.

The design waves to be used in the evaluation of the rock protection were obtained in part from an exhaustive study of extreme waves conducted by the U.S. Army Corps of Engineers as part of the Coast of California Storm and Tidal Wave Study. Additional data were obtained from Seymour (1996). These data were supplemented by storm waves obtained by wave hindcasting procedures conducted by Pacific Weather Analysis. The waves produced by an offshore storm event

consist of waves that vary in both height and period. The wave height is defined as the distance between a wave crest and wave trough. The wave period is defined as the time interval from one wave crest to the next wave crest.

The significant wave height  $H_{1/3}$  is used to represent the incident wave in this study. At location 1 and location 2, the variation of the probable maximum wave height with recurrence interval is presented in Fig.4-50 and Fig.4-51, respectively. The significant wave height equals to the probable maximum wave height divided by 2.57 (Sanitation District of Orange County, 1997). The following table shows the relation between the wave variables and recurrence interval.

Recurrence Interval(year)	Depth $d_o$ (ft)	$H_{1/3}$ (ft)	$H_{1/3}/d_o$ (ft/ft)	Diameter of pipe $D$ (ft)/ $d_o$ (ft)	Height of basin $B$ (ft)/ $d_o$ (ft)
10	40.65	6.23	0.15	0.24	0.12
	47.75	4.28	0.09	0.20	0.10
20	40.65	7.39	0.18	0.24	0.12
	47.75	5.84	0.12	0.20	0.10
30	40.65	9.73	0.24	0.24	0.12
	47.75	7.78	0.16	0.20	0.10
50	40.65	10.12	0.25	0.24	0.12
	47.75	8.56	0.18	0.20	0.10
90	40.65	10.50	0.26	0.24	0.12
	47.75	12.45	0.26	0.20	0.10

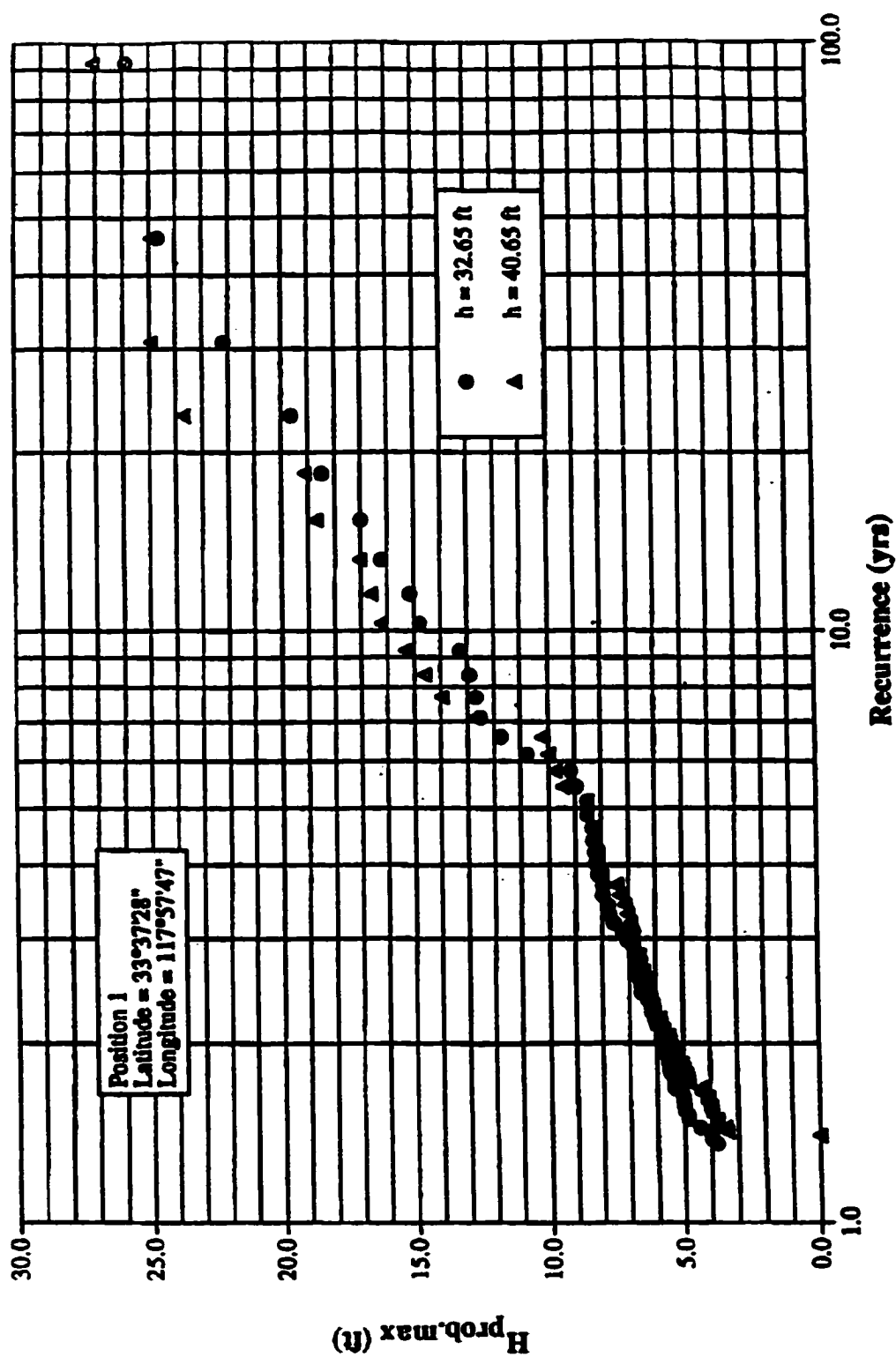


Fig. 4-50 Variation of probable maximum wave height with recurrence interval at location 1 in Orange County, California, July 1997.

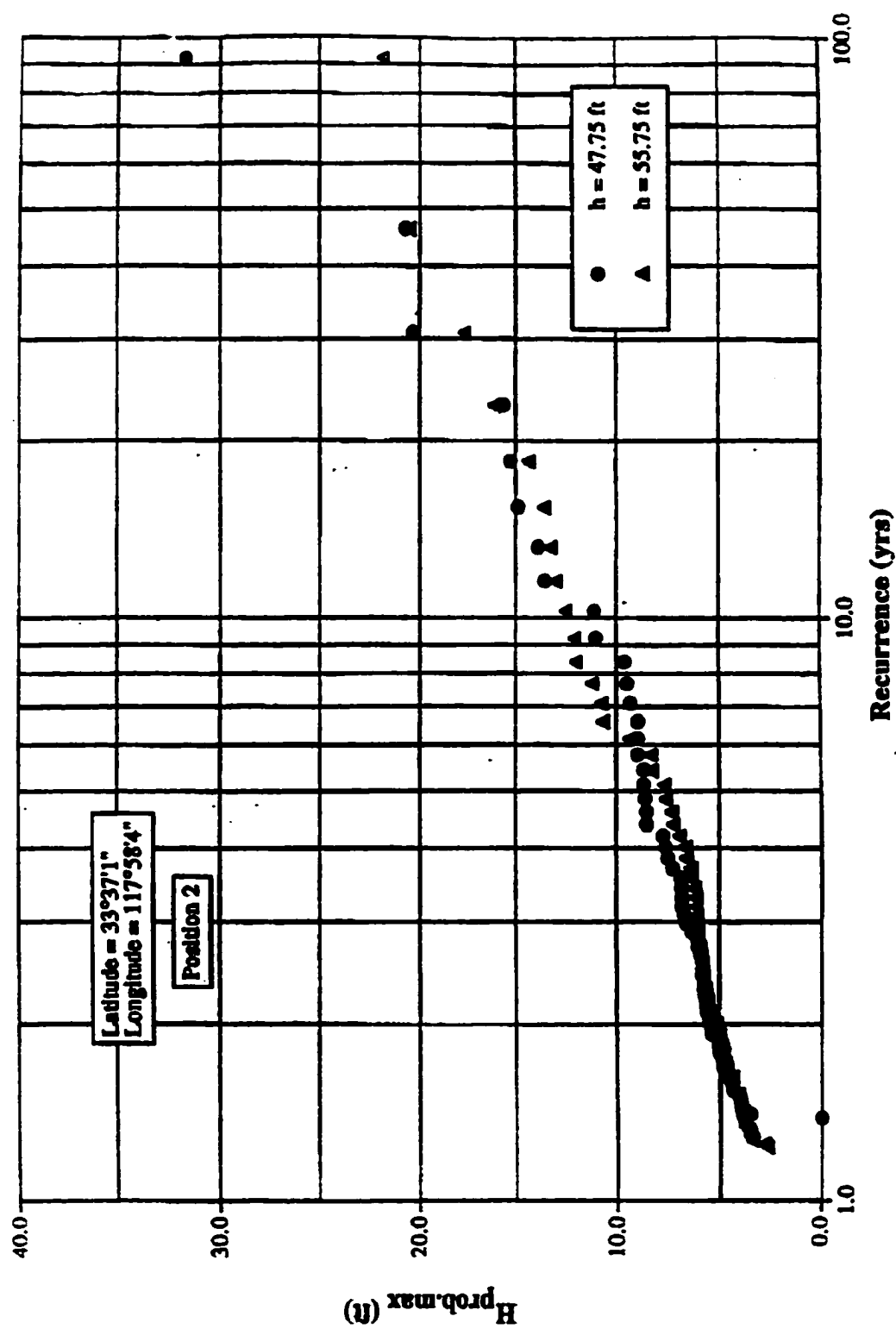


Fig. 4-51 Variation of probable maximum wave height with recurrence interval at location 2 in Orange County, California, July 1997.

To study the wave hydrodynamic force acting on the 120-inch diameter of the outfall pipeline, the present study uses two different numerical models to simulate the case. (1) First model is oscillatory wave passing over the outfall pipeline. The wave period  $T = 20$  sec. and the wavelength  $L = 723.57$  ft are for the water depth at 40.65 ft. For water depth = 47.75 ft, the wavelength  $L = 784.23$  ft with wave period  $T = 20$  sec.. In the report of Sanitation District of Orange County, there is no data of wavelength for the oscillatory wave. So the wavelength is computed by  $L = T\sqrt{gd_o}$  and is used in the oscillatory wave used in the present model. (2) Second model is solitary wave passing over the outfall pipeline. As a train of waves approaches the shallow water, it is observed that the crests become higher and the troughs become flattened. This kind of wave is approaching those represented by the solitary wave. The solitary wave height is assumed to be the half of the oscillatory wave height in this model. The variables used in the case of the depth 40.65 ft are  $dx/d_o = dy/d_o = 0.04$ ,  $dt/(d_o/g)^{0.5} = 0.04$ , Reynold's number  $R = 80,000$ . The variables used in the case of the depth 47.75 ft are  $dx = dy = 0.02$ ,  $dt/(d_o/g)^{0.5} = 0.02$ , Reynold's number  $R = 80,000$ .

The data are presented in Fig.4-52 where the horizontal, vertical, and resultant force are presented at the two different depths, 40.65 ft and 47.75 ft, as a function of the recurrence interval. The forces based on the analytical method were determined

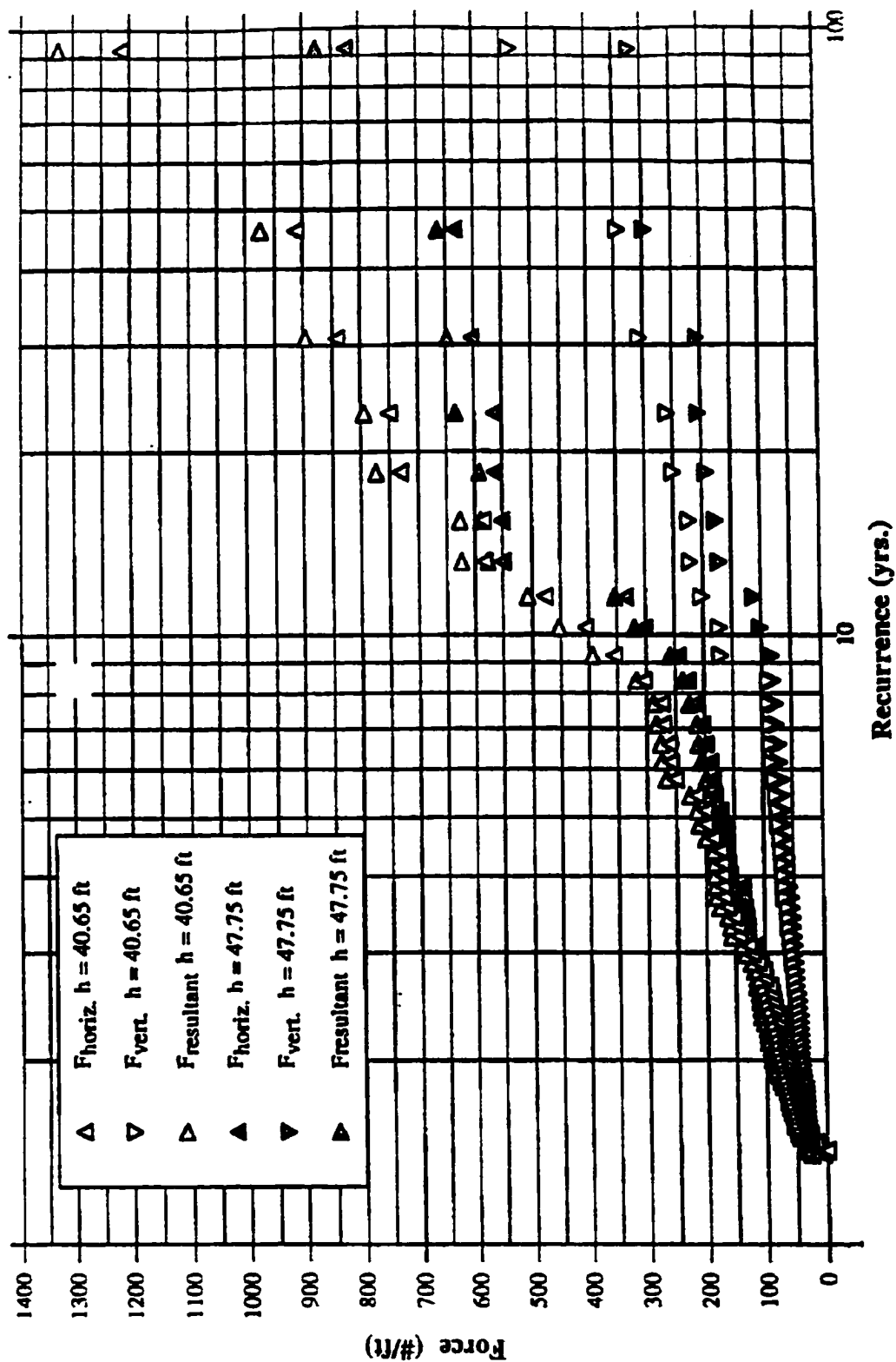


Fig. 4-52 The vertical, horizontal, and resultant forces acting on a circular pipe at the depths of 40.65 ft and 47.75 ft in Orange County, California, July 1997.

based on the velocity and acceleration in a direction perpendicular to the longitudinal axis of the pipe. Based on the report's data, there is angle  $\theta$  between the incoming wave propagation direction and the outfall pipeline. This is needed to determine the velocities and accelerations acting in a direction perpendicular to the pipe.

The data are presented in Fig.4-53 to Fig.4-55 where the drag, lift and resultant forces are presented for the depth = 40.65ft, and the forces presented in Fig.4-56 to Fig.4-58 are for the depth = 47.75ft. At location 1 the water depth is 40.65ft, the angle  $\theta$  ranges from  $20^\circ$  to  $50^\circ$  for recurrence interval 10-years to 30-years and the angle  $\theta$  ranges from  $20^\circ$  to  $30^\circ$  for recurrence interval 50-years to 100-years. So the wave forces acting in a direction perpendicular to longitudinal axis of the pipe are lesser for recurrence interval 10-years to 30-years and are larger for recurrence interval 50-years to 100-years. But in the present models, the wave is perpendicular to the pipe. So the forces, recurrence interval from 10-years to 30-years, have large difference between numerical results of oscillatory, solitary wave models and report's data in Fig.4-53 to Fig.4-55. But recurrence interval from 50-years to 100-years, the numerical results of the solitary wave model compare well with report's data than oscillatory wave model does.

At location 2 the water depth is 47.75 ft, the angle  $\theta$  is around  $0^\circ$  for recurrence interval 10-years to 30-years and the angle  $\theta$  ranges from  $0^\circ$  to  $20^\circ$  for recurrence

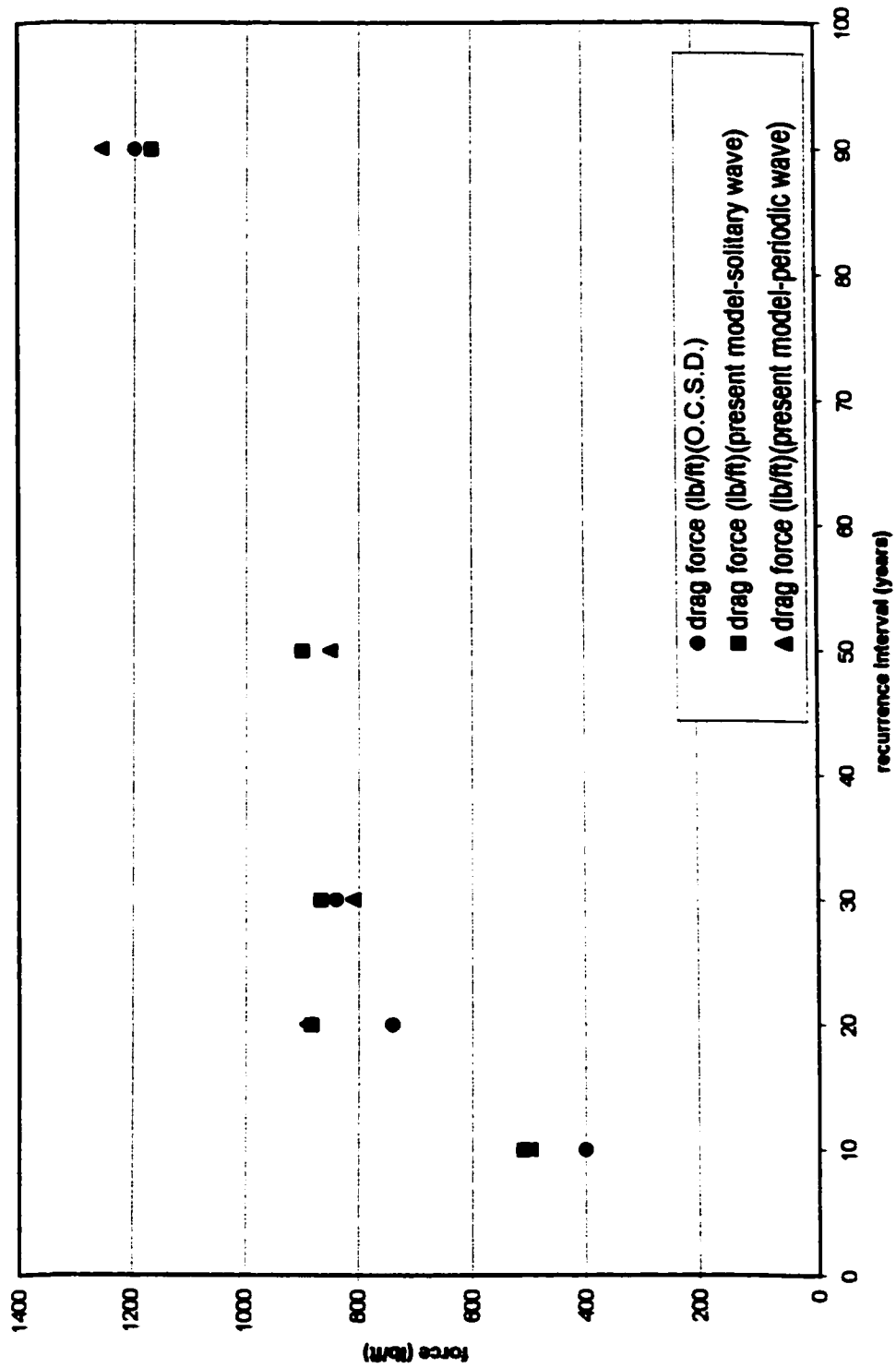


Fig. 4-53 Comparison of drag forces of the present model with solitary and periodic waves and the report of Orange County Sanitation District at the depth of 40.65 ft



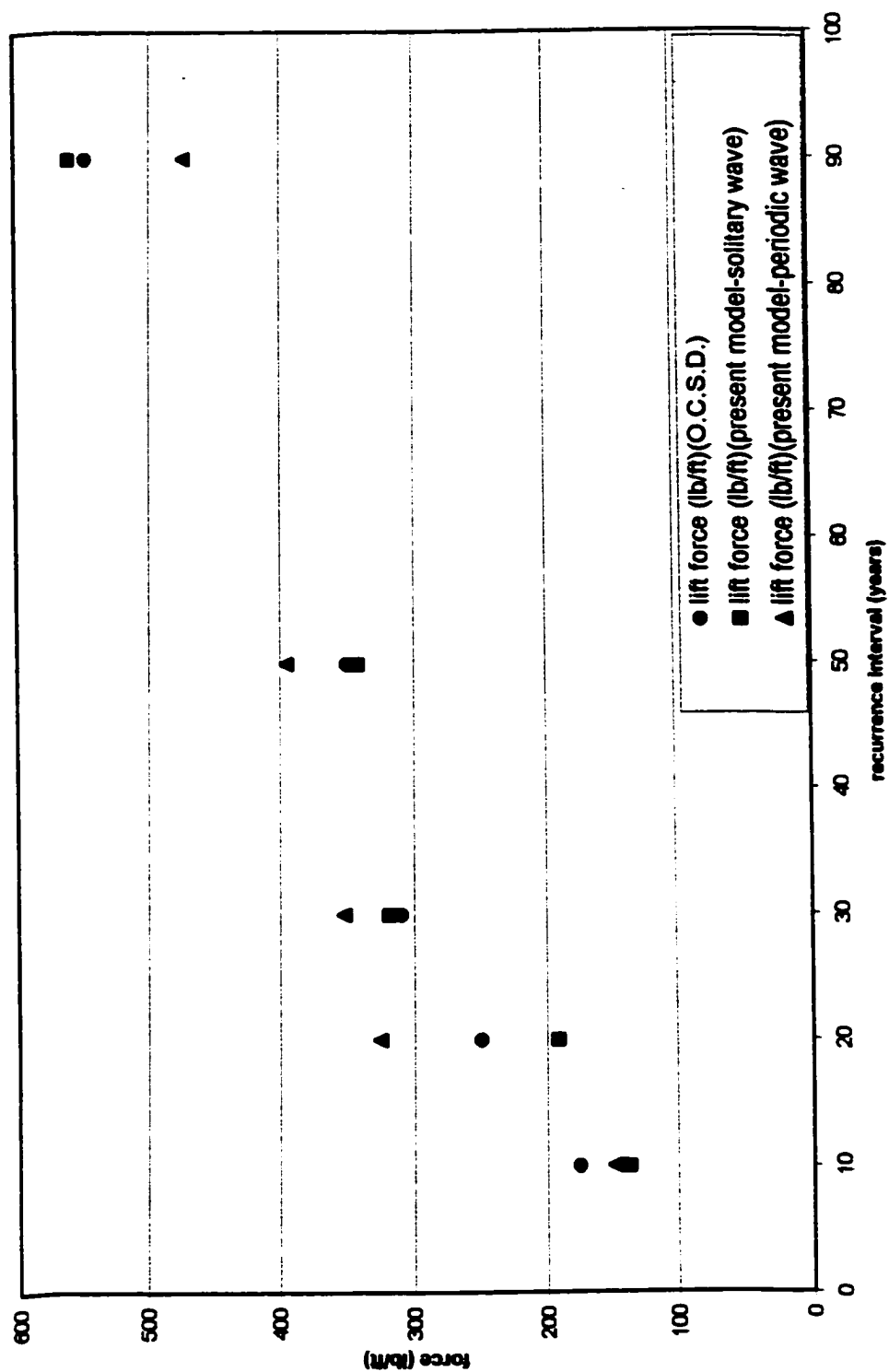


Fig. 4-54 Comparison of lift forces of the present model with solitary and periodic waves and the report of Orange County Sanitation District at the depth of 40.65 ft

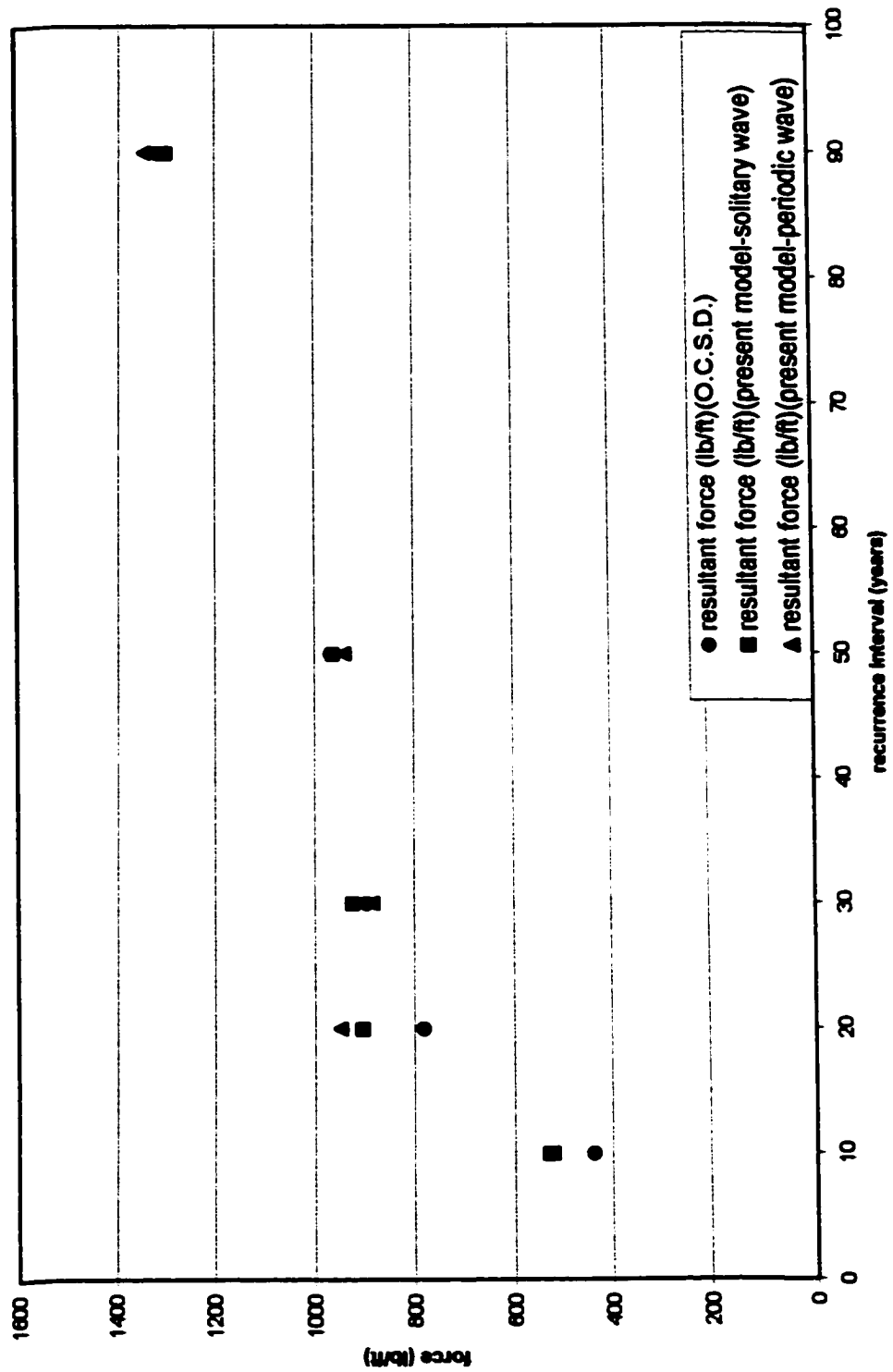


Fig. 4-55 Comparison of resultant forces of the present model with solitary and periodic waves and the report of Orange County Sanitation District at the depth of 40.65 ft

interval 50-years to 100-years. The wave forces acting in a direction perpendicular to the pipe are larger for recurrence interval 10-years to 30-years and are lesser for recurrence interval 50-years to 100-years. So the forces, recurrence interval from 50-years to 100-years, have large difference between numerical results of oscillatory, solitary wave models and report's data in Fig.4-56 to Fig.4-58.

As a train of waves approaches the shallow water, it is observed that the crests become higher and the troughs become flattened. This kind of wave is approaching those represented by the solitary wave. In Fig.4-55, the shallow water depth is 40.65ft, the resultant forces by the solitary wave model are closer to the report's data than the ones by oscillatory wave model. But in Fig.4-58, the location 2 is far away from the shoreline and the water depth is 47.75ft, the resultant forces by the oscillatory wave model compare well with report's data than the ones by solitary wave model. The comparisons show that the solitary wave model is preferred in shallow water, and the oscillatory wave model would work better in deep water.

In Fig.4-54 and Fig.4-57 the present model and the report of Orange County Sanitation District show that the maximum vertical force upward at depth 40.65ft and 47.75ft are about the same and at worst is of the order of 500 lbs on recurrence interval 90-years. The weight of the pipe per foot filled with fresh water is approximately 3331.0 lbs in the downward direction. Therefore, there is a factor of safety of almost six times in the vertical force. The drag force at worst is of the

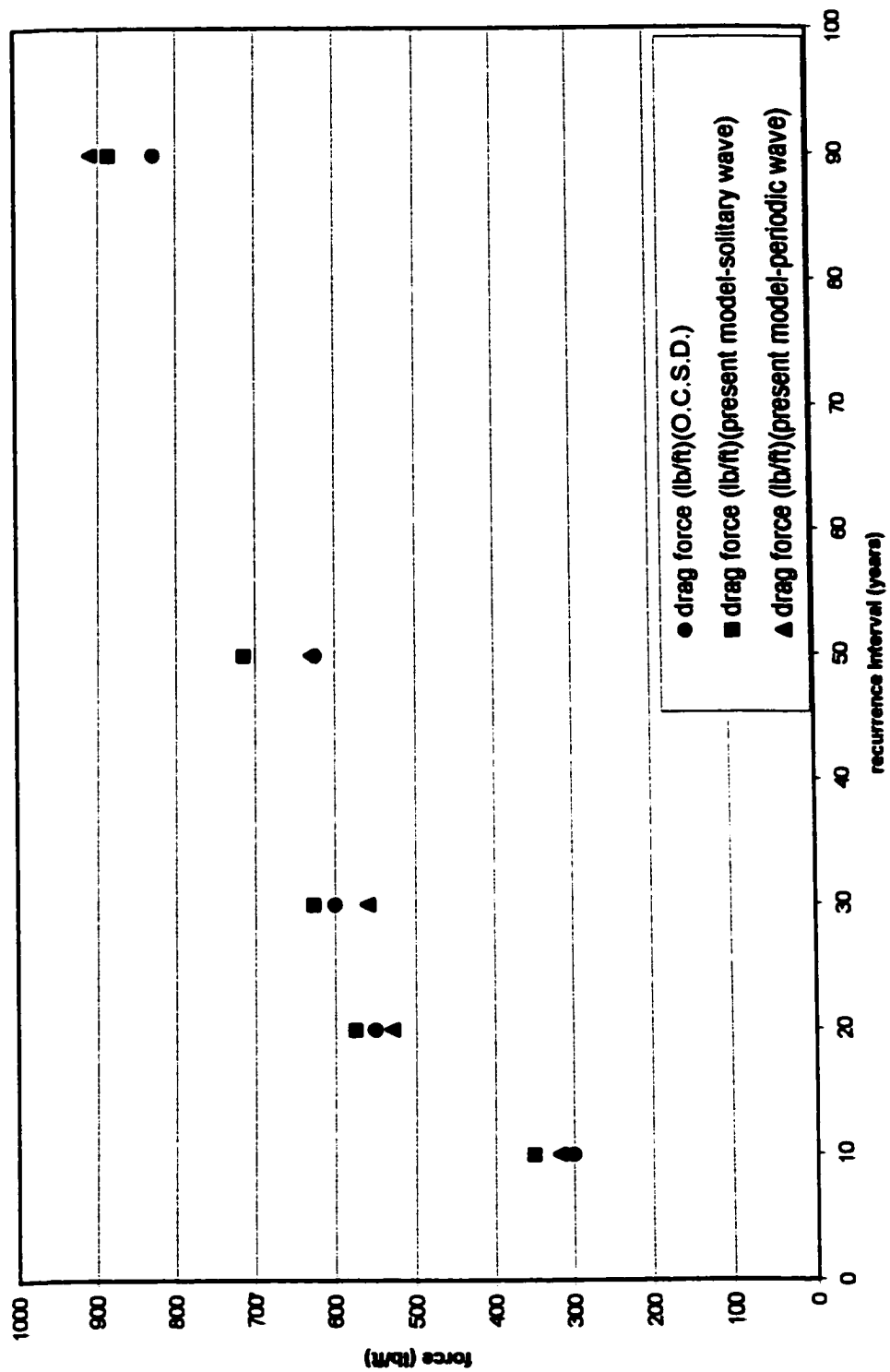


Fig. 4-56 Comparison of drag forces of the present model with solitary and periodic waves and the report of Orange County Sanitation District at the depth of 47.75 ft

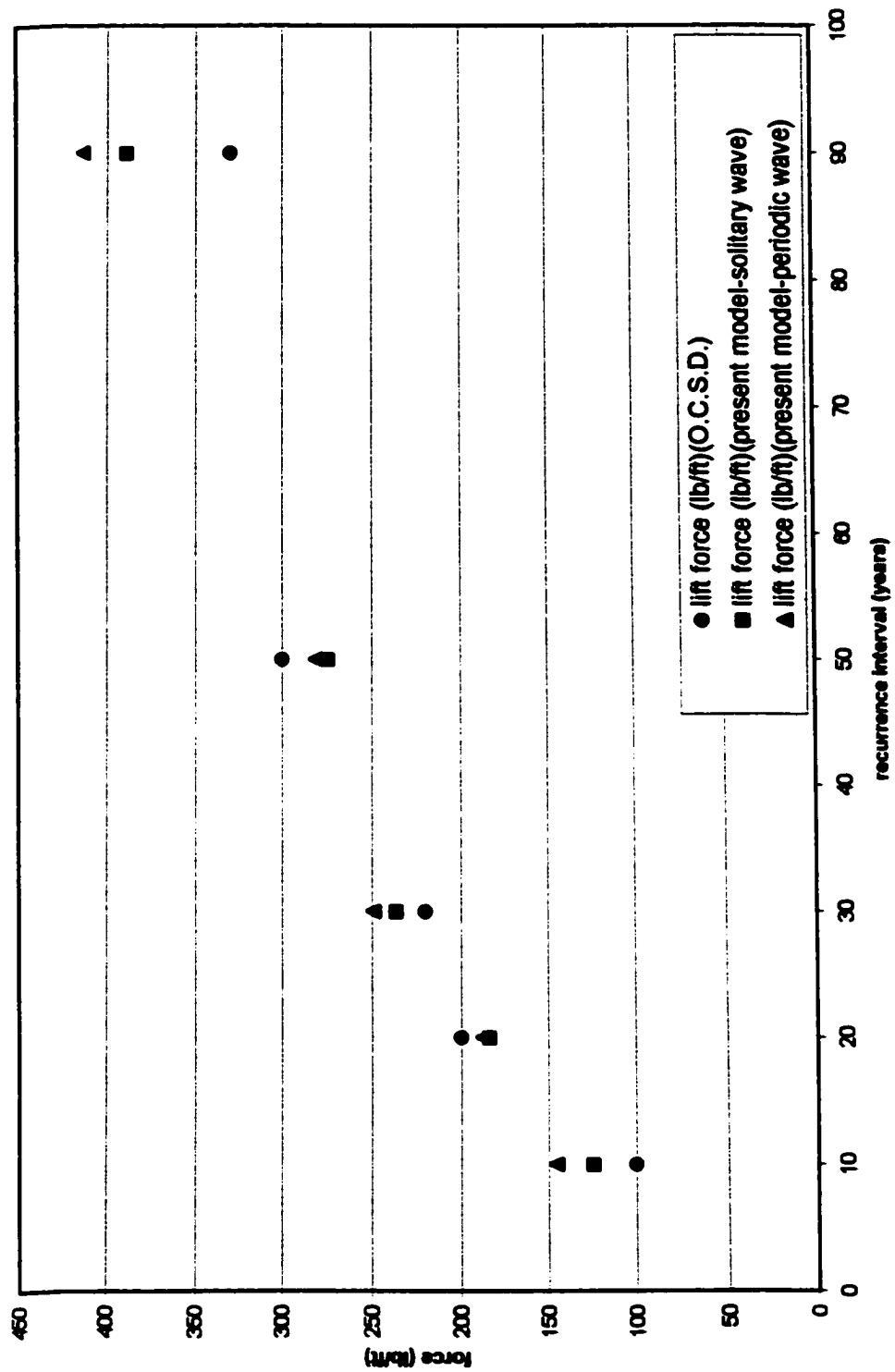


Fig. 4-57 Comparison of lift forces of the present model with solitary and periodic waves and the report of Orange County Sanitation District at the depth of 47.75 ft

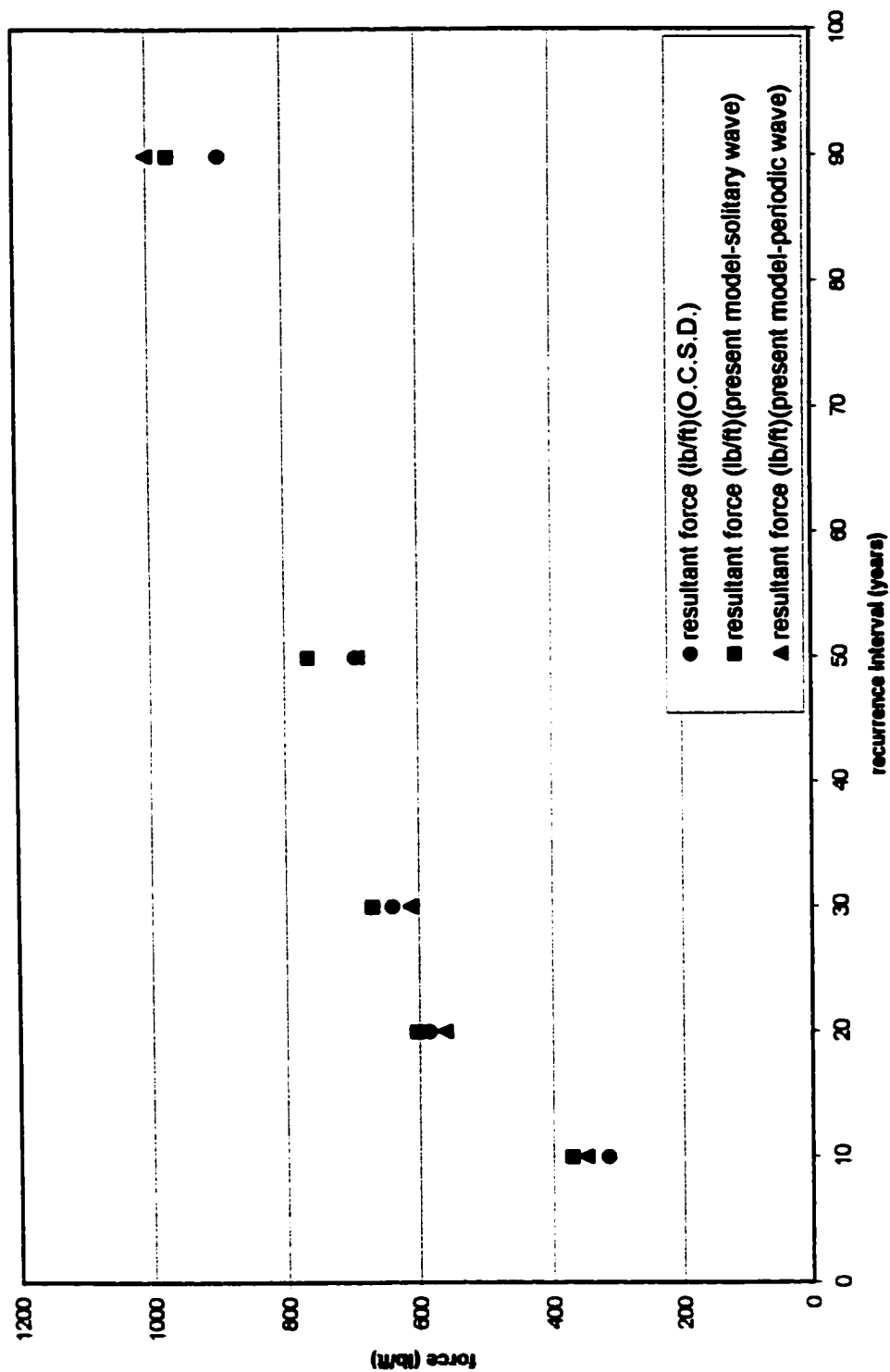


Fig. 4-58 Comparison of resultant forces of the present model with solitary and periodic waves and the report of Orange County Sanitation District at the depth of 47.75 ft

order of 1200 lbs on recurrence interval 90-years and if it acts on the midway up from the half-buried pipe. It can be shown that there is a significant resisting moment to prevent the pipe from rolling out of the matrix. Therefore, for the wave conditions investigated, the pipe is considered safe under the actions of the design waves.

## **Chapter 5**

### **Conclusion and Recommendation**

#### **5.1 Conclusions**

The present numerical model, which is based on the Navier-Stokes equation, is a powerful tool for the investigation of propagation large amplitude wave into the coastal zone as well as its interaction with marine structures. In the present study, three sets of comparisons are presented among numerical computations and experiments for (1) solitary wave overtopping submerged obstacle, (2) solitary wave shoaling on the slopping and vertical structures, and (3) periodic wave and solitary wave overtopping the submarine half-buried pipeline. The agreement of the free surface elevation and velocity distribution is found to be good.

The following major conclusions can be drawn and they are divided into the categories corresponding to the main areas of this investigation:

##### **5.1.1 Overtopping the Submerged Rectangular Structure**

The critical failure areas in structures of caisson are the toe and underlying foundation due to the wave-induced scouring, liquefaction and large stresses in the foundation soil. (Tsai, et al. 1986) The present modeling work shows that there are



rotational flows occurring around the submerged obstacle when the solitary wave propagates over it. These vortices are found in the vicinities of the submerged obstacle, the strongest one always occurs in the lee side of the submerged obstacle. Based on the results obtained, the submerged obstacle is found to be impacted severely by these vortices. These phenomena tend to scour and damage the foundation. To reduce the damage to keep these obstacles from damage, Liu, et al. (1999) shows that the porous armor layer is effective in reducing the overtopping rate as well as in preventing the caisson breakwater from bottom scouring.

The computed rotational flow field and the water surface profile using the present model compared well with the experimental data. The agreement between the present model and prior experiments is good for the water particle velocities obtained for several locations in the vicinities of the submerged obstacle. The comparison of the numerical results with the Ting and Kim's (1994) experiment shows that their inviscid theory (potential theory) would not accurately reproduce the experimental results at the shoreward region of submerged breakwater.

### **5.1.2 Run-up of Non-breaking Solitary Wave on Vertical Wall**

The present model can simulate the non-breaking wave climbing up the vertical structure. The maximum run-up height compares well with the analytical solution and other numerical results by prior investigators. It is seen that the present model results agree well with the analytical results of Laitone (1960). The agreement is

much better than any other numerical models. Thus, it is concluded that the analytical approximation by Laitone (1960)

$$R/d_o = 2H' + \frac{H'^2}{2} \quad H' : \text{normalized wave height} = H/d_o$$

can be used to predict the preliminary result of solitary wave run-up on the vertical wall.

### **5.1.3 Run-up of Non-breaking Solitary Wave on Steep Sloping Beaches**

The present model simulated the non-breaking solitary wave shoaling on steep slopes  $45^\circ$  and  $30^\circ$ . The agreement of the water surface profiles and spatial velocity distributions between the present model and Camfield and Street's (1968) experiment for slope  $45^\circ$  and Lin's (1999) experiment for slope  $30^\circ$  is very good during the wave run-up. The discrepancies of maximum run-up between the present model and experiments, with slopes  $S = 45^\circ, 30^\circ$  are only 0.9% and 5%, respectively.

The vertical variations of the horizontal velocity component on the steep slope can be very strong. These variations suggest that any shallow water wave approximation in the sloping beach region is incorrect.

### **5.1.4 Run-up of Breaking Solitary Wave on a Mild Sloping Beach**

The present model simulated the solitary wave shoaling on a mild slope ( $2.88^\circ$ ) reasonably well until the solitary wave overturning and breaking taking place. The free surface elevations and velocities agree well with experimental measurements before the profile of the wave crest becomes steep. The water surface profile predicted by the present model agrees better with the experiment than the one by the WENO numerical method used by Li (2000).

The results of the present model also show that the water surface elevations and the horizontal velocities are under-predicted slightly when compared with experiments but the comparisons with experiments are better than the WENO numerical method (Li, 2000). The present model and the experiment show that there are two major characteristics as the incident wave shoals in the mild sloping beach, (1) a narrow peak appears at the leading edge, and (2) an extended triangular wedge-shaped region forms behind the peak. This is because of the buildup of non-linear effect causing the wave crest to increase and the slope of the wave front to become steep. As wave shape is further steeper, the particle velocity near the crest become too big to be sustainable. Thus wave will break. But the present model will stop when the wave breaks.

### **5.1.5 Wave-induced Force on Half-buried Marine Pipeline**

One of the advantages of the present model is that it can be used to simulate the significant practical problem. The present model is used to simulate the periodic and

solitary wave overtopping the half-buried pipeline. In Fig.4-55 and Fig.4-58, the comparisons show that the solitary wave model is preferred for application in shallower water and the oscillatory wave model would work better in deep water region.

The present computer model when compared with the experimental study conducted for the Orange County Sanitation District show that the maximum vertical force upward at depth 40.65ft and 47.75ft are about the same and at worst is of the order of 500 lbs for wave height associated with recurrence interval 90 year. The weight of the pipe per foot filled with fresh water is approximately 3331.0 lbs downward. Therefore, there is a factor of safety of almost six times for the lift force computation. The drag force at worst is of the order of 1200 lbs for wave associated with recurrence interval 90 year and if it acts on the midway up from the half-buried pipe. It can be shown that there is a significant resisting moment to prevent the pipe rolling out of the matrix. Therefore, the pipe is considered safe from rolling.

## **5.2 Recommendation for Future Studies**

Based on the present investigation, three possible future research directions can be recommended here:

1. All optical sensing techniques, including laser doppler velocimetry (LDV) and particle image velocimetry (PIV), fail to measure velocity in the region where air bubble density becomes large. Therefore no velocity data in the

roller region of a breaking wave can be accurately measured using these methods. To obtain more information about the wave breaking and run-up process, more experimental measurements using digital particle imaging velocimetry (DPIV) have to be conducted.

2. The present numerical model fail to simulate the broken solitary wave propagating toward the shoreline. It appears that plunging jet is important to understand the wave breaking kinematics and the energy dissipation process. A numerical model, similar to that used by Lin, et al. (1999) solving the Averaged Navier-Stokes equation and improved  $k - \varepsilon$  equation, might lead to more accurate results of jet and the maximum run-up of solitary waves.
3. The present model has the potential to be extended to study three-dimensional problems about the diffractions around the submerged breakwater, breaking wave run-up on the slopping beach, and the wave acting on the half-buried pipeline with arbitrary incident angle.

## **Reference List**

- [1] Beji, s. and Battjes, J.A., ‘Numerical simulation of nonlinear wave propagation over a bar’, Coastal Engineering 23, pp.1-16, 1994**
- [2] Bryndum, M. B., Jacobsen, V., and Brand, L. P. (1983). ‘ Hydrodynamic forces from wave and currents loads on marine pipelines.’ Proc. 15<sup>th</sup> Offshore Tech. Conf., 1, 95-102.**
- [3] Camfield, F. E. and R. L. Street, J. Waterways and Harbors Division, ASCE 95, WW1, paper 6380, 1 (1968), 1.**
- [4] Carrier, G. F. and Greenspan, H. P. (1958). ‘Water waves of finite amplitude on a sloping beach.’ J. of Fluid Mechanics, Vol. 16, 447-459.**
- [5] Cevik, Esin and Yalcin Yuksel (1999). ‘Scour under submarine pipelines in waves in shoaling conditions.’ Journal of Waterway, Port, Coastal, and Ocean Engineering, ASCE, 125(1), 9-19**
- [6] Chan, Robert K.-C. and Street, Robert L., ‘A computer study of finite-amplitude water waves’, Journal of Computational Physics 6, pp.68-94, 1970**
- [7] Chan, Robert K.-C. and Street, Robert L., ‘ Shoaling of finite amplitude waves on plane beaches.’ 12<sup>th</sup> International Conference on Coastal Engineering, 1970**

- [8] Chubarov, L. B. and Shokin, Yu I. (1987). 'The numerical modeling of long wave propagation on the framework of non-linear dispersive models.' *Computers and Fluids*, Vol. 15, No. 3, pp. 229-249
- [9] Fletcher, C.A.J., 'Computational techniques for fluid dynamics', Second Edition, Springer-Verlag, 1991
- [10] Foda, M. A. (1985). 'Pipeline breakout from seafloor under wave action.' *Appl. Oc. Res.*, 7(2), 79-84
- [11] Frederiksen, C. S. and Watts, A. M. (1981). 'Finite element method for time dependent incompressible free surface flow.' *Journal of Computational Physics*, 39, 282-304.
- [12] Grace, R. A., and Zee, G. T. Y. (1981) 'Wave force on rigid pipes using ocean test data.' *Journal of Waterway, Port, Coastal, and Ocean Engineering*, ASCE, 107(2), 71-92.
- [13] Grilli, Stephen T.; Losada, Miguel A. and Martin, Francisco (1994). 'Characteristics of solitary wave breaking induced by breakwaters.' *J. Waterway, Port, Coastal and Ocean Engineering*, Vol. 120, No. 1.
- [14] Grilli, S. T., I. A. Svendsen, and R. Subramanya (1997). 'Breaking criterion and characteristics for solitary waves on slopes.' *Journal of Waterway, Port, Coastal, and Ocean Engineering*, ASCE, 123(3), 102-112

- [15] Herbich, John B. 1999. ‘ Handbook of Coastal Engineering’ pp.3.1-3.101
- [16] Hayashi, Masahiro; Hatanaka, Hatsumori and Kawahara, Mutsuto (1991). ‘ Lagrangian finite element method for free surface Navier-Stokes flow using fractional step methods.’ International Journal of Numerical Method in Fluids, Vol. 13, 805-840
- [18] Hibbrd, S. and Peregrine, D. H. (1979). ‘Surf and Run-up on a beach: a uniform bore.’ J. Fluid Mechanics, Vol. 95, part 2, pp. 323-345
- [19] Hughes, Thomas J. R.; Liu, Wing Kam and Brooks, Alec (1979). ‘Finite element analysis of incompressible viscous flows by the penalty function formulation.’ Journal of Computational Physics.
- [20] Ippen, Arthur T. and Kulin, Gershon (1954). ‘The shoaling and breaking of the solitary wave.’ Proc. 5<sup>th</sup> Int. Conf. Coast. Eng., Grenoble.
- [21] Jordaan, J. M., JR., U.S. Naval Civil Engineering Laboratory, Technical Note N-691, 1965.
- [22] Kirby, J.T. and Dalrymple, R.A., 1983. ‘ Propagation of obliquely incident water waves over a trench.’ Journal of Fluid Mechanic, 133 : 47-63.
- [23] Kobayashi, Nobushisa and Wurjanto, Andoyo, ‘Wave overtopping on coastal structure’, Journal of Waterway, Port, Coastal, and Ocean Engineering, Vol. 115, No.2, March, 1989



- [24] Kobayashi, Nobuhisa and Karjadi, Entin A. (1994). 'Surf-similarity parameter for breaking solitary wave run-up.' *Journal of Waterway, Port, Coastal, and Ocean Engineering*, Vol. 120, No. 6.
- [25] Latione, E. V., ' The second approximation to cnoidal and solitary waves.' *Journal of Fluid Mechanics*, Vol. 9, part 3, pp 430-444, 1960
- [26] Lee, J.J, Zhuang, F., and Chang, C., 'Kinematic measurements of wave overtopping on marine structure', *Proceeding of the Second International Symposium on Ocean Wave Measurement and Analysis (Wave 93)*, July 25-28 1993, New Orleans, Louisiana, pp.821-834
- [27] Lemos, C.M. (1992). 'Wave breaking'. Springer, Berlin.
- [28] Li, Ying (2000). ' Tsunamis: Non-breaking and breaking solitary wave run-up' Ph.d. dissertation in California Institute of Technology.
- [29] Lin, P., and Liu, P. L.-F (1998). 'Turbulence transport, vorticity dynamics and solute mixing under plunging breaking waves in surf zones.' *J. Geophys. Res.*, 103(c8), 15, 677-15,694.
- [30] Lin, Pengzhi, Kuang-An Chang, and Philip L.F. Liu (1999). 'Runup and Rundown of Solitary wave on Sloping Beaches.' *Journal of Waterway, Port, Coastal, and Ocean Engineering*, ASCE, 125(5), 247-255

- [31] Liu, Philip L. F., Pengzhi Lin, Kuang-An Chang, and Tsutomu Sakakiyama (1999). 'Numerical model of wave interaction with porous structures.' *Journal of Waterway, Port, Coastal, and Ocean Engineering*, ASCE, 125(6), 322-330
- [32] Lording, P.T., and Scott, J.R., 1971. 'Armor stability of overtopped breakwater.' *J. Waterw. , Harbors and Coast. Engr. Div.*, ASCE. 97 (2): 341-354.
- [33] Mostafa A. Foda, Jo Y. H. Chang, and Adrian W. K. Law, (1990) 'Wave-induced breakout of half-buried marine pipes.' *Journal of Waterway, Port, Coastal, and Ocean Engineering*, ASCE, 116(2), 267-286
- [34] Nishimura, H., and Takewaka, S. (1990). 'Experimental and numerical study on solitary wave breaking.' *Proc. 22<sup>nd</sup> Int. Conf. Coast Engrg.*, ASCE, New York, 1033-1045.
- [35] Pirooz, Moharram Dolatshahi (1996). 'Finite element methods for viscous free surface fluids including breaking and non-breaking waves.' Ph.D. Thesis, University of Southern California, Los Angeles, CA
- [36] Ramaswamy, Balasubramaniam and Kawahara, Mutsuto (1987). 'Arbitrary Lagrangian-Eulerian finite element method for unsteady, convective, incompressible viscous free surface fluid flow.' *International Journal for Numerical Methods in Fluids*, Vol. 7, 1053-1075

- [37] Sanitation District of Orange County (1997). 'The structural condition of the 120 inch outfall and general repair of the 78 inch outfall.'
- [38] Stoker, D. E., "water wave", Interscience Publishers, Inc., New York, 1957.
- [39] Summer, B. Mutlu and Jorgen Fredsoe (1990), 'Scour below pipelines in waves.' Journal of Waterway, Port, Coastal, and Ocean Engineering, ASCE, 116(3), 307-323
- [40] Synolakis, C.E.(1987). 'The runup of solitary waves.' J. Fluid Mech., Cambridge, U.K., 185, 523-545.
- [41] Ting, Francis C.K. and Kim, Young-Ki, 'Vortex generation in water waves propagating over a submerged obstacle', Coastal Engineering 24, pp.23-49, 1994
- [42] Tsai, Y. T., McDougal, W. G., and Sollitt, C. K. (1986). 'An analytical model for ocean wave-soil-caisson interaction.' Proc., 20<sup>th</sup> Int. Conf. On Coastal Engrg., ASCE, Taipei, Taiwan, 2314-2328
- [43] Tuck, E.O. and Hwang, L. (1972). 'Long wave generation on a sloping beach.' J. of Fluid Mechanics, 51, 449-461
- [44] Verley, Richard L. P., Kostas F. Lambrakos, and Knut Reed (1989) 'Hydrodynamic forces on seabed pipelines.' Journal of Waterway, Port, Coastal, and Ocean Engineering, ASCE, 115(2), 190-204

- [45] Welch, J.E., Harlow, F.H., Shannon, J.P. and Daly, B.J., Los Alamos Scientific Laboratory Report LA-3425 1966. [See also Phys. Fluids 8 (1965), 2182 and 9 (1965), 842]
- [46] Wiegel, R. L. (1964), 'Oceanographical engineering.' Prentice Hall, Englewood Cliffs, New Jersey.
- [47] Zelt, J. A. (1991). 'The run-up of non-breaking and breaking solitary waves.' Coastal Engineering, 15, 205-246
- [48] Zhuang, F., Chang, C., and Lee, J.J., 'Modeling of wave overtopping over breakwater', Proceedings of The Twenty-Fourth International Conference on Coastal Engineering, pp.1700-1712, ASCE, Kobe, Japan, Oct. 23-28, 1994